NASA Contractor Report 172488

Evaluation of the Feasibility of Scale Modeling to Quantify Wind and Terrain Effects on Low-Angle Sound Propagation

G.S. Anderson, R.E. Hayden, A.R. Thompson, and R. Madden

Bolt Beranek and Newman Inc.
Cambridge, MA 02238

Contract NAS1-16521
January 1985

National Aeronautics and Space Administration
Langley Research Center
Hampton, Virginia 23665

Report No. 5516 NASA CR 172488

EVALUATION OF THE FEASIBILITY OF SCALE MODELING TO QUANTIFY WIND AND TERRAIN EFFECTS ON LOW-ANGLE SOUND PROPAGATION

G.S. Anderson
R.E. Hayden
A.R. Thompson
R. Madden

January 1985

Prepared by:

Bolt Beranek and Newman Inc.
10 Moulton Street
Cambridge, MA 02238

Prepared for:

National Aeronautics and Space Administration
Langley Research Center

TABLE OF CONTENTS

TABLE OF CONTENTS (cont'd)

LIST OF FIGURES

LIST OF FIGURES (cont'd)

LIST OF FIGURES (cont'd)

LIST OF FIGURES (cont'd)

LIST OF TABLES

ABSTRACT

The objective of this study was to evaluate the feasibility of acoustical scale modeling techniques for modeling wind effects on long-range, low-frequency outdoor sound propagation. Upwind and downwind propagation was studied in 1/100 scale for flat ground and simple hills with both rigid and finite ground impedance over a full scale frequency range from 20 to 500 Hz.

Results are presented as 1/3-octave frequency spectra of differences in propagation loss between the case studied and a free-field condition. Selected sets of these results were compared with validated analytical models for propagation loss, when such models were available. When they were not, results were compared with predictions from approximate models developed specifically for this study. Comparisons were encouraging in many cases considering the approximations involved in both the physical modeling and analysis methods. Of particular importance was the favorable comparison between theory and experiment for propagation over soft ground.

EVALUATION OF THE FEASIBILITY OF SCALE MODELING TO QUANTIFY WIND AND TERRAIN EFFECTS ON LOW-ANGLE SOUND PROPAGATION

1. INTRODUCTION

The prediction of sound propagation over long distances is of interest in a variety of situations in which the source and receiver are both on or near the ground. In such cases, a number of important physical effects influence the manner in which sound travels from the source to the receiver, thus influencing the net change in amplitude and phase of the sound observed at the receiver as compared with the source. Such effects include spreading loss and air absorption; ground and surface wave propagation; diffraction and scattering by terrain features and ground impedance changes; refraction by gradients in wind velocity and temperature; and scattering by turbulence. Mathematical models for propagation currently exist for simplified terrain geometries, temperature and wind velocity gradients, and ground impedance. Lacking, however, are validated mathematical models for the complicated terrain geometries actually encountered outdoors. In addition, even if appropriate models were to exist, local wind velocity profiles and turbulence characteristics around hills, valleys, etc. are difficult to characterize outdoors. Variations in each of these parameters combine to magnify the uncertainty in the prediction of sound propagation.

Clearly, we require a method to isolate individual factors affecting propagation and to assess the sensitivity to expected variations in each. Since analysis is not currently available for any but the simplest cases, separation of the individual contributions may be more readily accomplished through carefully controlled experiment rather than analysis. The understanding provided by these controlled experiments can assist in determining the limits of applicability of simplified mathematical

models and in validating more complicated models when they become available. The current approach focuses on the use of acoustical scale modeling to provide this controlled experiment.

Acoustical scale modeling has long been used in the design stage to study the characteristics of architectural spaces. In the last decade, the techniques have been applied to outdoor sound propagation over relatively short distances to investigate effectiveness of noise barriers around highways, sound propagation in urban and suburban spaces, and even air-to-water sound propagation. The technology for such acoustical scale modeling is quite well-developed [1].

As with all scale modeling techniques, the potential value lies in the ability to control and separate individual effects such as topographic scattering, ground impedance, wind, and temperature at the discretion of the researcher. This process is simply intractable when doing full scale studies outdoors. Indeed, one factor complicating outdoor sound propagation research is the difficulty in controlling meteorological conditions or fully characterizing enough parameters to properly interpret measurements. The only means for obtaining statistically significant full scale data on such phenomena as wind refraction, turbulence scattering, and ground waves is to conduct a large number of experiments over a long period of time during which a statistically significant number of similar conditions occur, a very expensive and time-consuming exercise at best. One recent study has provided a data base through which multiple regression analysis separates the effects of wind, temperature, and ground cover for flat terrain on a fixed range [2]. However, such a study required years of data acquisition and was limited to a particular site geometry, and of course could not independently control the meteorological variables.

To model the effects of sound propagation in the lower atmosphere, the atmospheric boundary layer must be properly characterized. This requires, at a minimum, the simulation of mean velocity profiles and the turbulence structure appropriate to a particular type of terrain. A boundary layer wind tunnel can be used for modeling the earth's atmospheric boundary layer in the lower 500 m or so. Such simulations replicate a so-called neutral stability condition which is common on most moderately windy days. However, to date, only one model study of the effects of flow on sound propagation has been reported [3]. In this study, the effects of wind on the performance of acoustical barriers was investigated, clearly showing decreased noise reduction over the barrier when wind was blowing in the same direction as the sound was propagating (6 to 10 dB increase for a 15 m/s wind), while the barrier's noise reduction was increased when the wind was blowing in the direction opposite to the direction of propagation. These results should be extended to study the effects of wind over complex terrain as well as studying the combined effects of wind and ground impedance variations.

2. WIND AND TERRAIN EFFECTS

The velocity gradient in the boundary layer, the direction of the wind, the topographical features of the terrain, and the local ground impedance are all expected to influence the long range propagation of sound. In particular, certain combinations may lead to either the creation or elimination of shadow zones. This program was designed to evaluate the feasibility of using scale models to evaluate the following effects.

1. Creation of refraction shadow upwind (Fig. 1, Effect 1). From a ray-acoustic point of view, the upward sound refraction creates a shadow zone into which no source rays penetrate.

2. Creation of soft-ground shadow upwind (Fig. 1, Effect 2). Where a soft-ground shadow did not exist because the ground was too remote, upward refraction can, in effect, bring the ground closer.

3. Elimination of diffraction shadow downwind (Fig. 1, Effect 3). A diffraction shadow behind intervening terrain is flanked by downward refraction.

4. Elimination of diffraction shadow upwind (Fig. 1, Effect 4). A diffraction shadow behind intervening terrain may be flanked upwind, because of the strong, anomalous wind gradients near the terrain peak. Such anomalous wind gradients can produce strong downward refraction, as shown. If this downward refraction is strong enough to overbalance the upward refraction along the rest of the sound path, then this flanking will exist.

Superimposed upon all of these are the effects of atmospheric turbulence. Turbulence can scatter sound energy into any of these shadows and partially compromise the level reduction within these shadows.

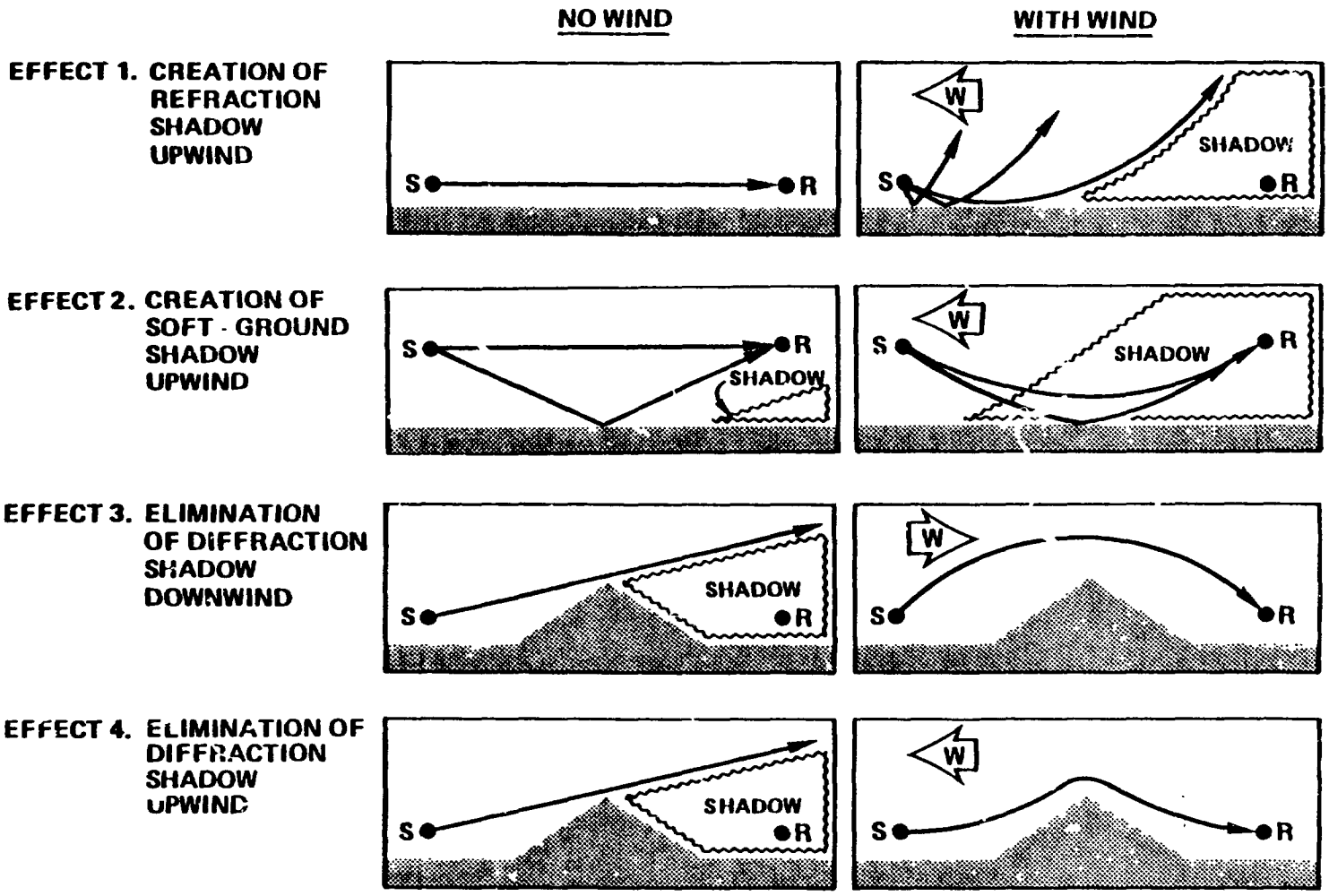

FIGURE 1. WIND AND TERRAIN EFFECTS.

3. SCALE MODELING

Conversion of propagation loss data obtained from a scale model with wind to full-scale conditions requires: (a) preservation of geometric and aerodynamic similarity, accounting for possible spatial variations in ground impedance that may exist in full scale but were not modeled in detail; and (b) removal of air-absorption effects from the model data prior to scaling to full scale.

3.1. Geometric similarity

The requirements for geometric similarity are met automatically by geometrically replicating the particular geometry or terrain feature of interest. The geometric scale factor (σ) sets the frequency scaling of the propagation data at $f \propto 1/\sigma$, since diffraction and scattering mechanisms are a function of the ratio of the acoustic wavelength to a typical dimension of the diffracting or scattering object. The geometric scale factor must also be preserved in developing the aerodynamic flow features relevant to the particular terrain of interest. These aerodynamic features include the shape of the mean velocity profiles (and shear stress profiles) in three dimensions, the gradient height (i.e., distance to the "top" of the boundary layer) and length scales of the turbulence. Such aerodynamic features may be expected to scale if Reynolds number effects are important.

3.2 Aerodynamic similarity

Physical or analytical modeling of propagation phenomena must replicate or account for all important physical phenomena. The primary justification for wind tunnel fluid modeling is that it provides the most effective means for replicating flow field phenomena associated with atmospheric boundary layer interaction with complex structures and topography. Furthermore, the wind tunnel allows one to control and vary parameters which are not

independently or conveniently controllable in full scale, providing a means for systematic sensitivity studies, which is indeed a logical extension of the present study.

However, as wind tunnels can only provide approximate and partial replication of full scale conditions, the most important physical similarity parameters must be preserved. For acoustic frequencies of interest in the present study, these are:

1. Reynolds number
2. Mach number.

More general studies of atmospheric modeling (including those involving very long wavelength sound waves whose properties depend on the large scale structure of the atmosphere) will require the consideration of further similarity parameters (c.f. the EPA Fluid Modeling Guidelines [4]).

Reynolds number

In the "Fluid Modeling Guidelines" [4] the EPA has established that, for sharp-edged geometries, the flow over significant elevated terrain and buildings near the source is Reynolds number independent if the Reynolds number, $Re_1 = U_H L/\nu$, is greater than 11,000, where U_H is the mean velocity upstream at the height of the obstacle H; L is the lesser dimension of the obstacle, and ν is the kinematic viscosity of air. Consequently, when working at small scale factors or with low velocities, local roughness upstream of the model may need to be exaggerated to preserve Reynolds number similarity.

Mach number

The Mach number of the atmospheric flow is of prime importance in that the rate and direction of refraction (ray bending) will be directly dependent on the local flow speed gradients. Also, the intensity (strength) of scattering and associated phase dispersion will depend on the local turbulence intensity along the propagation path.

In summary, for scale model sound propagation studies the following factors must be preserved:

- Geometric similarity
- Average surface roughness, length, and resultant distributions of mean velocity and turbulence
- Reynolds number
- Mach number.

The simulation methods used to achieve these are discussed further in Sec. 4 and also in detail in Ref. 4.

3.3 Air Absorption in Scale Model Testing

The model experiments will experience air absorption that is substantial over even short distances, due to the high frequencies involved in the modeling. This air absorption is "anomalous," in the sense that it does not exist in full scale, at the corresponding full-scale frequencies. The anomaly becomes greater than 10 dB in the range from 3-10 m at 50-100 kHz, depending upon the relative humidity in the laboratory.

Most of this air absorption is due to the so-called "classical" and "relaxation" phenomena [5]. These two phenomena, combined, result in the absorption shown in Fig. 2. There, sound level drop-off from a point source is plotted as a function of relative humidity, for the upper frequencies of interest in modeling. In this figure, the vertical scale is arbitrary. The various frequency-band data are separated vertically only to allow them to be more easily read from the graph.

At full-scale frequencies, the figure implies essentially no air absorption, as is expected. Therefore, all deviations from the -6 dB/dd (6 dB decrease per doubling of distance) baselines shown on the figure are "anomalous."

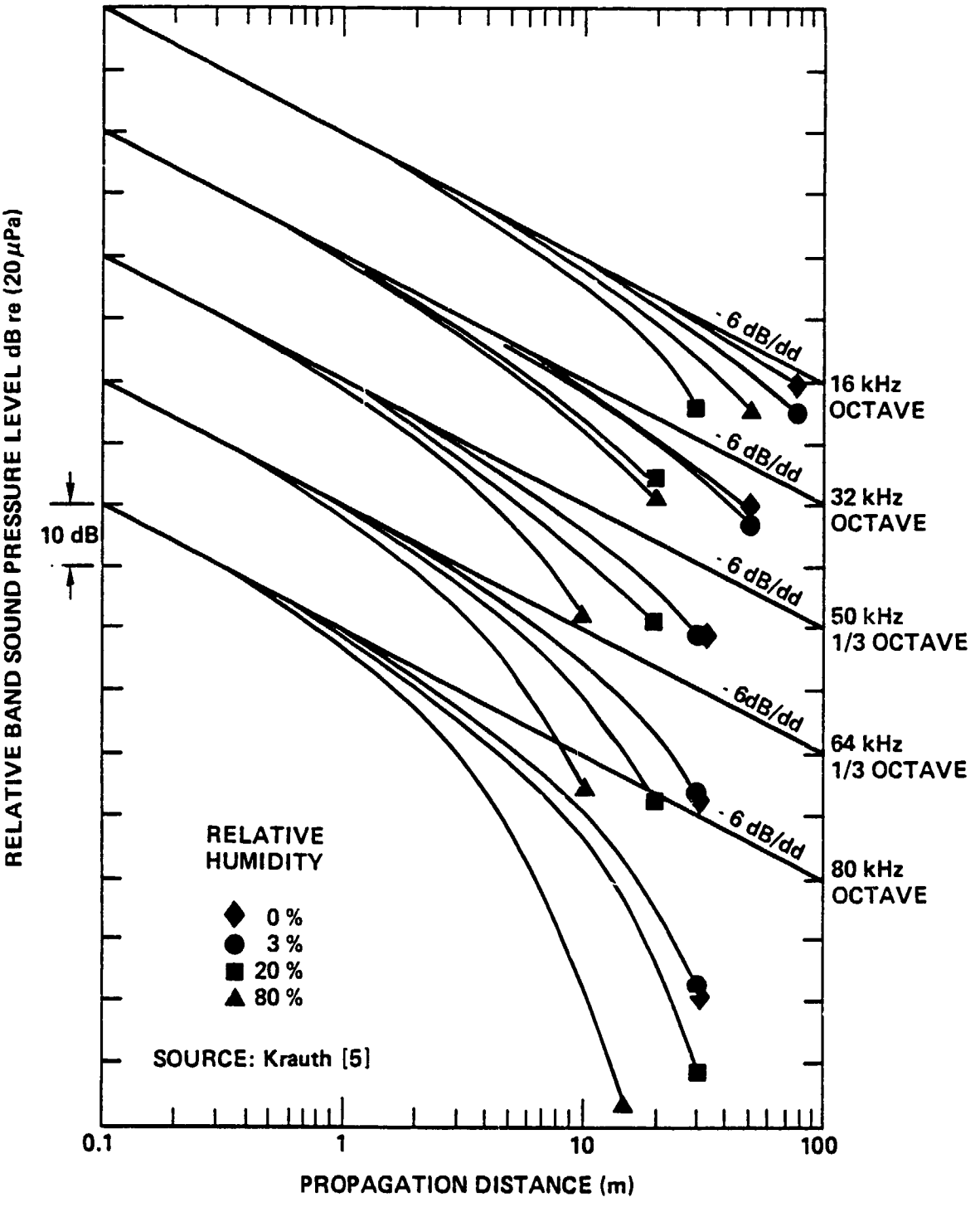

FIGURE 2. ANOMALOUS AIR ABSORPTION: COMBINATION OF "CLASSICAL" AND RELAXATION.

Figure 3 illustrates some direct measurements of this anomalous absorption, by scale model laboratory investigations. The bottom set of data (open symbols) are broadband measurements of the scaled A-level of roadway noise.

Although the relative humidities are generally not known for the data in Fig. 3, the data show generally less anomalous absorption than do the values in the preceding figure. This anomaly is associated with the use of a high intensity spark as the acoustic source. The high levels cause nonlinear regeneration of the high frequency energy, which replaces that lost by air absorption.

To evaluate the importance of nonlinear propagation in this study, the spectrum was measured at two distances from the spark source: the first quite close to the source (0.25 m) (approximately the same distance as the source microphone) and the second at a greater distance (2.0 m). After correction for normal divergence, the remaining level difference is a measure of the actual air absorption. For our particular source and laboratory condition (21° Celsius and 40% relative humidity), the match between this measured absorption and the theoretical absorption for linear propagation was sufficiently good to allow use of the standardized equation for air absorption and linear propagation theory (App. E) in the region between the source and receiver microphones.

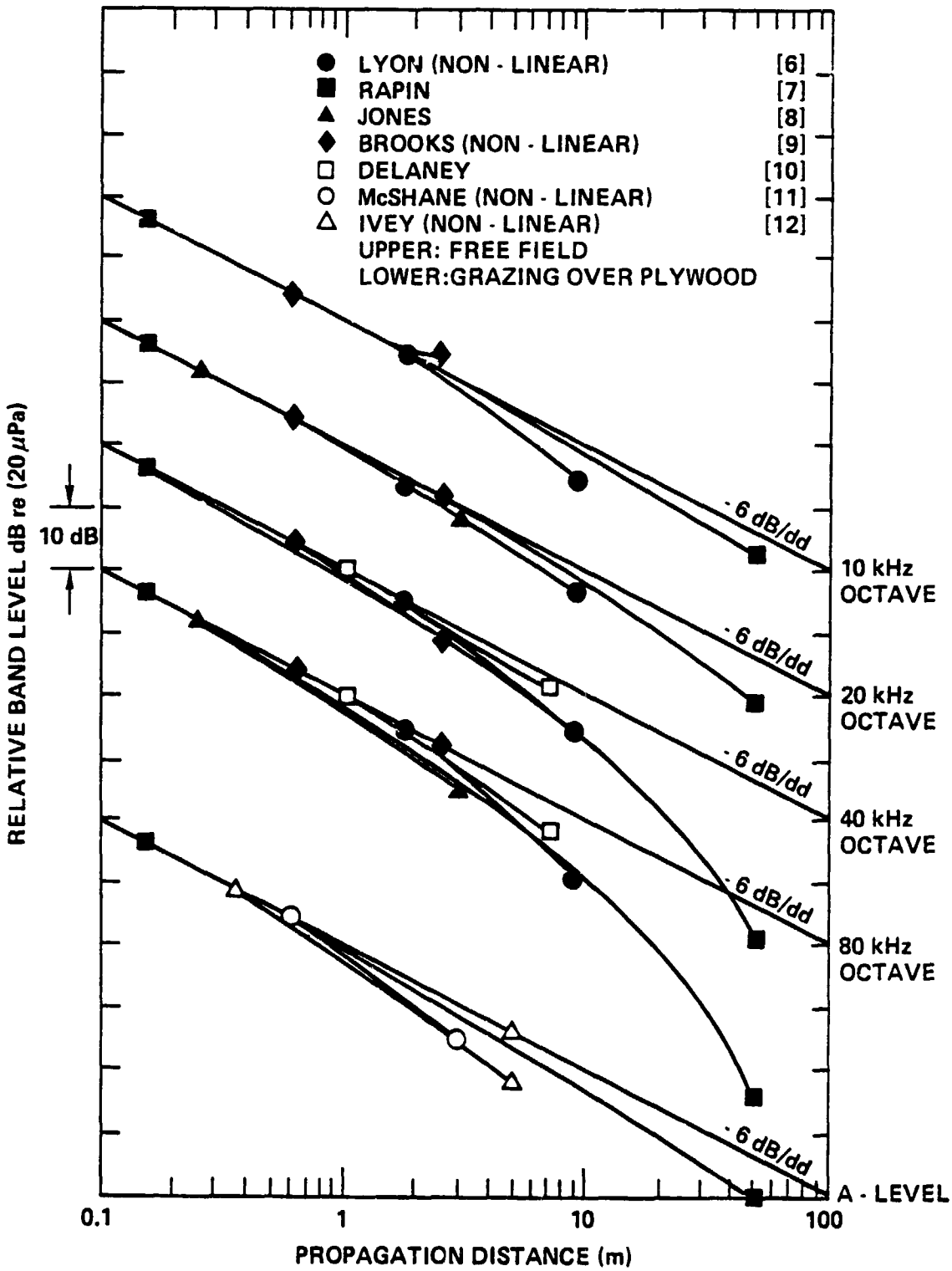

FIGURE 3. ANOMALOUS AIR ABSORPTION: SOME DIRECT MEASUREMENTS.

4. SCALE MODEL TESTING

This section provides background information on the 1/100 scale model sound propagation tests, including descriptions of the test facility, the impulsive sound source, the model ground impedance, and the methcd used to analyze the experimental data.

4.1. Flow Facility

The Atmospheric Boundary Layer Wind Tunnel, shown in Fig. 4, has a rectangular cross section of internal dimensions 2.4 m (wide) x 1.82 m (high) and an overall length of 18.2 m. The inlet section consists of a bellmouth contraction with turbulence damping screens at the face and at the front of the bellmouth. The atmospheric boundary layer profile is simulated by a series of spires at the entrance of the tunnel followed by roughness elements. At the throat, a 30-cm deep section of flow straighteners follows the screen and is in turn followed by two more screens downstream. Wind-direction changes are facilitated through use of a remotely controllable motorized turntable. Test-section air velocities in the range of 0.3 to 10.6 m/s can be achieved. The fan discharges into a large temperature-controlled working space surrounding the wind tunnel, leading to adequate mixing of room air for the type of measurements performed in this facility.

Rigorous procedures for establishing flow field similarity have been established by EPA [4]. The test facility used for this study complies with those requirements. Upstream flow field similarity is achieved by a long, slowly diverging duct that has roughness elements distributed along the floor of the tunnel. The roughness elements may be varied in size and spatial density in accordance with the scale of the model and the profile that one is attempting to replicate. In some cases, where a thick boundary layer is needed, spires are placed at the entrance of the tunnel to both provide an initial thickening of the boundary layer and to introduce large scale turbulence.

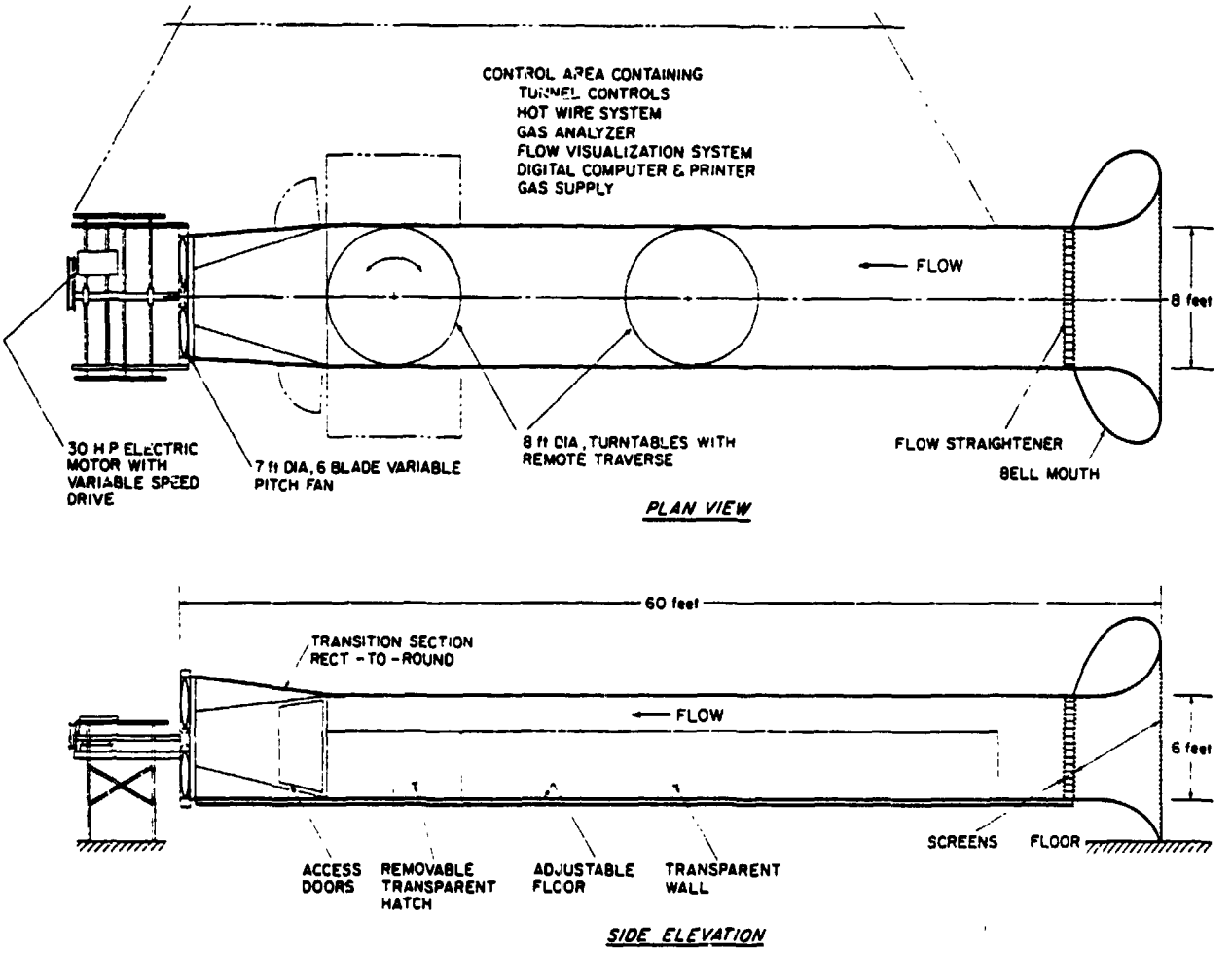

FIGURE 4. ATMOSPHERIC BOUNDARY LAYER WIND TUNNEL.

Figure 5 shows a photograph of one configuration modeled in the boundary layer wind tunnel during this study (looking upstream). The set-up shown is for an upstream-propagation case over a "hill." Roughness elements can be seen upstream of the test area; also, the spires are visible at the entrance to the flow-conditioning section. A reference microphone in the foreground and two receiver microphones are shown boom-mounted at the upstream edge of the test area.

4.2 Impulsive Sound Source

A sound source for use in the boundary-layer wind tunnel with reflective walls and ceiling must satisfy the following:

1. Impulsive rather than continuous-duration, so that acoustic paths can be easily identified and tunnel reflections removed
2. Sufficient acoustic energy to provide the required signal-to-noise ratio in the presence of electronic noise of the instrumentation system and flow-associated noise of the wind tunnel (both the mechanical noise of the fan and the wind noise of the moving air)
3. Excellent repeatability, so that differences at the receiver microphones are not caused by changes in the source output level
4. Uniform directivity in the vertical plane so that all ray paths will have the same source level.

4.2.1 Physical description

A high energy (50 J) electrical spark discharge was chosen to satisfy these requirements. This is essentially a point source that can be adjusted to various heights above the ground plane. The configuration of the spark source is shown in Fig. 6. A high voltage power supply, rated at 10 kV, was used to charge a 1 μF storage capacitor through a 100-kilohm resistor

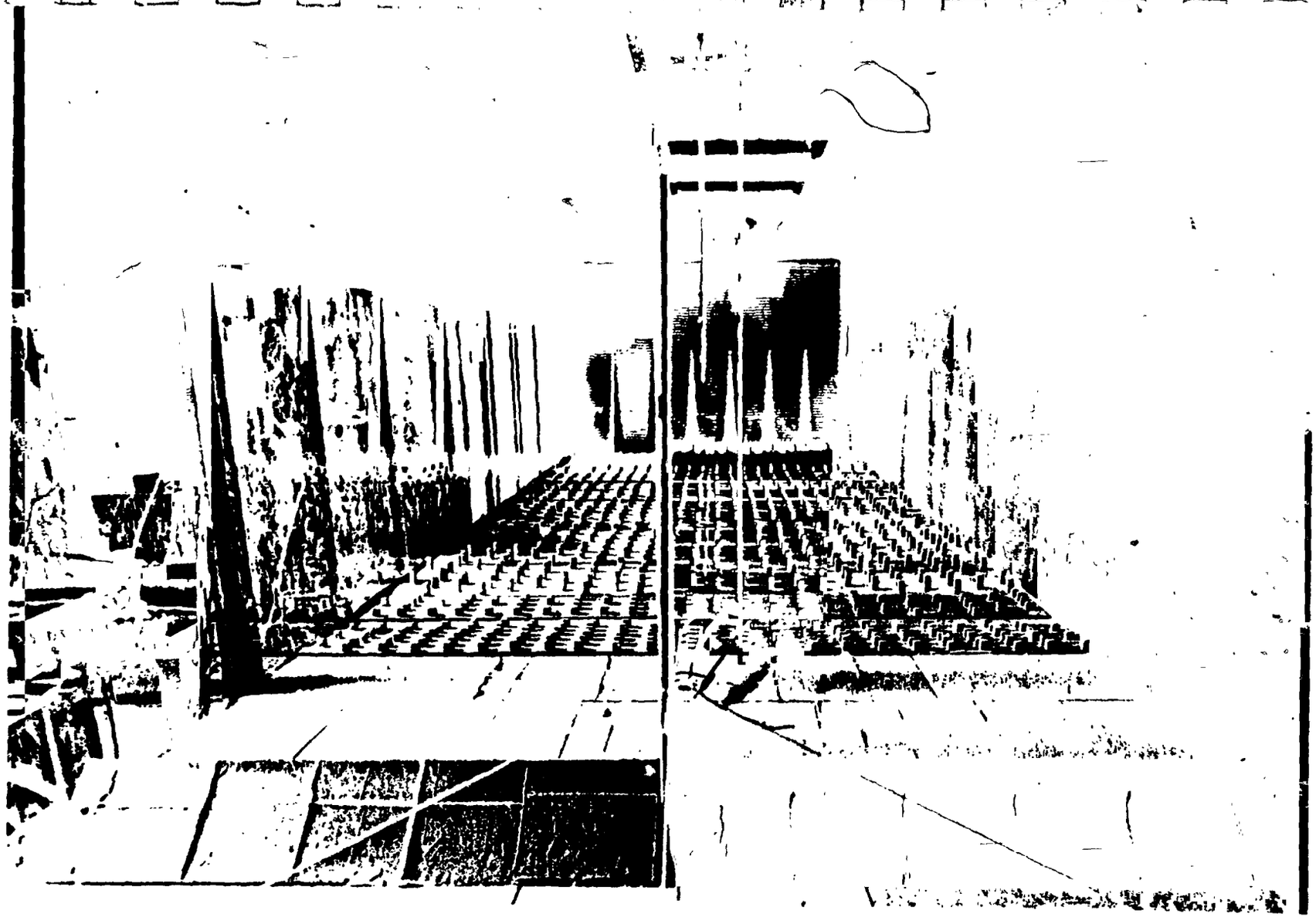

FIGURE 5. PHOTOGRAPH OF ATMOSPHERIC BOUNDARY LAYER WIND TUNNEL TEST SECTION (LOOKING UPSTREAM TOWARD SPIRES).

bank. The power supply was set at 8 kV to obtain longer spark-source-component life. The discharge circuit consists of the storage capacitor in series with the spark electrodes, a 1-ohm damping resistor, and a high-voltage trigger tube.

In operation, a separate clock circuit supplies a 300-V pulse to the trigger tube in the discharge circuit. This tube then "closes," electrically completing the discharge circuit. The stored energy then flows from the storage capacitor, through the damping resistor and the leads, to the spark gap.

As soon as the voltage across the storage capacitor drops significantly during discharge, the trigger tube "opens," interrupting the discharge circuit. This allows the power supply to recharge the storage capacitor.

The entire discharge process lasts approximately 100 μs. To allow such a fast rate of current change in the discharge circuit, the inductance of all elements has to be very low. Special low-inductance wire (108 nH/m) is used between the storage capacitor and the spark electrodes to minimize the largest source of inductance. Even then, the length of this wire has to be limited to approximately 3 m to minimize inductance.

The 1-ohm damping resistor is included to avoid oscillations in the discharge circuit. Such oscillations contribute to the rapid deterioration of the trigger tube, whose life is charge limited. Oscillations can also produce multiple discharges across the spark gap, destroying the required repeatability in the spark.

The trigger rate of the clock circuit is adjustable from several times per second to approximately once every five seconds. An interval of 2.5 seconds was used. The clock circuit also provides the trigger signal used in processing data from the receiving instrumentation.

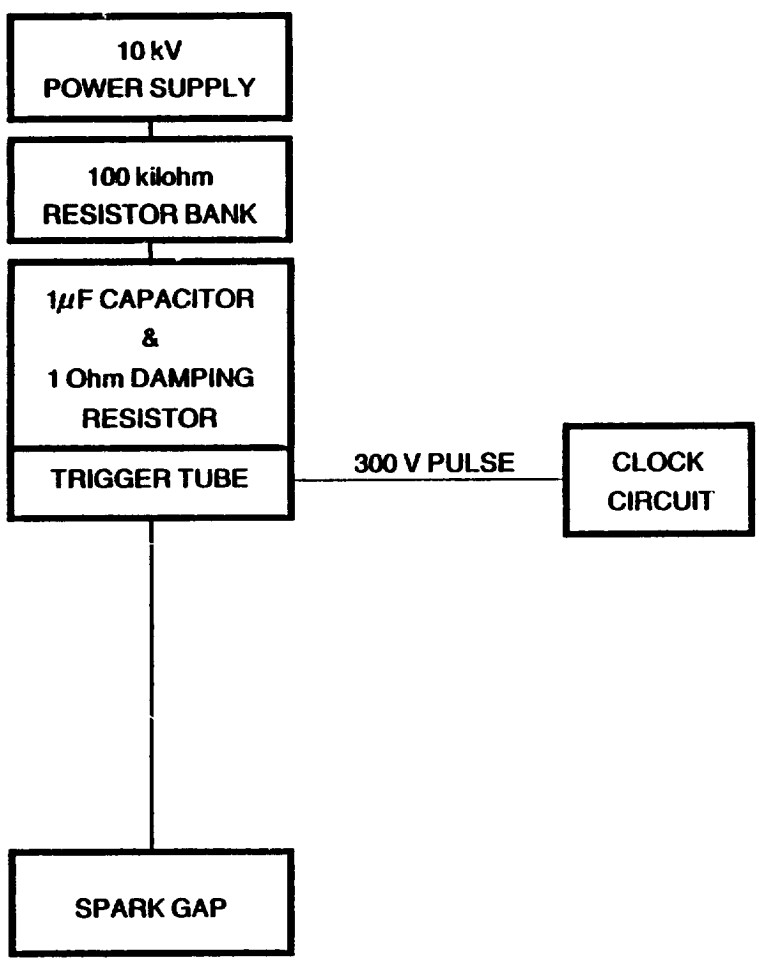

a. ELECTRICAL CONFIGURATION

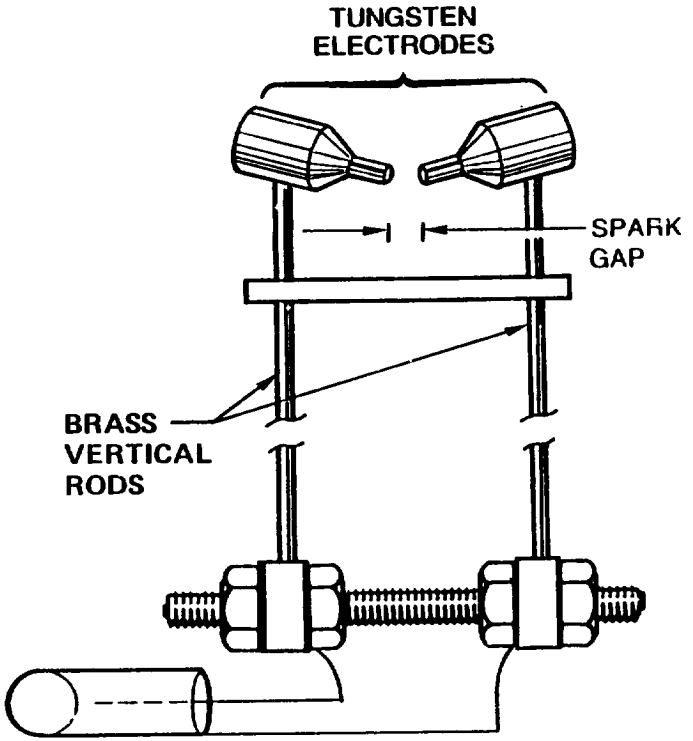

b. MECHANICAL CONFIGURATION

FIGURE 6. SPARK SOURCE.

The physical components of the spark source are also shown schematically in Fig. 6. On the central insulating post are the two electrical connections to the discharge circuit. The circuit is then completed through the brass vertical rods and the connecting washers, into the horizontal tungsten electrodes, and finally across the spark gap. A stiffener stabilizes the gap length. In use, the gap size is set at 1 mm.

4.2.2 Acoustic pulse

In general, when very intense spark sources are utilized, propagation in the vicinity of the source becomes nonlinear. However, early investigation under this program indicates that nonlinearities do not appear to affect the propagation in the region between the source and receiver microphones in this experiment and we therefore restrict our analysis to linear theory. A review of the propagation of a nonlinear pulse will, however, provide insight into the character of the measured source spectrum.

Immediately after spark discharge, an abrupt positive pressure pulse begins to propagate outwards from the spark, followed by a rarefaction. Very quickly, the leading edge of the positive pulse builds up into a shock wave, with rise time on the order of several microseconds. Figure 7 illustrates such a shock wave at distances of 0.5 m and greater, for a source that is similar to that used in this study. These waves are often called N-waves, because of their general shape. Pressure histories are shown at increasing distances from the source.

For intense sparks, such a shock is fully formed within a centimeter or so from the spark. Once formed, the shock shape is independent of the precise spark characteristics; all shocks assume roughly the shape presented in the figure.

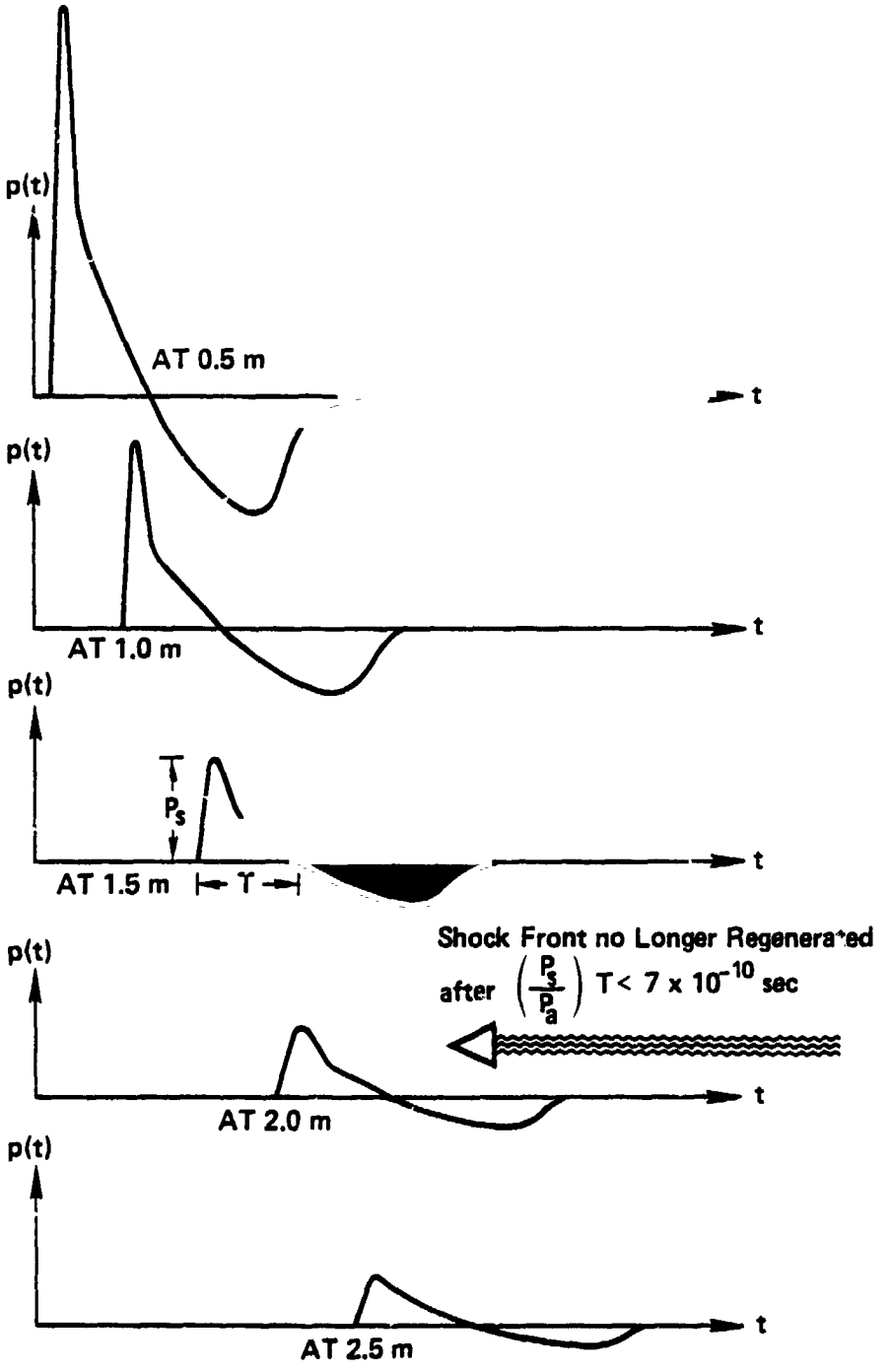

SOURCE: KLINKOWSTEIN [13]

FIGURE 7. DECAY OF SHOCK FRONT WITH INCREASING PROPAGATION DISTANCE.

Formation of the shock occurs because the speed of sound is greater in the areas of acoustic compression (the crests) than it is in the areas of rarefaction (the troughs). The greater sound speed with increasing pressure in the positive pulse causes minor perturbations to rush toward the highest pressure part of the pulse, thus building up to an abrupt shock front, which then stabilizes as energy is dissipated across the shock front.

The time history of a shock can be described by the two parameters shown in Fig. 7: the peak overpressure p_s and the half-duration T. The overpressure decreases with time at a greater rate than 6 dB per distance doubling, especially very near the source, while the half-duration T increases with time. For a spherically spreading shock [13]

$$\frac{P_s(r)}{P_a} = \frac{(P_s)_0}{P_a} \left(\frac{r_0}{r}\right) \left\{1 + k \ln \left(\frac{r}{r_0}\right)\right\}^{-1/2} \tag{1}$$

$$\frac{T}{T_0} = \left\{1 + k \ln \left(\frac{r}{r_0}\right)\right\}^{+1/2} \tag{2}$$

where $(P_s)_o$, r_o, P_a and k are constants.

Again, Eq. 1 indicates that the overpressure decreases faster than 1/r by the factor in the brackets.

While the shock is propagating, the dissipative mechanisms discussed in Sec. 3.3 are continually extracting high-frequency energy from the propagating wave. However, the same sound-speed phenomena that caused the shock initially to form, continue to reform the shock. They cause an energy "transfer" from low to high frequencies, to preserve the shape of the shock front. Once the product P_s/P_a times T drops below approximately 7×10^{-10} sec, the shock front no longer regenerates itself. Instead, the propagation reverts to linear and the dissipative mechanisms begin to prevail.

The replenishment can be observed directly by examining the spectra of such shocks. A spectrum of an idealized N-wave is illustrated in Fig. 8. It consists of a broad maximum at mid frequencies, and a series of zeros and maxima at higher frequencies. Asymptotically, the spectrum envelope (dotted) approaches 6 dB/octave at low frequencies and -6 dB/octave at the highest frequencies, as shown.

The asymptotic envelope is shown for four successive times. As time increases from t to 2t to 3t to 4t, the peak shifts toward lower and lower frequencies. Also, the nulls (zeros) in the spectrum shift downward as the spark propagates. We note that the "zeros" in the spectrum of the idealized N-wave are a direct result of the fact that it is an odd function in time (i.e., represented only by a Fourier sine series rather than a full Fourier series). Since the excitation used in this study is not an idealized N-wave, we do not expect the regular occurrence of zeros. In addition, the use of 1/3-octave bands rather than narrow bands, as was used in this study, suppresses remaining zeros. Figure 9 presents the spectrum of the spark measured at a location .3 m directly above the spark source.

From an earlier project on which the same spark source was used, it is known that the short-term repeatability of the spark source averages 0.6 dB in 1/3-octave bands in the range of 10 to 90 kHz. Long-term repeatability measured in 1/3-octave bands over a one-month period of active use averaged 1.8 dB.

4.3 Ground Impedance

The current program considers two limiting values of ground impedance, the first being a model of full-scale asphalt and the second being a model of grassland. For the asphalt, the impedance is high and a rigid ground plane appears to suffice. For the grassland, we must find a proper match for the acoustic impedance of the full-scale grassland (though at frequencies higher by the scaling factor: 100 in this case).

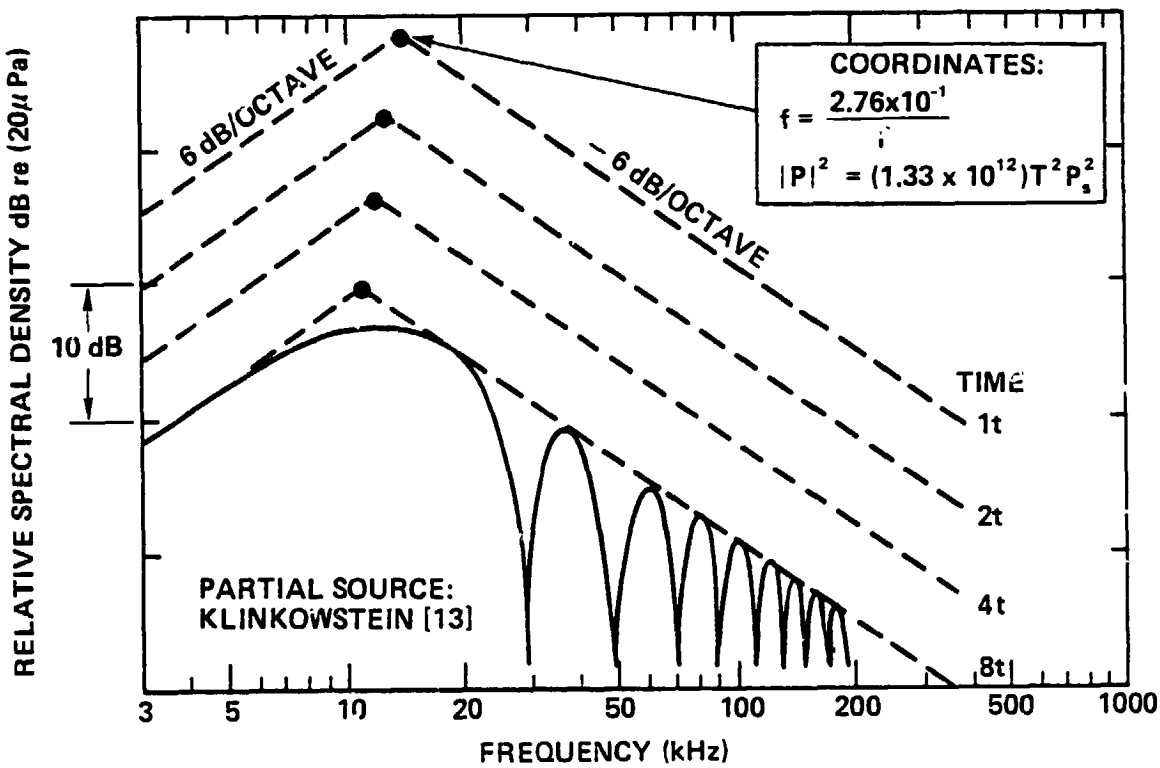

FIGURE 8. NARROW-BAND SHOCK SPECTRUM OF N-WAVE.

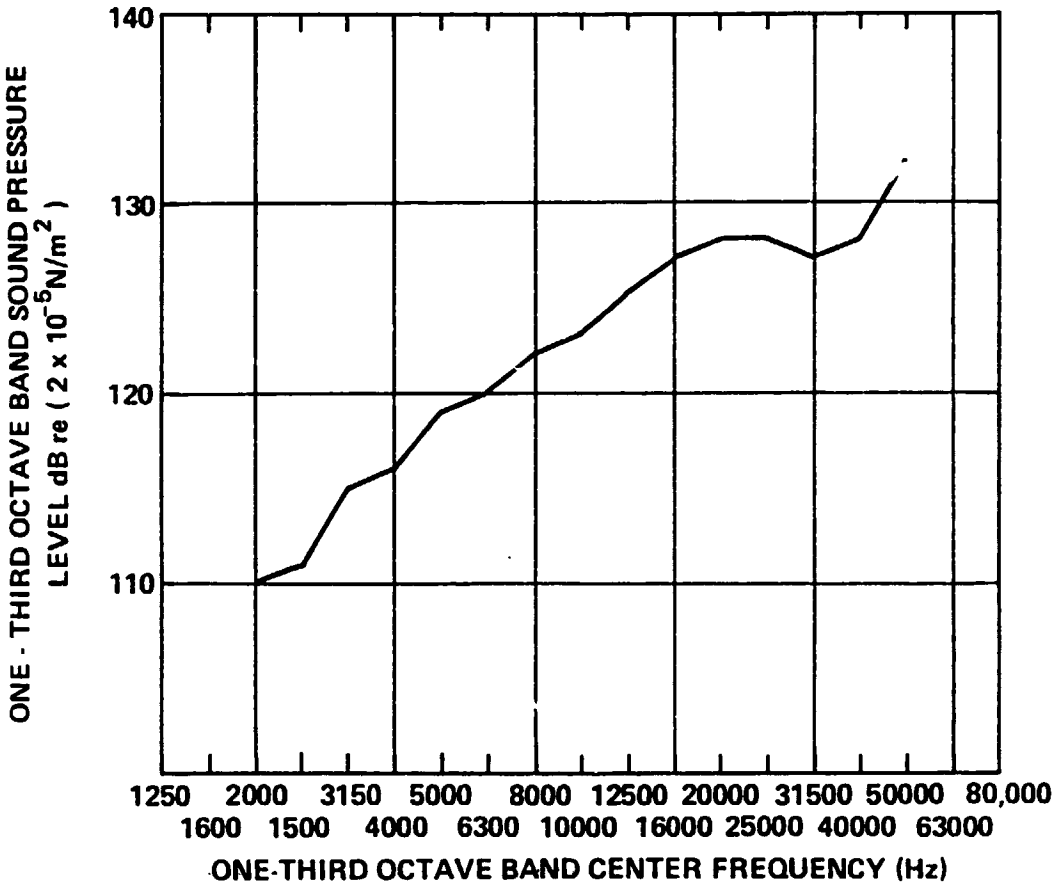

FIGURE 9. SPECTRUM OF SPARK SOURCE.

Finding new materials that preserve impedance at scaled frequencies is a significant material problem for absorptive surfaces. Fortunately, we were able to use material similar to that used successfully by Jones [8, 14] for 80-scale grassland.

4.3.1 The model hard ground

Full-scale asphalt (hard ground) was modeled by a 1.6-mm (0.063-in) thick aluminum sheet.

Embleton's data [15] give the effective flow resistance σ of "asphalt, sealed by dust and light use" as 30,000 cgs rayls. This is the hardest ground surface catalogued by Embleton. With a scale factor of 100, this converts to σ of 3,000,000 cgs rayls, which we have used in the analysis.

We did not, however, verify that the aluminum sheet matched this σ, since reflection from such hard surfaces is very insensitive to actual surface hardness. For these high-impedance surfaces, we have assumed that the reflection coefficient is unity (without phase shift) for all angles of interest.

4.3.2 Model grassland

Jones's scaled grassland material consists of 2.5-cm thick extruded polystyrene (Type RM as manufactured by Dow Chemical) with light tissue paper glued to its surface. The points in Fig. 10 are Jones's impedance data, unscaled.

In App. D, the acoustical effects of impedance are condensed into the so-called "effective" flow resistance σ. Use of the real-number σ simplifies the mathematics, compared with use of the complex-impedance η. From App. D,

$$\mathrm{Re}(\eta) = 1 + 9.08\ (f/\sigma)^{-0.75}$$

$$\mathrm{Im}(\eta) = 11.9\ (f/\sigma)^{-0.73} \quad .$$

With these equations, each of Jones's data points yields one estimate of σ. The mean of the 24 values of σ is 17,400 cgs rayls, with a standard error of 2,300 cgs rayls. With 95% confidence, therefore, the effective flow resistance of the scaled grassland is

17,400 ± 4,600 cgs rayls.

Note that for the impedance to be independent of scale, σ must scale linearly with frequency, per the equations above. Since Jones's scale factor was 80, his model grass scales to a full-scale σ of 218 ± 58 cgs rayls. Embleton [15] catalogues grass with σ between 150 and 300 cgs rayls, an excellent match to Jones's model grass, at 80-scale.

With a scale factor of 100, as used here, this material scales to 174 ± 46 cgs rayls, which still lies within Embleton's range.

It is of interest to utilize the two equations above to reconstruct impedance at all frequencies, from the average value of σ. This has been done in Fig. 10, where the results are compared to Embleton's impedance of full-scale grassland, scaled upward by a factor of 100. The match seems adequate, though it is not as good as that for a scaling factor of 80.

In subsequent comparisons of theory against data, we have used this scaled value of σ, derived from Jones's data. Appendix D presents equations for calculating the Insertion Loss (IL) associated with reflections from finite-impedance ground.

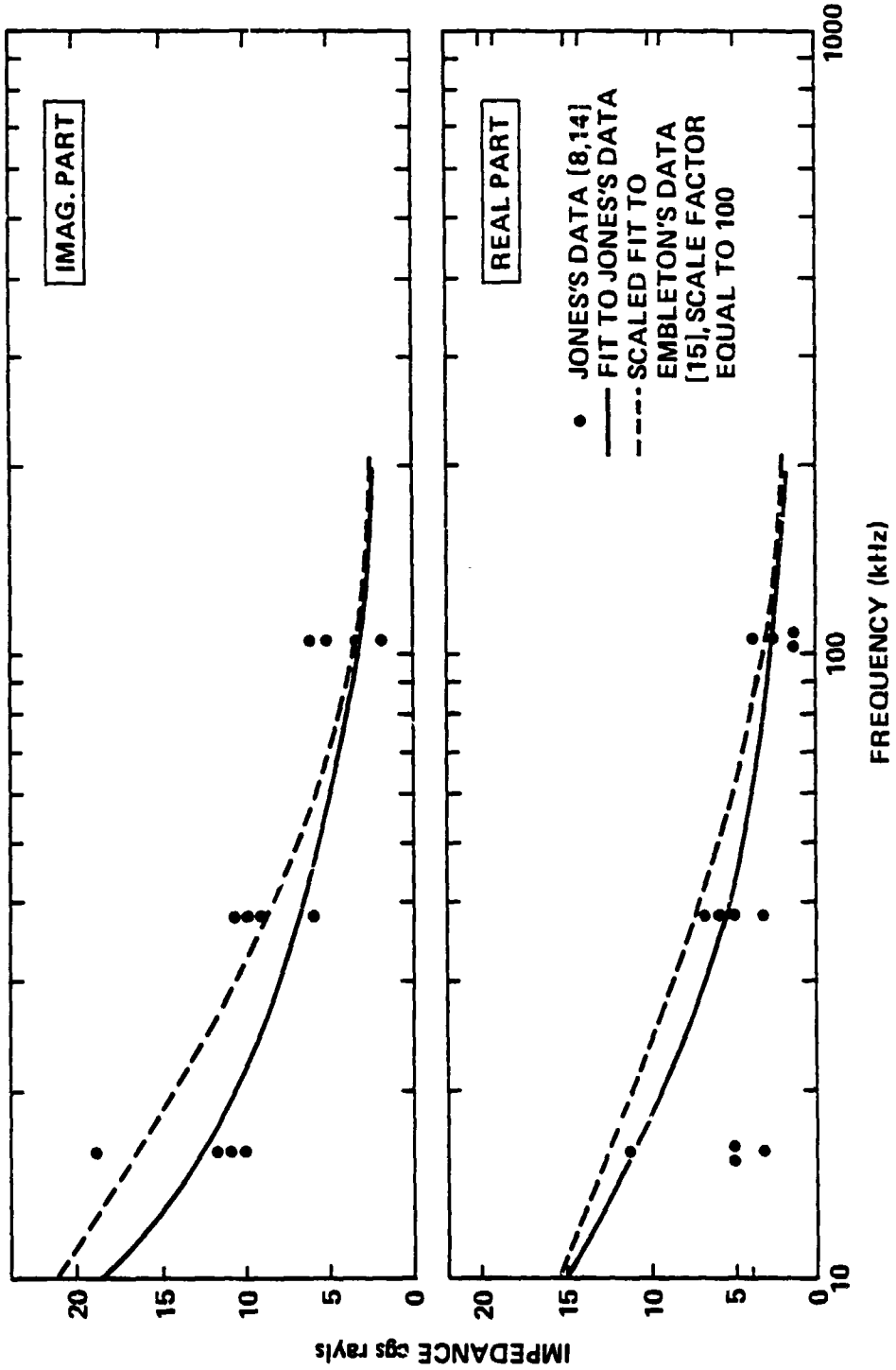

FIGURE 10. SC[illegible]-GROUND IMPEDANCE.

4.4 Data Acquisition System

4.4.1 Flow field data

A longitudinal section of the test geometry is shown in Fig. 11. Profiles and rms turbulence intensity were taken at the entrance to the test section (station 0; turntable leading edge), and at the midpoint (station 4; turntable centerline), and at the end of the test area (station 8). When the "hill" was in place, measurements were also taken at stations 2 and 6. Figure 12 shows turbulence data at two stations along the length of the test section. Note that the turbulence is relatively insensitive to position. Figure 13 summarizes the velocity profile data and provides the input for later calculations of refraction. Several points are noteworthy in these data. Figure 13 illustrates the dramatic effect of the "hill" on the mean-velocity profile. Note in Fig. 13 that the reversal in the sense of the velocity profile near the hill top could provide a potential flanking path for upstream-propagating sound to refract over the hilltop into the area that would normally be in a shadow.

4.4.2 Acoustic data

The acoustical measurement system in the wind tunnel employs a total of three microphones - one 0.3-m directly above the spark and two others at a distance of 2.2 m from the spark gap at various heights above the ground plane. To accommodate the high sound pressure at 0.3 m from the spark, a 3.2-mm microphone is used. This small diameter microphone also provides the required high frequency response. The two microphones at 2.2 m are 6.4 mm in diameter for better sensitivity and lower equivalent pressure noise floor.* With the attachment of nose cones, proper frequency

---

*Note that the two different size microphones (reference and receptor) have significantly different directional characteristics.

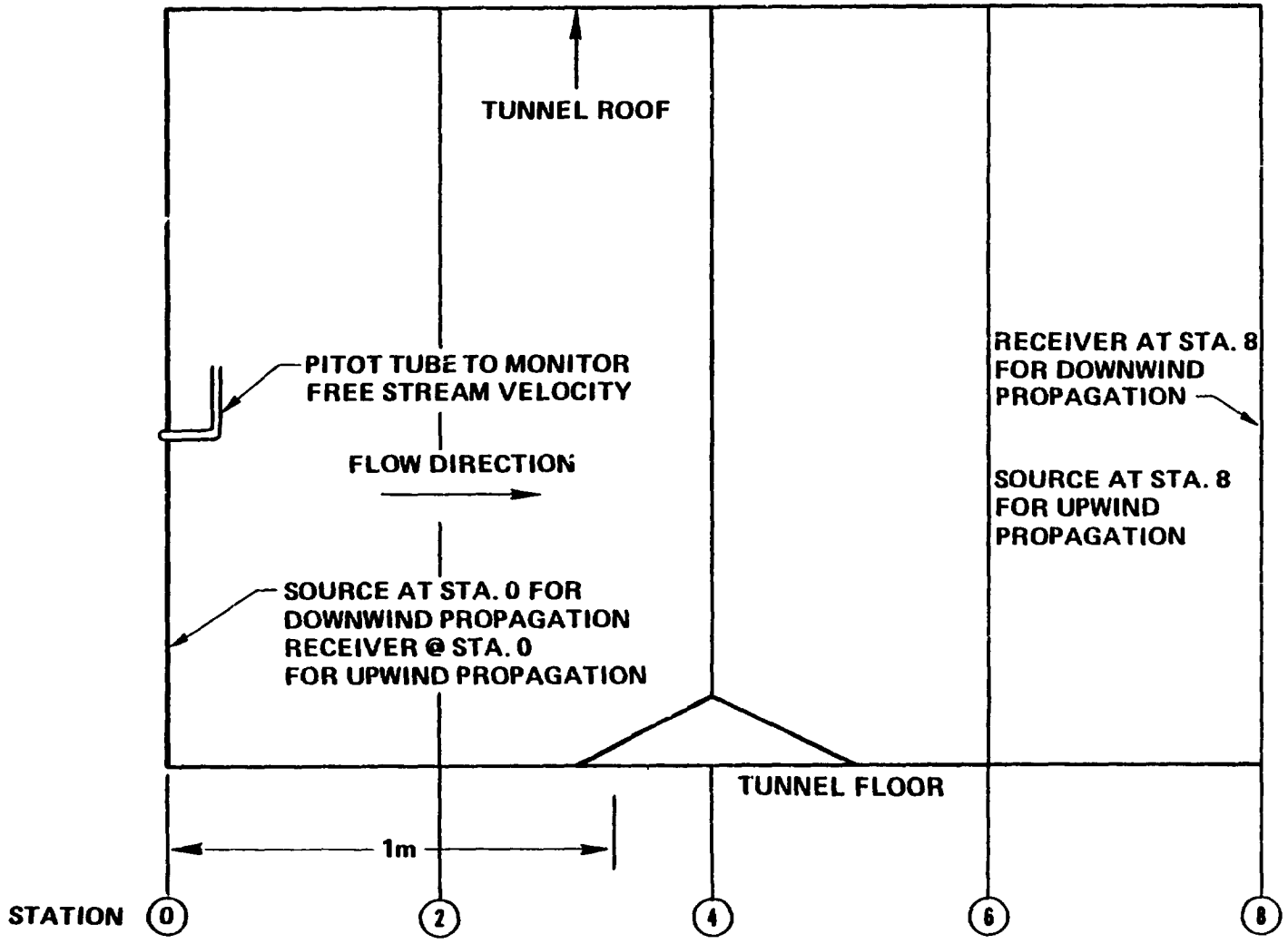

FIGURE 11. LAYOUT OF TEST SECTION FOR FLOW MEASUREMENTS.

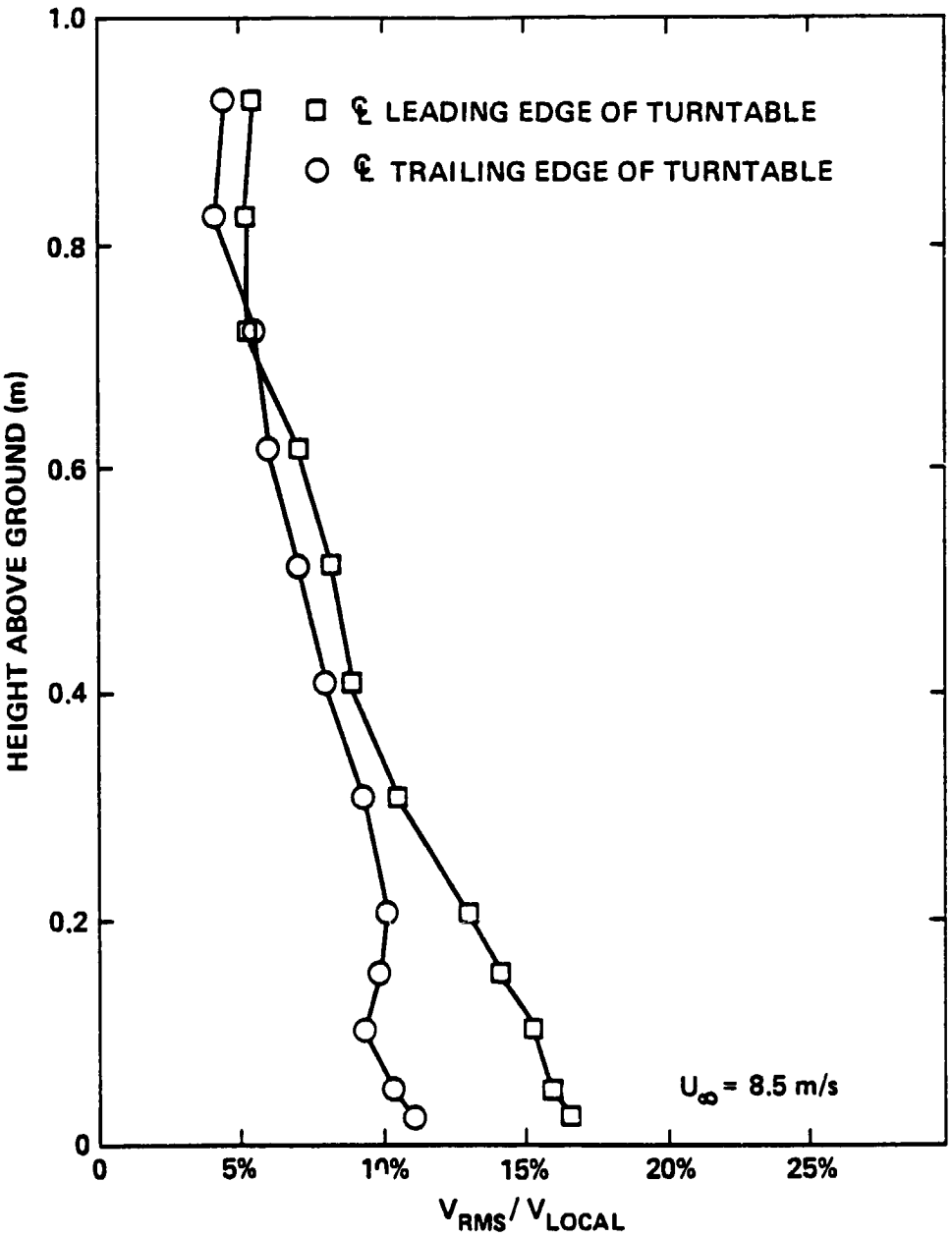

FIGURE 12. TURBULENCE DATA FOR FLAT TERRAIN AND REFERENCE VELOCITY OF 5.75 m/s.

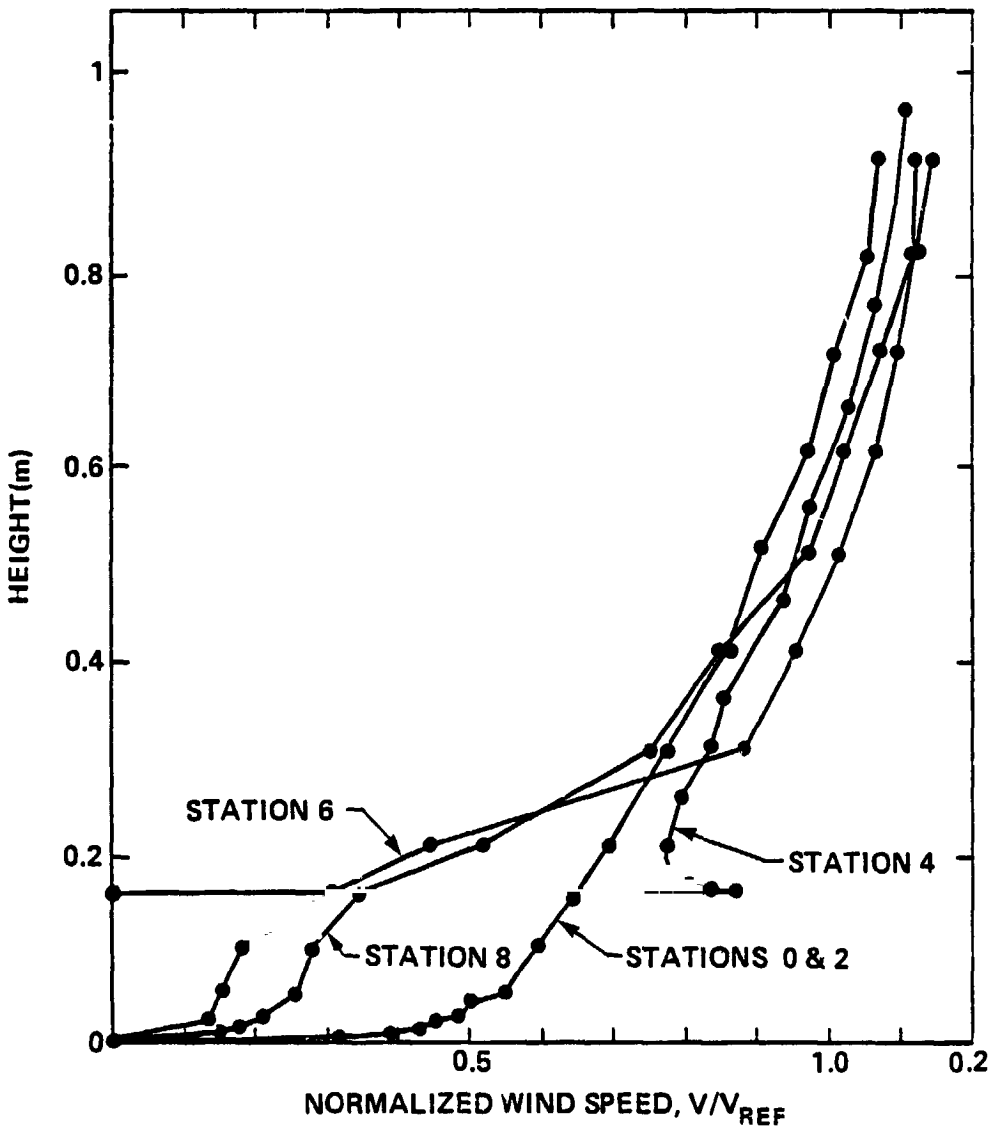

FIGURE 13. MEAN VELOCITY PROFILES FOR SET-UP WITH TWO-DIMENSIONAL 15.24 cm HILL.

response is achieved and the influence of wind-generated pressure fluctuations is reduced. The microphones were installed on pre-amplifiers and the signals were fed through signal-conditioning amplifiers to a seven-channel tape recorder. The high-pass filter on the amplifiers was set at 100 Hz to reduce unwanted DC and very low frequency signals. The tape recorder was set up with three of the seven channels operating in direct record (DR) mode and the other four in FM mode. The acoustic signals were fed to the three DR channels; one FM channel was used to record the electrical trigger signal from the clock circuit. The trigger signal was recorded to synchronize the data analysis. At 76 cm/s tape speed, the tape recorder has an upper frequency response of 150 kHz and 40 dB signal-to-noise (S/N) ratio on the three DR channels.

For each test condition, the individual gains on the amplifiers were adjusted to optimize the S/N ratio on the tape recorder. Typically, scope photos were taken of the signals being fed to the tape recorder. A typical scope photo is shown in Fig. 14. The uppermost trace represents a slice of 20 ms in the signal and the lower trace represents a 20-to-1 expansion of the signal in the vicinity of the first peak. The duration of each tape recording was set to approximately two minutes, so that at least 40 sparks were captured for each run. Dry-bulb and wet-bulb measurements at 0.08 m above the ground plane were taken every two hours during data acquisition.

4.5 Reduction of Experimental Data

At the conclusion of the data-acquisition stage, 27 reels of tape had been recorded. A commercial analog-to-digital converter and FFT software package were customized to analyze the tapes. Customization involved altering the sampling rate, waveform and spectrum file management capability, internal triggering of the microcomputer, and use of a 256-line FFT. The data-reduction procedure is presented in the following paragraphs.

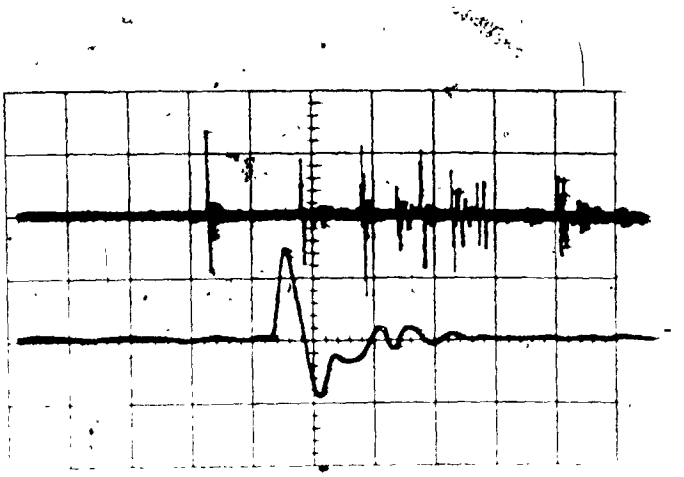

FIGURE 14. SCOPE PHOTOGRAPH OF SPARK SIGNAL.

Vertical scale
both traces: 0.5 V/div

Horizontal scale
top trace: 2 ms/div
bottom trace: 0.1 ms/div

Analog tapes were played into a microcomputer one channel at a time, at a playback speed of 19 cm/s to match the frequency response of the A/D converter to the upper frequency of interest. The trigger signal recorded from the spark's clock circuit was connected internally in the computer, to act as an initiating pulse for waveform acquisition. The analog signal was connected to the input of the A/D converter. Input gain and time delay were selectable from the computer keyboard. Upon arrival of the trigger pulse, the computer waited a number of time-delay units proportional to the acoustic pulse travel time, then acquired 1024 waveform points and stored them on diskette memory. The time delay was chosen so that the arrival of the first pulse from the spark occurred approximately 100 to 200 points after the beginning of data acquisition. For each test condition, at least 40 source-spark, time-history waveforms were stored on diskette.

After digitization of the time waveforms for each selected test condition, the FFT algorithm was loaded into computer memory and the spark waveforms were individually processed. Waveform editing was possible through use of "begin" and "end" cursors to isolate the portion of the signal required for FFT computation. After computation, the FFT of each spark was stored on diskette memory.

The result is a set of 40 FFT spectra for the reference microphone (0.3 m above the spark source) and a set of 40 FFT spectra for the receptor microphones (2.2 m from the spark), all stored on one diskette. Individual spectra from a 40-spectra block were fed through a program that sums the constant-bandwidth line spectra in each 1/3-octave band and stored the resultant 1/3-octave band sound pressure levels in an array. We note that this procedure introduces inaccuracies in the lower 1/3-octave bands. The lowest 1/3-octave band computed was 2 kHz (scaled frequency 20 Hz). If lower frequencies are required, the original data can be band-limited and then sampled at a lower rate to improve resolution. When all individual spectra are

summed into 1/3-octave bands and loaded into the array, the program searched through the array in each 1/3-octave band and computed the minimum, maximum, and mean level in each band, plus the standard deviation about the mean. An example of the program's output is shown in Fig. 15.

4.6 Summary of Test Conditions

The scale model test program was designed to systematically vary parameters of interest and determine the relative effects. The parameters varied during these tests were:

- Wind direction
- Ground impedance
- Source height
- Receiver height
- Barrier height
- Wind speed.

Two wind directions were tested with the receiver microphones first downwind and then upwind from the spark source. The ground impedance was initially "hard" (a 1.6-mm thick aluminum sheet) and then changed to a "soft" (finite-impedance) surface. These ground surfaces are described in Sec. 4.3. The heights of the spark gap above the ground plane were 0.013 m (designated 0+), 0.15 m, and 0.3 m, to represent actual source heights of "ground level," 15 m and 30 m. Receiver heights of 0.013 m (designated 0+), 0.038 m, 0.076 m, and 0.15 m were used to represent actual heights of "ground level," 3.8 m, 7.6 m, and 15 m. Acoustic data were acquired without a barrier, and with 0.15 m barriers, representing 15-m high ridges. The last parameter, wind speed, was chosen to be independent of scale. Its values were 2.5 m/s, 5.0 m/s, and 8.8 m/s.

R153.7 SOFTGROUND 29FPS WIND UPWIND NO MTN SOURCE AT 6 IN RECEIVER AT 3 IN

THIRD OCTAVE BANDS

0.4	0.5	1.4	2	2.5	3.15	4	5	6.3	8	10	12.5	16	20	25	31	40	50	63	80
91	90	82	90	94	98	99	102	103	104	105	105	106	103	102	102	103	101	100	97
95	95	95	95	95	99	99	102	103	104	106	105	105	102	104	103	104	101	99	98
90	90	90	90	91	96	97	99	100	102	103	103	103	101	102	101	101	97	99	94
89	90	92	94	95	99	100	102	102	104	105	106	105	103	105	104	104	100	102	99
83	90	93	94	95	97	98	99	100	102	104	103	103	102	104	102	103	99	101	99
90	91	91	89	82	96	97	99	100	102	103	104	104	101	101	99	100	96	93	95
94	94	95	95	95	97	98	100	101	102	103	103	104	103	102	101	102	98	100	98
96	96	95	94	92	98	100	102	103	105	106	104	104	105	107	104	104	100	101	98
87	85	84	89	90	95	96	98	100	101	103	103	103	99	98	98	98	94	93	92
93	93	92	93	95	98	99	102	103	104	106	105	105	104	107	105	106	101	99	99
94	93	92	91	92	96	95	99	100	101	103	103	102	100	100	98	99	96	96	92
90	91	91	87	91	99	100	102	103	105	106	105	105	104	106	104	105	100	99	98
92	93	93	91	89	98	99	101	102	103	104	103	99	105	106	103	102	97	101	96
94	92	85	74	90	94	97	99	100	102	104	103	101	102	103	101	101	97	98	97
87	88	89	90	90	95	97	99	100	102	103	103	103	101	104	101	102	97	98	97
93	94	94	93	91	98	99	101	102	104	105	105	105	104	105	103	103	99	99	94
90	90	91	90	86	95	97	99	101	102	103	104	104	102	101	100	101	97	98	96
94	94	93	91	88	96	97	99	101	102	103	103	103	100	101	100	100	96	95	95
92	95	96	94	92	97	98	101	102	104	105	105	103	103	105	103	104	98	98	98
92	92	94	95	96	100	100	102	102	104	105	105	106	104	104	102	103	99	97	98
86	89	88	87	91	95	96	99	100	102	103	103	103	102	102	101	102	97	98	97
95	94	94	92	92	97	97	99	101	102	104	104	104	103	103	101	101	98	100	97
97	96	95	93	94	97	97	99	100	101	102	102	100	101	103	101	100	97	97	96
83	90	92	92	88	94	97	99	100	102	103	103	103	99	102	101	102	97	95	95
96	96	95	93	91	96	97	99	100	102	104	104	104	104	103	100	101	98	100	98
90	91	91	91	94	99	100	102	102	104	104	104	105	102	105	103	103	100	100	98
90	91	93	94	95	98	99	102	103	104	106	104	101	106	108	105	104	99	101	99
81	85	89	92	93	95	97	99	100	102	103	102	100	103	104	102	102	97	98	96
MINIMA																			
87	90	82	80	88	97	98	101	102	103	104	103	99	102	102	102	102	97	97	94
MAXIMA																			
103	102	101	101	101	103	104	106	107	108	110	110	110	110	110	108	109	105	107	105
MEA.																			
94	95	95	95	95	100	101	104	105	106	108	107	107	106	107	105	106	101	102	100
STANDARD DEVIATIONS																			
4	4	4	4	3	2	2	2	2	2	2	2	3	2	2	2	2	2	3	3

FIGURE 15. EXAMPLE OF PROGRAM OUTPUT.

All parameter combinations could not be tested within the project resources and the program was reduced to the following test conditions:

- Downwind, hard ground, spark at 0+ (all other parameters varied through full range)
- Upwind, hard ground (all other parameters varied through full range)
- Upwind, soft ground (no barrier - all cases tested) (0.15 m barrier - spark at 0+ and 0.15 m height tested).

The test matrix and data log are presented in App. A.

5. ANALYTICAL MODELS

A primary purpose of this study was to evaluate the applicability of scale model tests for long-range low-altitude sound propagation research. The evaluation consisted of a comparison of the experimental results with prediction from analytical models. Models that have been validated by full scale experiment were clearly the first choice. Unfortunately, for many of the cases of interest here, there were no validated models. We therefore had to develop approximate analytical models for these cases. We recognize, however, that discrepancies between analysis and experiment, when we use the newly developed models, may be due either to (1) deficiencies in scale-modeling or (2) deficiencies in the analytical model itself.

In the following paragraphs we describe the newly created models in detail to underline the assumptions and to point out limitations. Where thought necessary, suggestions are made for development of more advanced models.

For the analysis of these atmospheric effects, we use three analytical models: refraction from knowledge of wind gradients; level reduction within diffraction shadows; and level reduction within soft-ground shadows. The appropriate equations appear in Apps. B, C, and D. Combinations of these mathematical models are used to predict each of the atmospheric effects.

Quantizing the effects of atmospheric turbulence is beyond the scope of this analysis, although its effects may influence the experimental results.

5.1 Creation of Refraction Shadow Upwind (Fig. 1, Effect 1)

Of critical importance to upwind refraction is the source ray that just grazes the ground before refracting further upward. This ray is the nominal boundary of the upwind refraction shadow. From a ray-acoustic point of view, no source rays penetrate this shadow.

Of course, the sound field cannot sustain a true discontinuity across this ray - from outside to inside the shadow. Transformation of the vertical geometry, as shown in Fig. 16, provides some insight into how this apparent discontinuity can be avoided. In effect, this vertical transformation has changed the refraction geometry to one of "diffraction" over a hill.

In the transformed geometry, rays that lie relatively close to the grazing ray transform as relatively straight lines; there, the diffraction model is applicable, at least to a first approximation.

In accordance with diffraction theory, the level reduction starts somewhat outside the shadow and increases dramatically as the shadow is entered. At the limiting ray itself, the level reduction is 6 dB; in essence, the entire bottom half of the wavefront is obscured by the hill.

Required then is the location of the grazing ray for the relevant source position. To transform vertically, this grazing ray is inverted, as shown in Fig. 17.

There is no precendent for transforming from refraction to diffraction in this manner. However, intuitively, the transformation preserves the physics close to the grazing ray, at least for the higher frequencies, where conditions far off the grazing ray have little influence. We also recognize that the diffraction approximation will tend to lose validity as the receptor deviates further from the grazing ray; for large deviations, the actual ray path between the ground and the receptor is certainly not straight in the transformed geometry.

Success of this diffraction approximation also depends upon how well the resulting diffraction is modeled. "Wedge" diffraction will be satisfactory only if the transformed ground plane approximates a wedge - that is, only if refraction is extreme near the ground.

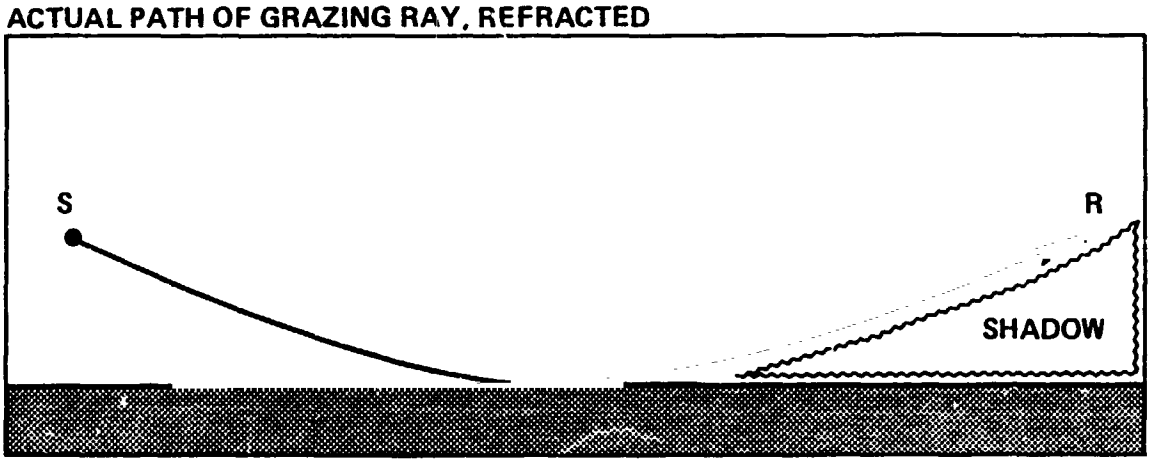

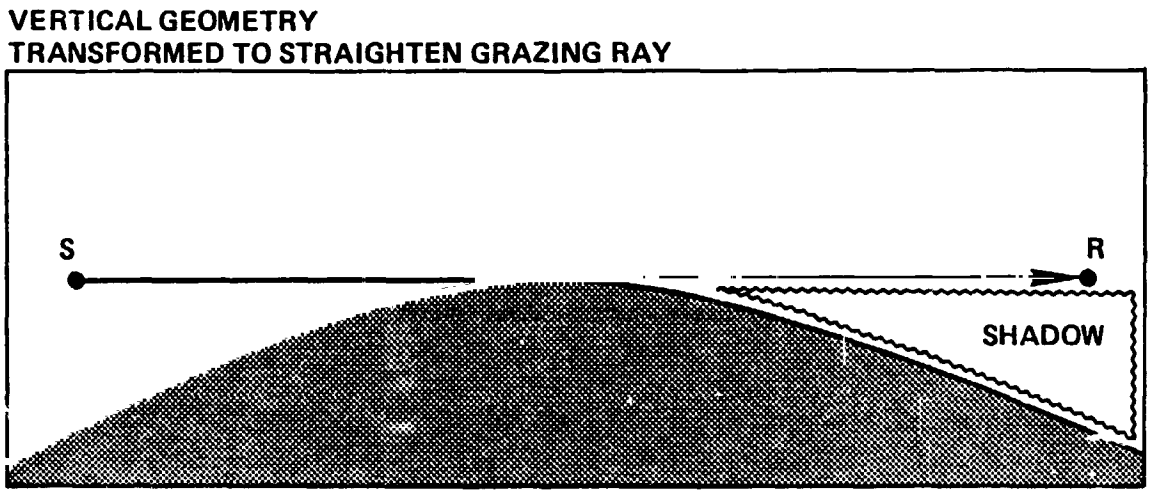

FIGURE 16. TRANSFORMATION OF VERTICAL GEOMETRY TO STRAIGHTEN GRAZING REFRACTED RAY.

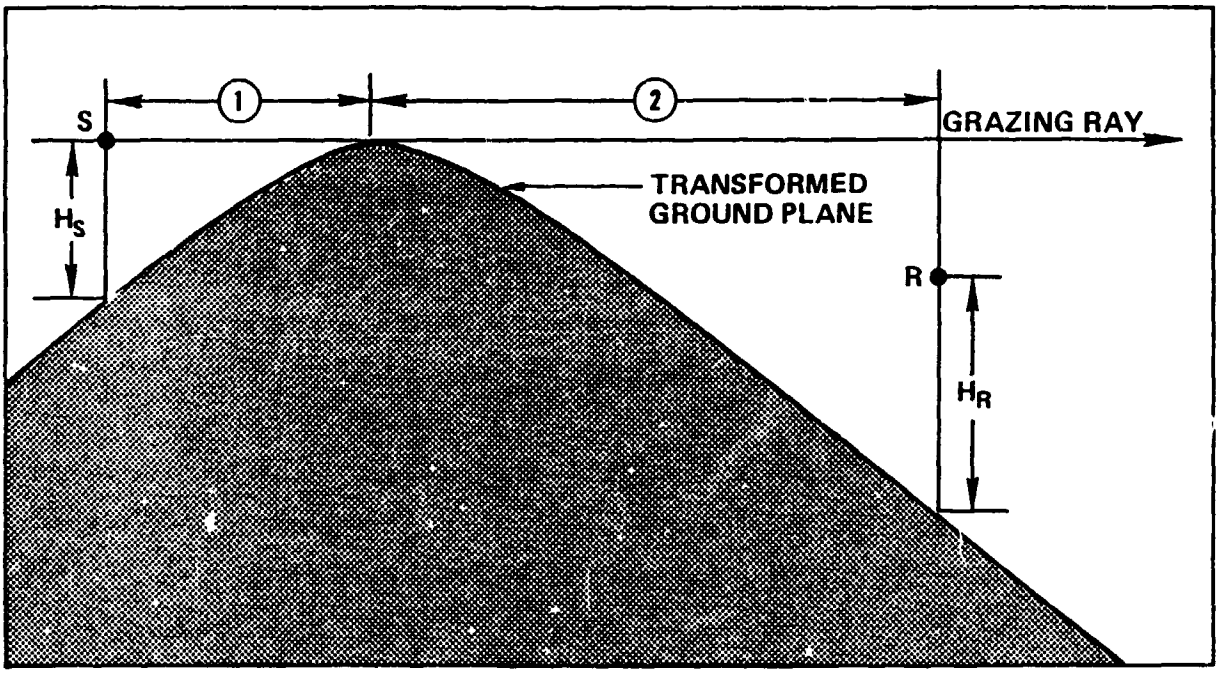

H_S YIELDS (1)

(1) PLUS S/R RANGE YIELDS (2)

(2) PLUS H_R YIELDS POSITION OF R

FIGURE 17. LOCATION OF TRANSFORMED RECEIVER POSITION.

This transformation of refraction into "diffraction" is only approximate and is used because no more accurate theory exists.

In summary, the level reduction within the refraction shadow, referenced to free-field propagation, is computed by:

- Locating the sound ray that emanates from the source and just grazes the ground, using App. B
- Transforming vertically, to convert this grazing ray into a straight line
- Locating the transformed receptor, as shown in Fig. 17
- Computing the diffraction IL from App. C.

These steps result in the IL of the ground in the presence of wind. To obtain the effect of the wind alone, this IL must be compared to the no-wind IL with the same geometry. Therefore,

- Compute the effect of the ground alone, from App. D, without wind
- Subtract this no-wind result from the IL with wind, to obtain the effect of the wind alone.

5.2 Creation of Soft-Ground Shadow Upwind (Fig. 1, Effect 2)

The effect of the ground, with wind, is computed by:

- Computing the ground/surface portion of the no-wind solution, from App. D - both magnitude and phase
- Locating the refracted sound ray that emanates from the source, reflects from the ground (with angle of reflection equal to angle of incidence), and intercepts the receptor
- Observing (1) the grazing angle between this ray and the ground, and (2) the refracted path length from source to receptor, reflected from the ground

- Relocating both the source and receptor vertically downward, preserve this grazing angle. These two new positions and the ground-reflection point define a triangle

- Locating the refracted sound ray that emanates from the source directly to the receptor, without reflection from the ground

- Observing the refracted path-length of this ray from source to receptor

- Subtracting the two refracted path lengths from source to receptor: one direct and the other reflected from the ground - to obtain the path-length difference

- Further relocating the source and receptor to (1) preserve geometric similarity with the triangle above, and (2) duplicate the path-length difference just computed. This results in a source/receptor/reflection triangle geometrically similar to the one above, but smaller. (As is obvious from Fig. 1, Effect 2, the wind has the effect of reducing the path-length difference between direct and reflected ray. This reduction in triangle size duplicates the reduced path-length difference, while preserving the reflection angles at the ground and also preserving the ratio between the source-ground distance and the ground-receptor distance. Moreover, the ratio between the reflected-ray length and the direct-ray length is also preserved, thus guaranteeing that the increased divergence of the reflected ray, relative to the direct ray, is preserved.)

- Computing the soft-ground IL from App. D, using this transformed geometry, but retaining only the direct and reflected terms, including their phases

- Combining these direct and reflected terms with the no-wind ground/surface term, preserving phase.

These steps result in the IL of the ground in the presence of wind. To obtain the effect of the wind alone, this IL must be compared to the no-wind IL with the same geometry. Therefore,

- Compute the soft-ground IL from App. D, without wind
- Subtract this no-wind result from the IL with wind to obtain the effect of the wind alone.

5.3 Elimination of Diffraction Shadow Downwind (Fig. 1, Effect 3)

The refraction model of App. B can be used to locate the refracted path between source and receptor. If this path misses the hill sufficiently, then diffraction has been flanked. The level within the former diffraction shadow is no longer reduced by diffraction.

5.4 Elimination of Diffraction Shadow Upwind (Fig, 1, Effect 4)

A diffraction shadow behind intervening terrain may possibly be flanked upwind, because of the strong anomalous wind gradient near the terrain peak. If the anomalous downward refraction is strong enough to overbalance the upward refraction along the rest of the sound path, this flanking will exist.

The refraction model of App. B can be used to locate the refracted path between source and receptor, over the top of the hill - if such a path can be found. If this path misses the hill sufficiently, then diffraction has been flanked. The level within the former diffraction shadow is no longer reduced by diffraction.

6. COMPARISON OF MODEL TESTS WITH ANALYTICAL PREDICTIONS

Three no-wind cases were first selected for analysis. These are:

- Propagation over flat, hard ground
- Propagation over flat, soft (absorptive) ground
- Propagation over a (soft-ground) hill.

Comparison of theory with experiment for these cases provides calibration of the experimental method, separate from any wind-induced effects.

Next, the data for maximum wind gradients, as presented in App. F, were used to analyze four wind-induced effects. These are:

- Creation of soft-ground shadow upwind (Effect 2).
- Elimination of diffraction shadow downwind (Effect 3)
- Elimination of diffraction shadow upwind (Effect 4)

Experimental results for each case were compared with results obtained from the previously described analytical models. The comparison and appropriate discussion are presented in the following paragraphs.

6.1 Sound Propagation Without Wind

6.1.1 Propagation over flat, hard ground

The geometries selected for propagation over flat, hard ground appear in Fig. 18. Note that the vertical scale is stretched 10-to-1, relative to the horizontal scale. The source-receptor distance for all selected geometries is 2.2 m. Three pairs of source/receptor heights were selected:

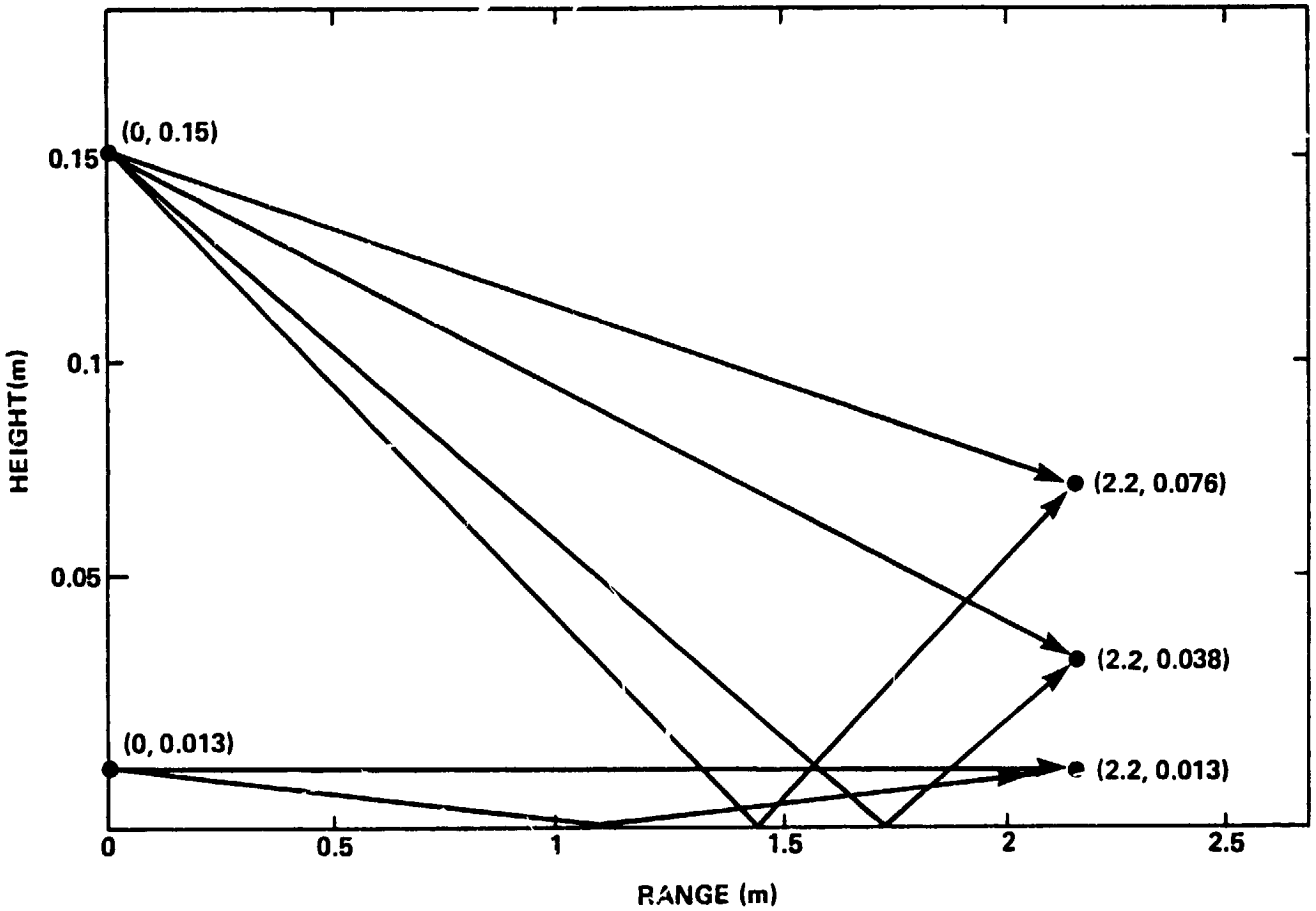

FIGURE 18. GEOMETRIES FOR PROPAGATION OVER FLAT, HARD GROUND.

0.15 m/0.076 m

0.15 m/0.038 m

0.013 m/0.013 m.

The 0.013 m height constitutes the smallest height that the spark-source could manage. It is labeled at 0^+ and corresponds to a full-scale height of 1.3 m.

For these geometries, App. D was used to calculate the IL of the ground, assuming the previously discussed effective flow resistance of 3,000,000 cgs rayls for the aluminum plate. Calculated ILs appear in Table 1.

Source height 0.15 m; receptor height 0.076 m

Figure 19 contains a comparison of the analysis with experiment for the 0.15-m source and 0.076-m receptor. Mean values obtained from experiment are represented by a solid line; theoretical predictions are shown as a dashed line.

At low frequencies, the analysis predicts a 6 dB pressure doubling, where direct and reflected waves constructively interfere. This pressure doubling is partially missing from the experimental results.

In the 16-kHz band, the analysis predicts a deep minimum due to destructive interference between direct and reflected rays.

At 16 kHz exactly, the analysis yields the following pressure contributions:

- Direct-wave pressure: 1 (since IL is normalized to this free-field pressure)
- Reflected-wave pressure: $0.983 \exp[i2\pi(0.492)]$
- Ground/surface-wave pressure: $0.0034 \exp[i2\pi(0.062)]$.

TABLE 1

ANALYSIS RESULTS: NO WIND

Terrain		Hard Flat	Hard Flat	Hard Flat	Soft Flat	Soft Flat	Soft Hill	Soft Hill
Source Height (m)		0.15	0.15	0.013	0.15	0.15	0.15	0.15
Receptor Height (m)		0.076	0.038	0.013	0.076	0.038	0.076	0.038
1/3-Octave-Band Insertion Loss (dB)	2.0 kHz	-5.8	-6.0	-6.0	-5.4	-5.7	5	6
	2.5	-5.7	-5.9	-6.0	-5.2	-5.5	5	6
	3.2	-5.6	-5.9	-6.0	-4.7	-5.2	5	6
	4	-5.3	-5.8	-6.0	-4.1	-4.9	6	6
	5	-4.9	-5.7	-6.0	-3.1	-4.3	6	7
	6.3	-4.2	-5.6	-6.0	-1.5	-3.5	6	7
	8	-3.1	-5.3	-6.0	1.2	-2.3	6	7
	10	-1.0	-4.9	-6.0	5.7	-0.6	6	8
	12.5	3.1	-4.2	-6.0	8.7	1.8	7	8
	16	26.0	-3.0	-6.0	1.9	5.5	7	9
	20	3.1	-0.9	-6.0	-2.0	6.3	8	10
	25	-3.4	3.3	-5.9	-3.5	2.5	8	11
	31.5	-5.8	22.2	-5.9	-1.8	-1.1	10	12
	40	-3.4	2.8	-5.8	5.4	-3.2	11	13
	50	12.9	-3.4	-5.7	-2.2	-3.1	12	15

Notes:

1. Negative ILs denote an amplification of the free-field sound level.

2. Hill is 0.15 m high.

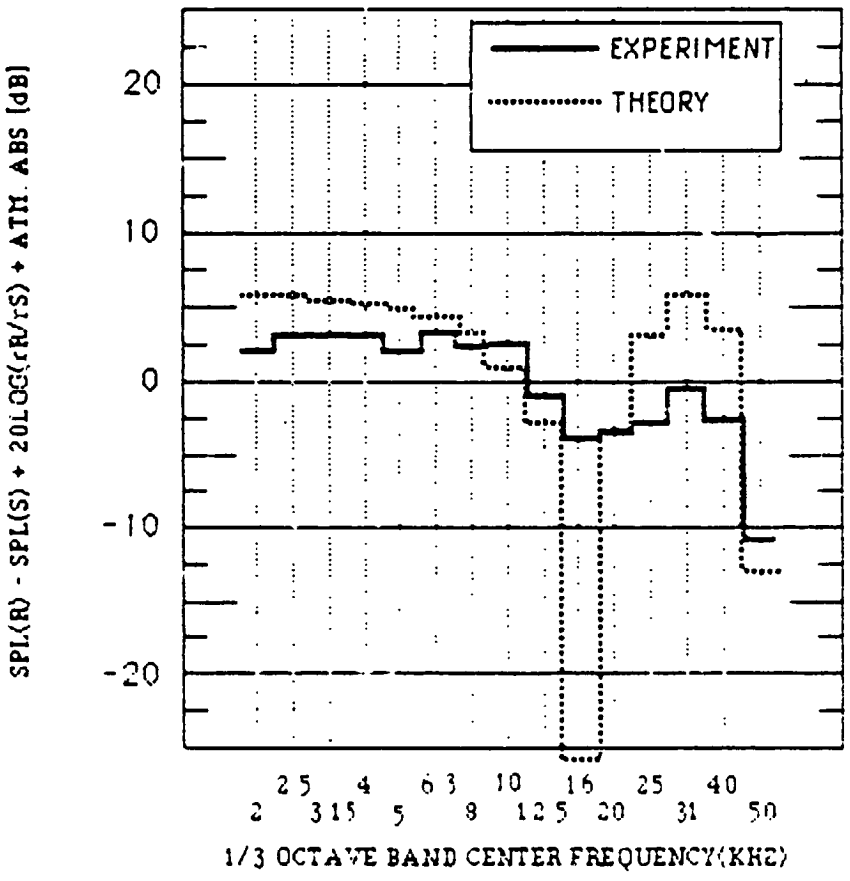

FIGURE 19. PROPAGATION OVER FLAT, HARD GROUND WITH NO WIND. (SOURCE HEIGHT .15 m, RECEIVER HEIGHT .076 m, DISTANCE 2.2 m.)

These pressure details point out that the reflected wave is nearly equal in magnitude to the direct wave, but out of phase with it by 0.492 wavelengths. Of this 0.492, only 0.003 is due to phase shift upon reflection; the remainder is due to the path-length difference between direct and reflected rays. Further, these details show that the ground/surface wave is of no importance.

The minimum present in the experimental results in the 16 kHz 1/3-octave band is not as deep as that predicted by theory for a number of reasons. In particular, in order for a direct and reflected signal to cancel each other to the point required for a 26 dB reduction the 2 signals must be within .5 dB of each other. Small variations in the directivity of the receiver microphone in the frequency range of interest may be greater than .5 dB, precluding the measurement of the predicted cancellation. In addition, system noise will tend to fill in the deep void.

Note also that complete destructive interference occurs only at one frequency within the 1/3-octave band, not throughout the entire band. For this reason, the 1/3-octave band calculations do not predict "no energy whatsoever" -- that is, "minus infinity" decibels. The analysis takes this effect into account, although it assumes an incident spectrum that is uniform across the 1/3-octave band. This assumption can lead to error in the following two ways. First, if the incident spectrum is concentrated around the frequency of destructive interference, then the analysis should falsely underpredict the destructive interference -- that is, the measured level should be lower than predicted. On the other hand, if the incident spectrum is concentrated away from the frequency of destructive interference, the opposite should happen -- the measured level should be greater than predicted. Therefore, this assumption concerning the incident spectrum may effect the results either way: either increasing or decreasing the measured destructive interference.

In the 31 kHz band, the analysis predicts constructive interference between direct and reflected waves, for a 6-dB increase in level. Some indication of this constructive interference occurs in the experimental results. In the 50-kHz band, the analysis again predicts destructive interference, though not as complete as before. In this band, the experimental results agree well with the analysis.

Source height 0.15 m; receptor height 0.038 m

Figure 20 presents the results of the comparison of experiment and analysis for the 0.15-m source and 0.038-m receptor. At low frequencies, the analysis again predicts a 6-dB pressure doubling which is now present in the experimental results.

In the 31 kHz band, the analysis predicts a deep minimum due to destructive interference. At 31.5 kHz exactly, the analysis yields the following contributions:

- Direct-wave pressure: 1
- Reflected-wave pressure: $0.966 \exp[i2\pi(0.488)]$
- Ground/surface-wave pressure: $0.0050 \exp[i2\pi(0.078)]$.

Of the 0.488 phase shift in the reflected wave, only 0.007 is due to phase shift upon reflection; the remainder is due to path-length difference. Again, microphone directivity variations and the system noise floor preclude us from achieving the theoretically predicted minimum.

Source height 0.013 m; receptor height 0.013 m

Figure 21 presents the comparison of experimental results with analysis for the 0.013-m source and receptor. At all frequencies, the analysis predicts a 6-dB pressure doubling. Pressure doubling is present in the experimental results at the lower frequencies, but tends to disappear at the upper. The experimental results also indicate that there is destructive interference in the 20- and 50-kHz bands.

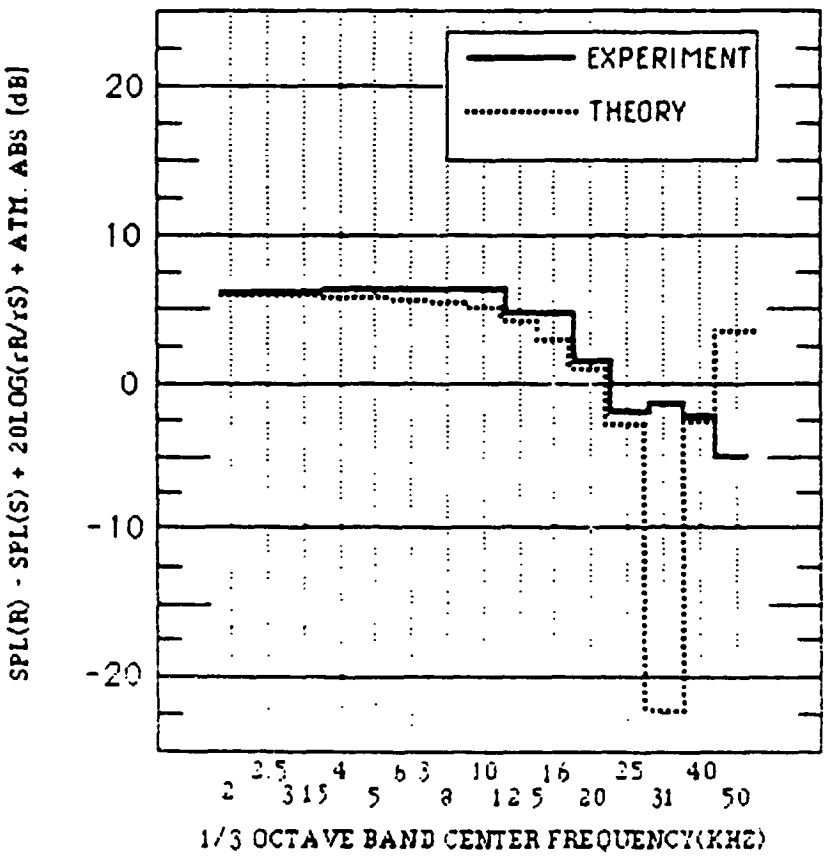

FIGURE 20. PROPAGATION OVER HARD, FLAT GROUND WITH NO WIND. (SOURCE HEIGHT .15 m, RECEIVER HEIGHT .038 m, DISTANCE 2.2 m.)

General discussion of hard-ground results

The destructive interference in the 16 kHz 1/3-octave band is not as pronounced in the experimental data as one would expect from the theory. In addition to the microphone directivity and noise floor causes, we have noted that for all data taken with the hard-ground aluminum plate, acoustic energy was detected before the arrival of the airborne pulse. This "pre-arrival" energy appears to the left of the main pulse in Fig. 14. We suspect that this is caused by an acoustic bending wave in the aluminum plate generated by the extreme pressure field near the spark source. This wave travels outward from the spark at the speed of bending waves in aluminum plate of this thickness. As the bending wave propagates in the aluminum plate, it constantly radiates a portion of its energy as sound. Since this speed is greater than the speed of sound in air, it arrives in the vicinity of the receptor microphone prior to the airborne energy.

Such anomalous energy at the receptor microphone would be insignificant in most bands, but highly significant in bands with expected destructive interference. In essence, the anomalous energy fills in these "zeros." A similar argument can be posed for the destructive interference in the 31-kHz band in Fig. 20.

Figure 21 also shows signs of destructive interference in the 20 and 50 kHz bands. For the given source/receptor geometry, this interference behavior could not be duplicated by the analysis for <u>any</u> value of the ground's flow resistance. At first glance, the analysis points toward the existence of a source at 0.75 m to achieve this interference behavior. This explanation is not feasible since it does not account for the interference near 50 kHz. We therefore attribute these differences again to the bending waves in the plate or to reflections from both the source-microphone supports and the receptor-microphone supports. All of these supports were reflective, and approximately 0.005 m in diameter: a troublesome size at these higher frequencies. Suggested for further study are additional measurements with

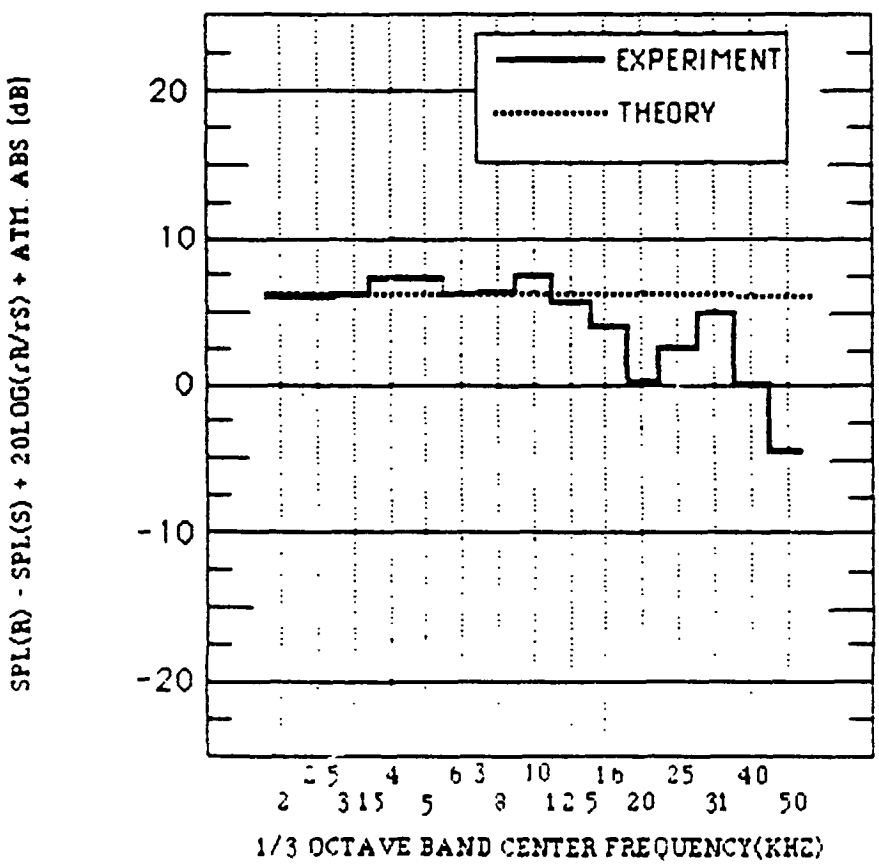

FIGURE 21. PROPAGATION OVER HARD, FLAT GROUND WITH NO WIND. (SOURCE HEIGHT .013m, RECEIVER HEIGHT .013 m, DISTANCE 2.2 m.)

these supports made acoustically absorptive. Because the geometry is so simple and the analysis so unambiguous, this situation is ripe for detailed diagnostic measurements.

In summary, the flat hard-ground data, without wind, indicate that:

- Future measurements should be made with all supporting rods acoustically absorptive
- Future hard-ground material should be damped to minimize bending waves.

6.1.2 Propagation over flat, soft (absorptive) ground

The selected geometries for propagation over flat, soft (absorptive) ground appear in Fig. 22. Two pairs of source-receptor heights were selected:

0.15 m/0.076 m

0.15 m/0.038 m.

For these geometries, App. D was used to calculate the IL of the ground, assuming an effective flow resistance of 17,400 cgs rayls, as previously discussed. Resulting ILs appear in Table 1.

Source height 0.15 m; receptor height 0.076 m

Figure 23 contains the comparison of experimental results with analysis for the 0.15-m source and 0.076-m receptor. At low frequencies, the analysis predicts a 6-dB pressure doubling. This pressure doubling is again partially missing from the experimental results.

In the 12.5 kHz band, the analysis predicts a moderate minimum, due to partially destructive interference between direct and reflected rays. This destructive interference at 12.5 kHz is seen in the experimental results. The match here is good. At 12.5 kHz exactly, the analysis yields the following pressure contributions:

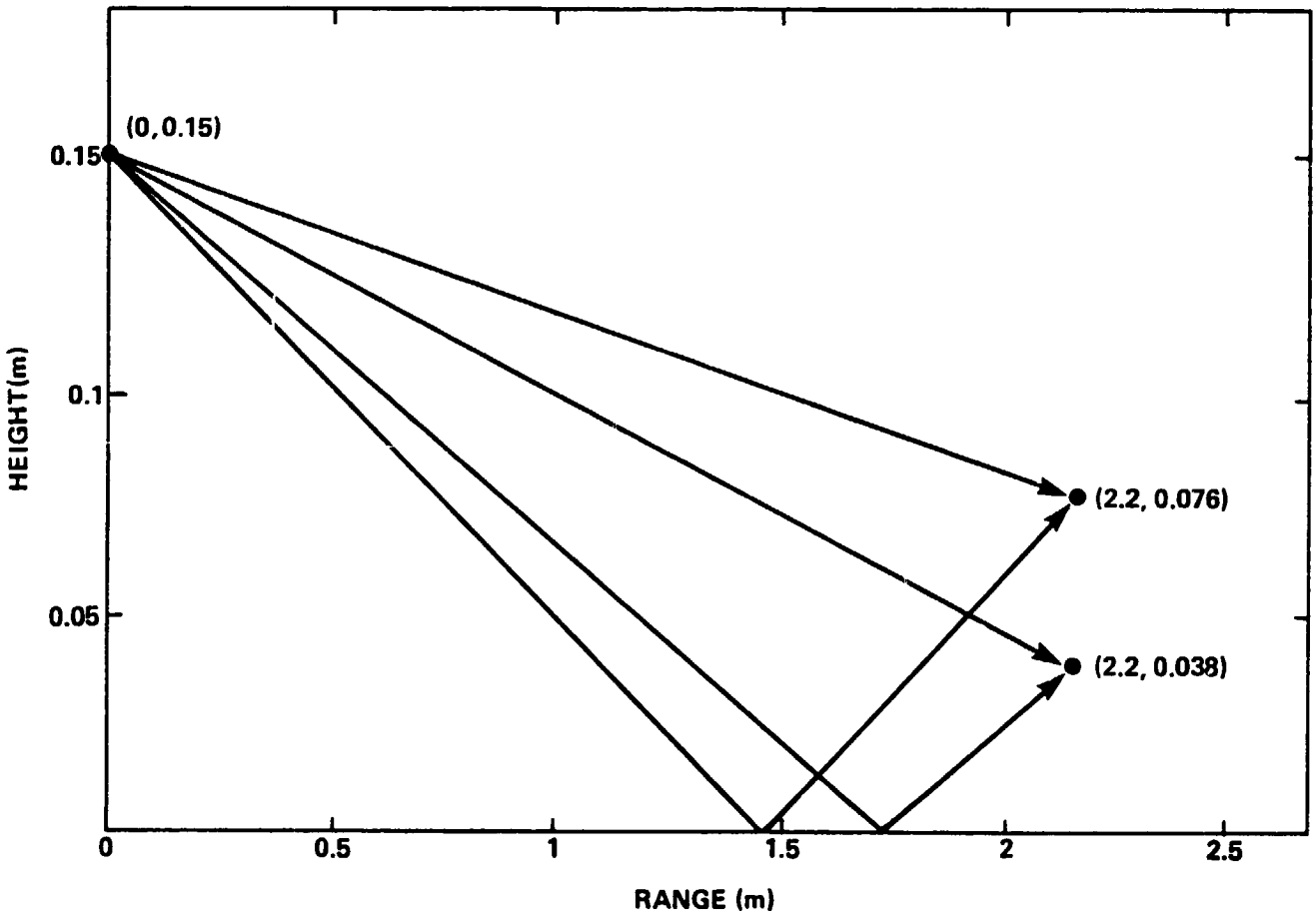

FIGURE 22. GEOMETRIES FOR PROPAGATION OVER FLAT, SOFT GROUND.

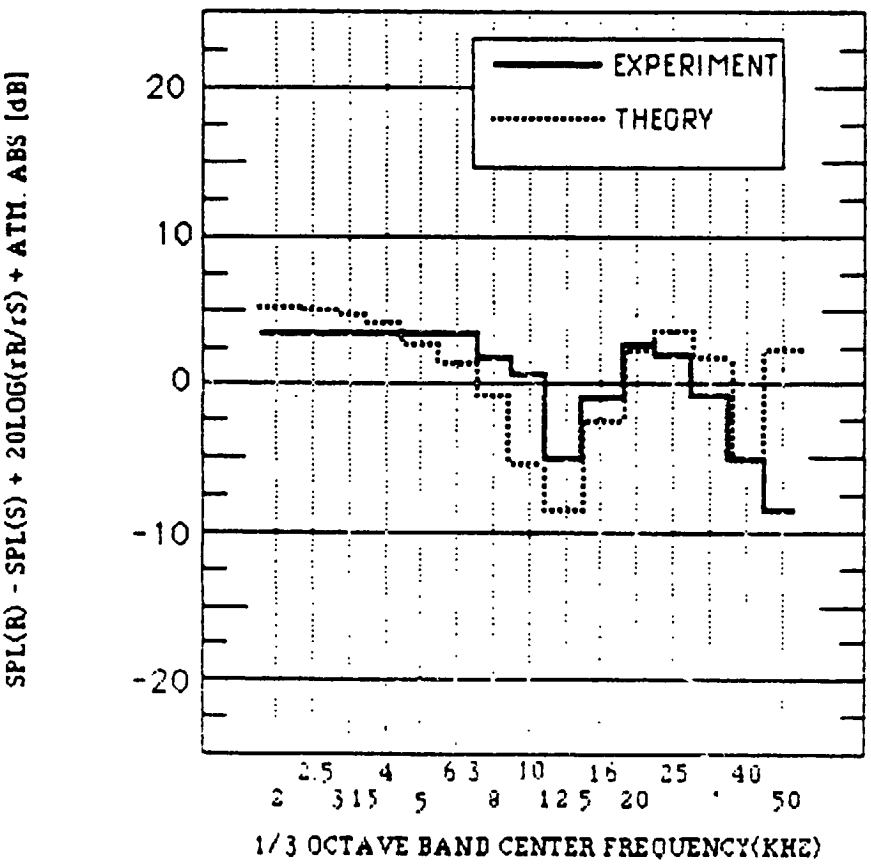

FIGURE 23. PROPAGATION OVER SOFT, FLAT GROUND WITH NO WIND. (SOURCE HEIGHT .15 m, RECEIVER HEIGHT .076 m, DISTANCE 2.2 m.)

- Direct-wave pressure: 1 (since IL is normalized to this free-field pressure)
- Reflected-wave pressure: $0.572 \exp[i2\pi(0.507)]$
- Ground/surface-wave pressure: $0.0762 \exp[i2\pi(0.195)]$.

These pressure details point out that the reflected wave is significantly reduced in magnitude compared to the direct wave, and very nearly out of phase with it. As distinct from the hard-ground case, the moderate amount of destructive interference here is due to the reduced amplitude of this reflected wave. Of this 0.507 phase shift, 0.124 is due to phase shift upon reflection - a significant fraction of the total, as distinct from the hard-ground case. The remainder of the phase shift is due to the path-length difference between direct and reflected rays.

In the 25 kHz band, the analysis predicts partially constructive interference between direct and reflected waves. This interference also occurs in the experimental results, though with a slight frequency shift downward.

In the 40-kHz band, the analysis again predicts destructive interference, though not as complete as before. This interference is also evident in the experimental data. At 40 kHz exactly, the analysis yields the following contributions:

- Direct-wave pressure: 1
- Reflected-wave pressure: $0.447 \exp[i2\pi(0.495)]$
- Ground/surface-wave pressure: $0.0188 \exp[i2\pi(0.321)]$.

Of the 0.495 phase shift of the reflected wave, 0.272 is due to phase shift upon reflection. As is apparent, the ground-surface term is negligible.

Source height 0.15 m; receptor height 0.038 m

Figure 24 contains the results of the comparison for the 0.15-m source and 0.038-m receptor.

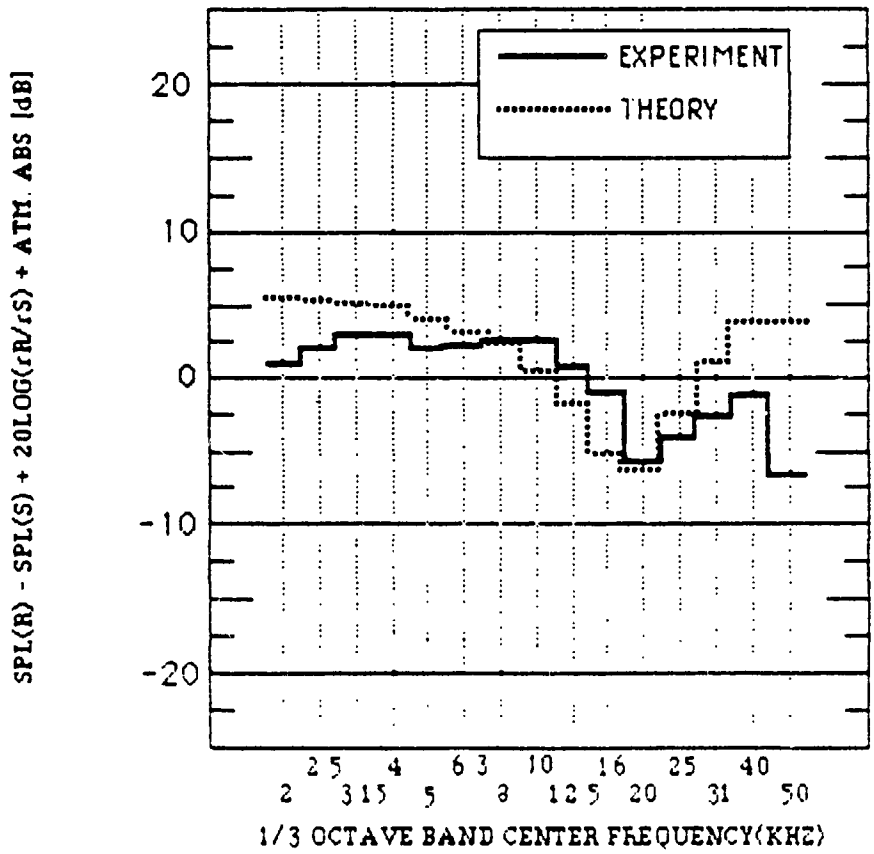

FIGURE 24. PROPAGATION OVER SOFT, FLAT GROUND WITH NO WIND. (SOURCE HEIGHT .15 m, RECEIVER HEIGHT .038 m, DISTANCE 2.2 m.)

At low frequencies, the analysis predicts a 6-dB pressure doubling, which is again mostly missing from the experimental results. In the 20-kHz band, the analysis predicts a moderate minimum, due to partially destructive interference between direct and reflected rays. This predicted interference is evident in the experimental data. At 20 kHz exactly, the analysis yields the following pressure contributions:

- Direct-wave pressure: 1
- Reflected-wave pressure: $0.471 \exp[i2\pi(0.515)]$
- Ground/surface-wave pressure: $0.0650 \exp[i2\pi(0.279)]$.

Of the phase 0.515 shift of the reflected wave, 0.209 is due to phase shift upon reflection. As is apparent, the ground/surface term is essentially negligible.

In the 40-kHz band, the analysis predicts partially constructive interference between direct and reflected waves. This interference occurs in the experimental results, though to a lesser degree.

General discussion of soft-ground results

With soft ground, agreement between experiment and analysis is very good except at very low frequencies. In general, the soft-ground measurements yielded destructive interference where predicted, with approximately the correct magnitudes. There are a number of reasons why we should expect the soft ground data to compare better with theory than do the hard ground data. First, the expected destructive interference is not as great with soft ground, and therefore system noise is not as important. Second, the aluminum plate is not only effectively damped by the model grass, but also the model grass reduces the amount of energy that can enter the plate and be subsequently radiated.

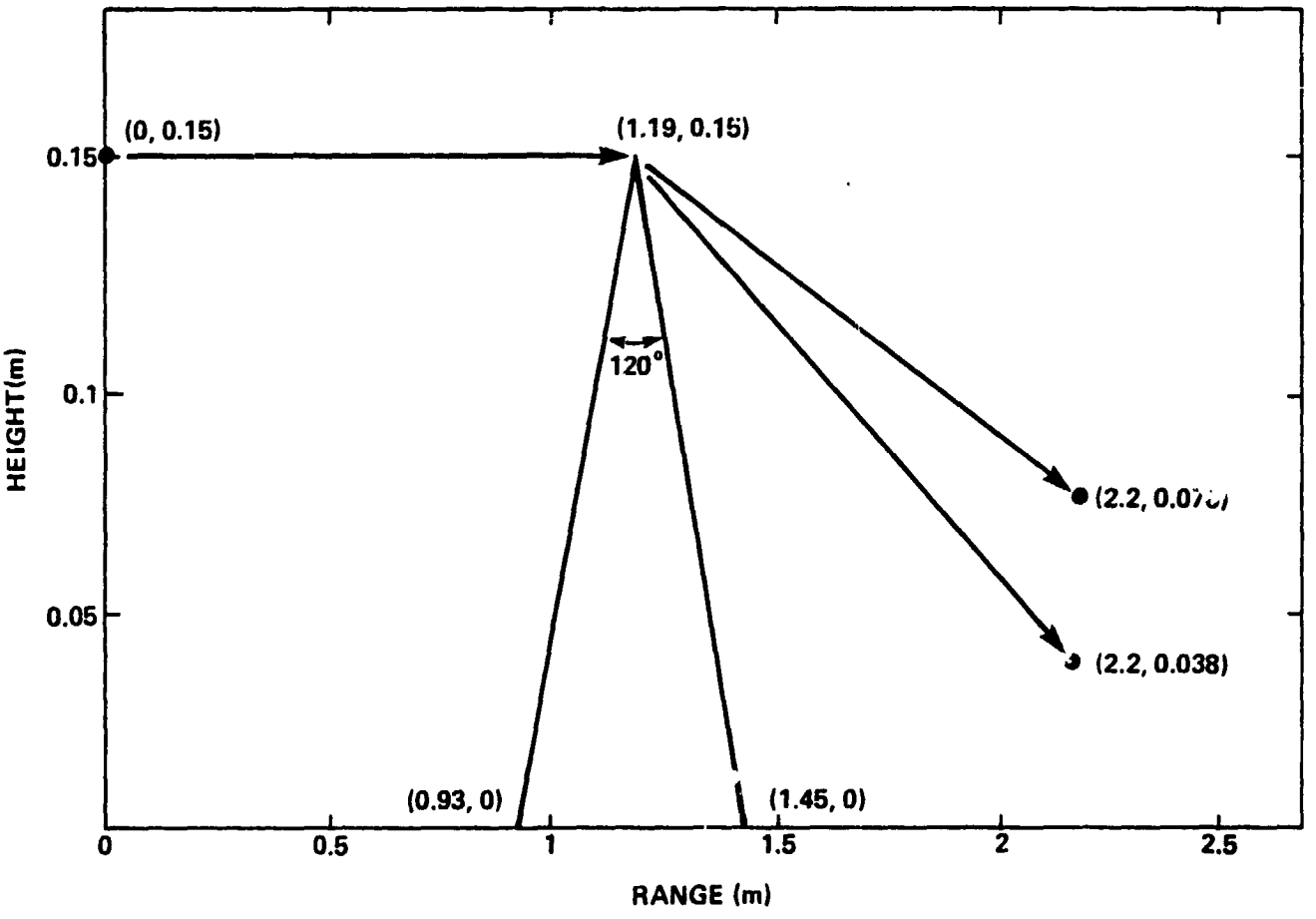

FIGURE 25. COMPARISON OF DATA WITH THEORY: CASE 6.

6.1.3 Propagation over a soft-ground hill

The selected geometries for propagation over a hill appear in Fig. 25. Note that the vertical scale is stretched 10-to-1, relative to the horizontal scale. The source-receptor distance for all selected geometries is again 2 2 m. Two pairs of source/receptor heights were selected:

0.15 m/0.076 m

0.15 m/0.038 m.

For these geometries, App. C was used to calculate the IL of the hill, assuming the full-scale ground impedance in Fig. 10, scaled upwards in frequency by a factor of 100. Although this full-scale impedance does not correspond exactly to the impedance in the scale model (which also appears in Fig. 10) results are very insensitive to ground impedance.

In each use of App. C, four solutions were obtained:

- Kurze: hard, thin-screen
- Pierce: hard-wedge
- Pierce: hard, thin-screen (same as hard wedge but interior wedge angle reduced to zero)
- Pierce: absorptive wedge.

The Kurze equations apply only to thin screens, and predict a barrier IL of 5 dB when the line-of-sight between source and receptor just grazes the barrier top. Theoretically, this value should be 6 dB, since the entire bottom half of the wavefront is truncated in this geometry.

For this same grazing geometry, the Pierce hard-wedge equations predict an IL of 0 dB. For receptors outside the geometrical shadow of the barrier, these Pierce equations predict amplification. Obviously, Pierce's equations are not valid in the vicinity of the grazing line-of-sight.

As a compromise, the maximum of either Kurze or Pierce was used. Thereby, for a geometry with the receptor inside the geometric shadow, 5 or 6 dB IL (Kurze) was obtained at the lowest frequencies, increasing slowly with increasing frequency, until the Kurze solution equaled the Pierce solution. Invariably, the Pierce IL exceeded the Kurze IL above this transition frequency, and, therefore, Pierce was used for higher frequencies.

The Pierce thin-screen solution predicted 2-3 dB higher ILs than Kurze, at the highest frequencies. Comparison of Pierce thin-screen with Pierce hard-wedge indicated a reduction in IL due to the thickness of the wedge: 1-2 dB for these cases, independent of frequency. Comparison of the Pierce hard-wedge with the Pierce absorptive-wedge indicated the additional IL due to the absorptive ground: 0-1 dB for these cases.

For the wedge calculations, two (p, q) (see App. C for the definition of p and q) pairs were used to bracket the wedge angle, which is 4.189 radians. These (p, q) pairs are:

- (31, 12), yielding an angle of 4.058 radians
- (33, 12), yielding an angle of 4.320 radians.

The wedge solutions were essentially identical for both bracketing runs, in all cases.

Resulting ILs appear in Table 1.

Source height 0.15 m; receptor height 0.076 m

Figure 26 contains the comparison of experimental results with the analysis for the 0.15-m source and 0.076-m receptor.

The match between analysis and experiment is quite good over the entire frequency range. The destructive interference in the 4 to 8 kHz range indicated in the experimental data results most likely from ray paths that reflect from the horizontal ground surface of the tunnel. These paths are not considered in the simple analytical model and, consequently, we do not expect to predict this type of interference.

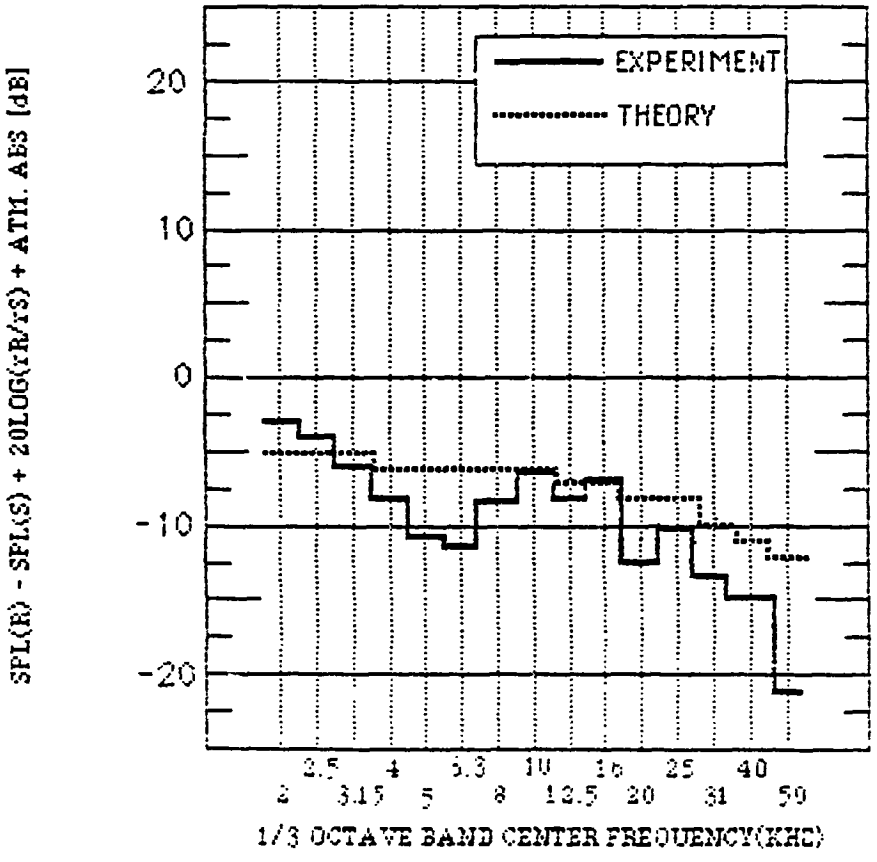

FIGURE 26. PROPAGATION OVER SOFT GROUND WITH .15 m HILL AND NO WIND. (SOURCE HEIGHT .15 m, RECEPTOR HEIGHT .076 m, DISTANCE 2.2 m.)

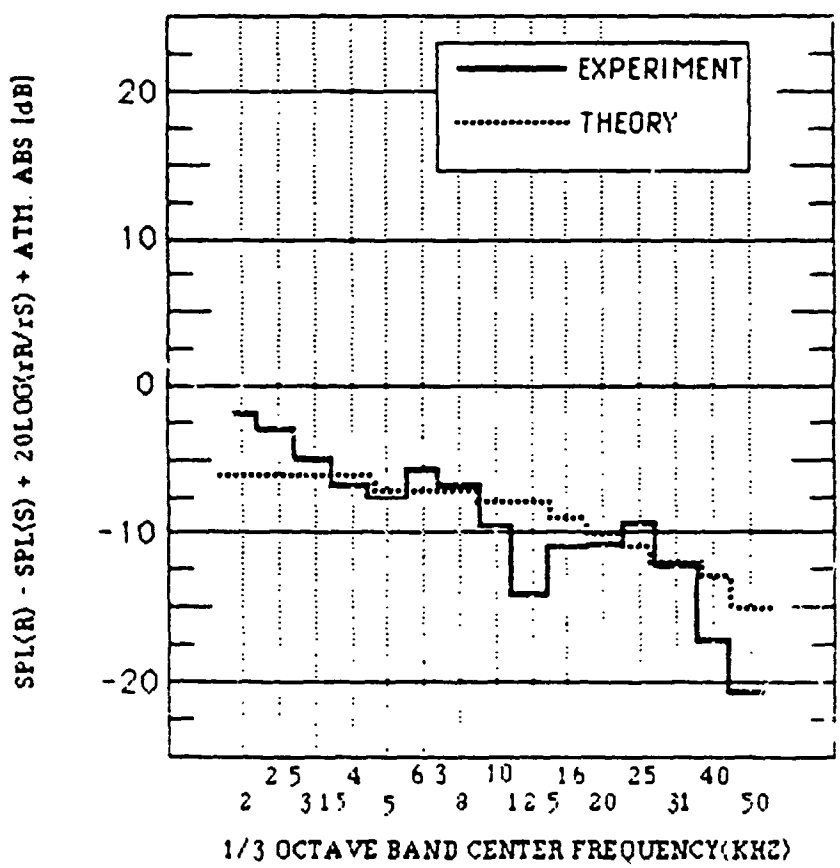

FIGURE 27. PROPAGATION OVER SOFT GROUND WITH .15 m HILL AND NO WIND. (SOURCE HEIGHT .15 m, RECEPTOR HEIGHT .038 m, DISTANCE 2.2 m.)

Source height 0.15 m; receptor height 0.038 m

Figure 27 contains the comparison of experimental results with the analysis for the 0.15-m source and 0.038-m receptor.

The match between analysis and experiment is quite good. Again, the experimental results indicate destructive interference that is not predicted by the simple analytical model. The cause is no doubt the same deficiency in the mathematical model as pointed out previously, i.e., lack of ground plane. As expected, the attenuation very close to the ground (0.038 m receiver height) is greater than for the previous 0.076 m receiver height presented in Fig. 26.

General discussion of soft-ground with hill results

The Pierce model was chosen for analysis because it alone allowed computation of the effect of absorptive ground. However, this model does have some deficiencies when applied to the propagation over a soft-ground hill.

Pierce's diffraction equations do not predict the interference that appears in the experimental data. For the hill-on-a-horizontal-plane geometry that was used in this study, such interference could arise due to paths that reflect from the horizontal portion of the terrain. Pierce's infinit wedge geometry does not allow incorporation of these addit al paths, (retaining phase) and consequently the interference is not expected.

In summary, the soft-hill data, without wind, indicate that:

- Comparison between theory and experiment are quite good
- Future analysis should incorporate the effects of rays reflected from the horizontal ground surfaces.

6.2 Sound Propagation With Wind

6.2.1 Creation of soft-ground shadow upwind (Effect 2)

Where a soft-ground shadow did not exist because the ground was too remote, upward refraction can, in effect, bring the ground closer and thereby create a soft-ground shadow.

For this test, the selected source-receptor geometry appears in Fig. 28. Note that the vertical scale is stretched 10-to-1, relative to the horizontal scale. The source-receptor distance is 2.2 m. This geometry would tend to produce a soft-ground shadow because the refraction reduces both (a) the grazing angle of incidence with the ground, and (b) the path length difference between direct and reflected rays -- both relative to the no-wind situation.

For this geometry, the flat-terrain wind data of App. F was used to search for both the direct ray and the reflected path from the ground. No reflected path was found, however. For this source-receptor geometry and wind condition, the receptor is in the upwind refraction shadow (Effect 1). The computed grazing ray appears in Fig. 29. Therefore, these experimental data test not for Effect 2, but for a soft-ground version of Effect 1.

However, there do exist two direct rays from source to receptor, shown in Fig. 29. One is high above the ground, while the other is refracted strongly near the ground.

Note that this second direct ray does not undergo any phase shift near the ground. However, it does have a phase shift relative to the higher direct ray due to path-length difference. Therefore, the two combine coherently at the receptor and produce interference. The resulting levels, relative to the direct ray alone, appear in Table 2 and in Fig. 30, where they are compared to experimental results.

At the lower frequencies, the analysis predicts 5-6 dB of pressure doubling, which is partly missing from the experimental

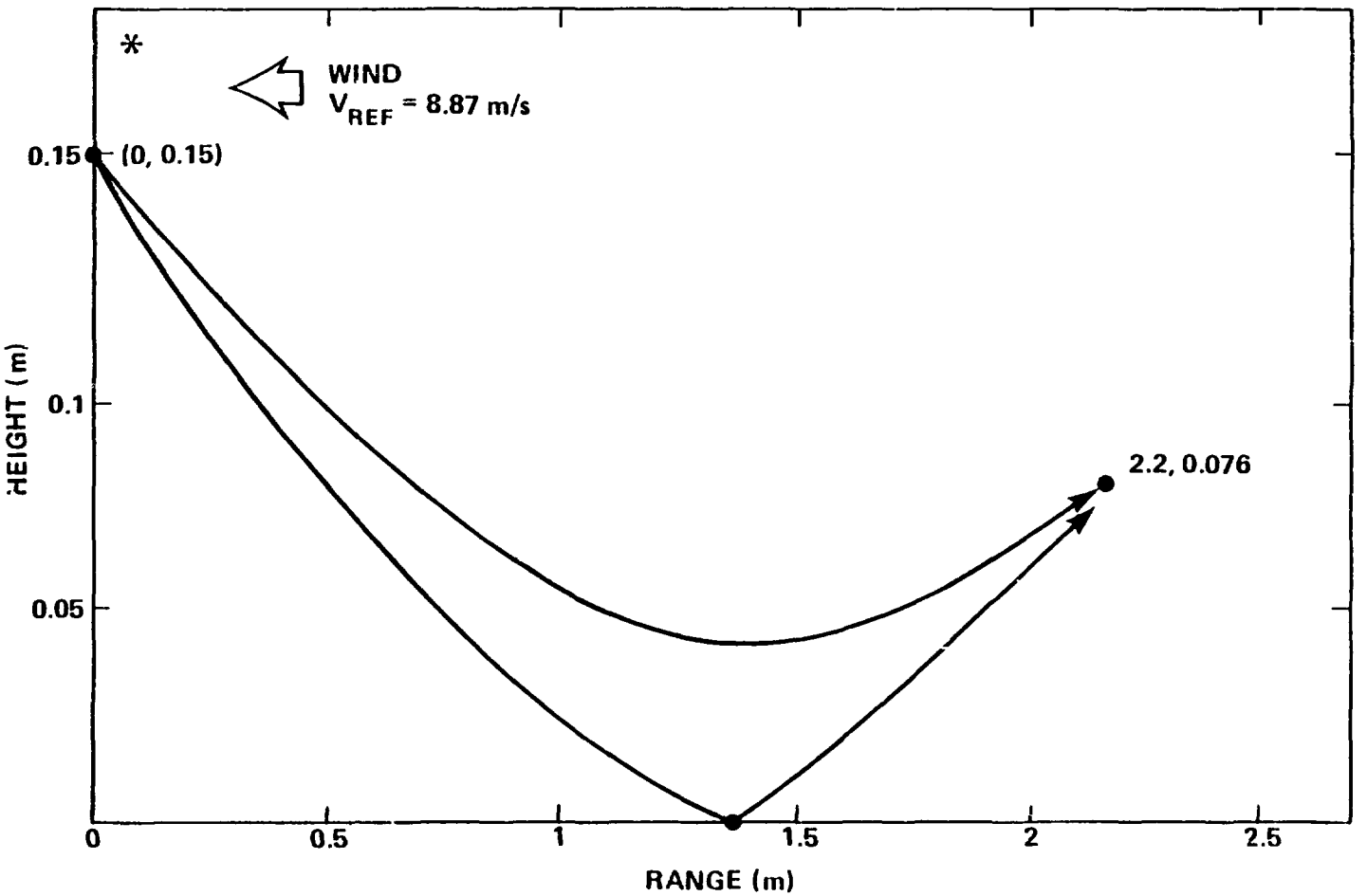

FIGURE 28. GEOMETRY FOR PROPAGATION OVER SOFT GROUND WITH WIND (EFFECT 2).

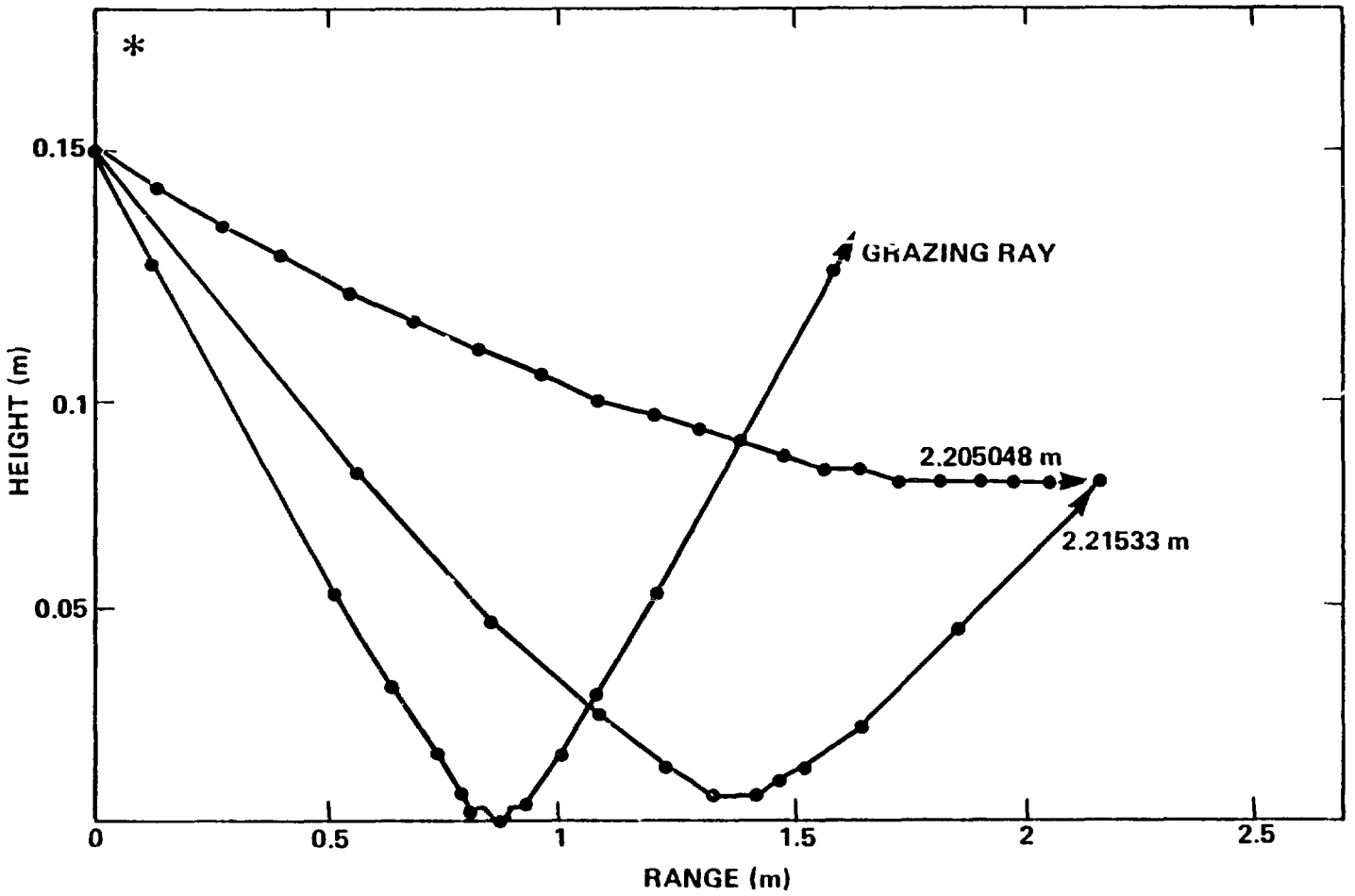

FIGURE 29. COMPUTED RAYS FOR PROPAGATION OVER SOFT GROUND WITH WIND.

TABLE 2

ANALYSIS RESULTS: WITH WIND

Effect	Effect 2		Effect 3		Effect 4	
Reference Wind Speed (m/s)	8.8	0	2.5	0	8.8	0
Terrain	Soft Flat	Soft Flat	Hard Hill	Hard Hill	Hard Hill	Hard Hill
Source Height (m)	0.15	0.15	0.013	0.013	0.15	0.15
Receptor Height (m)	0.076	0.076	0.15	0.15	0.15	0.15
1/3-Octave Band Insertion Loss (dB)	-5.9	-5.4	5	6	5	5
	-5.8	-5.2	5	6	5	5
	-5.6	-4.7	5	6	5	5
	-5.4	-4.1	6	6	5	5
	-5.1	-3.1	6	7	5	5
	-4.5	-1.5	6	7	5	5
	-3.5	1.2	6	8	6	5
	-1.8	5.7	6	8	6	5
	0.6	8.7	7	9	6	5
	10.1	1.9	7	10	6	5
	5.5	-2.0	7	11	6	5
	-2.2	-3.5	8	12	7	5
	-5.6	-1.8	9	13	7	5
	-4.8	5.4	10	14	7	5
	3.4	-2.2	11	15	8	5

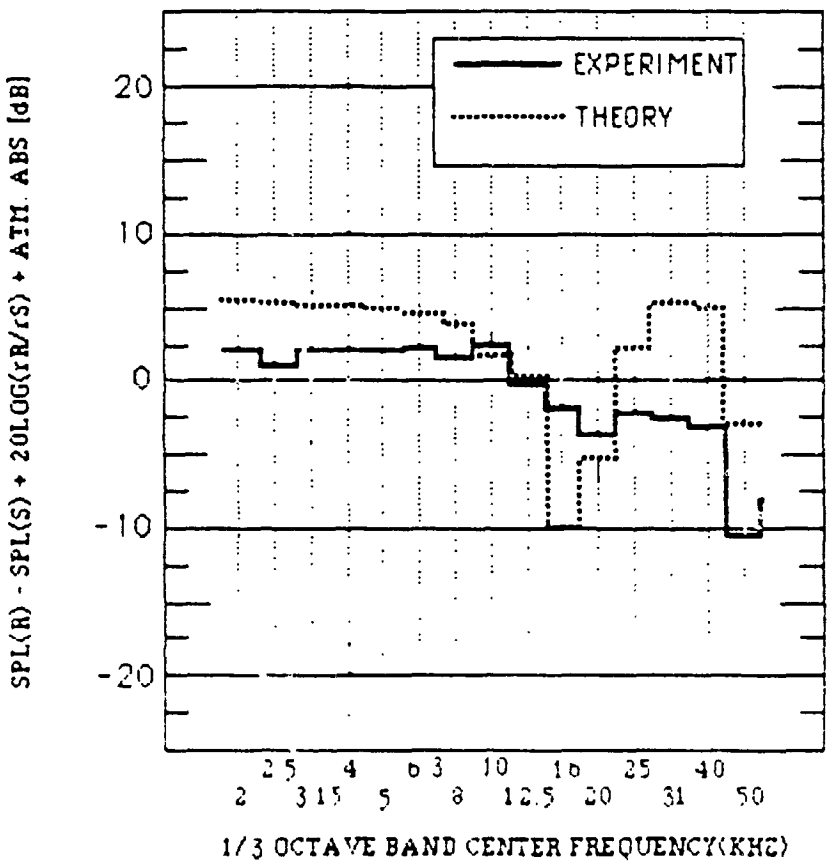

FIGURE 30. PROPAGATION UPWIND OVER SOFT, FLAT GROUND. (SOURCE HEIGHT .15 m, RECEPTOR HEIGHT .076 m, DISTANCE 2.2 m, WIND SPEED 8.8 m/s.)

results. In the 16 kHz band, and somewhat less in the 20 kHz band, the analysis predicts destructive interference. Some interference appears in the experimental results. Around 31-40 kHz, the analysis predicts constructive interference, which is not present in the experimental results. In the 50 kHz band, the analysis again predicts destructive interference, which does appear experimentally. The no-wind reference case appeared previously in Fig. 23.

Discussion of results

At the lower frequencies, the 5-6 dB pressure doubling is missing from the experimental data. Suspected again is a gain misadjustment. Compared to the no-wind situation, interference at moderate and high frequencies tends to be "washed out." This is probably due to wind turbulence, which tends to destroy coherence between the interfering rays. In spite of this, however, levels are not significantly changed by the wind, although the energy is shifted somewhat in frequency.

6.2.2 Elimination of hard-ground diffraction shadow downwind (Effect 3)

A diffraction shadow behind intervening terrain may be flanked by refraction, if the wind velocity gradients are strong enough. For this test, the selected source-receptor geometry appears in Fig. 31. Note that the vertical scale is stretched 10-to-1, relative to the horizontal scale. The source-receptor distance is 2.2 m.

For this geometry, the 0.15 m hill wind data of App. F was used to search for the flanking ray -- that is, the ray that refracts over the hilltop, directly from source to receptor. No such ray was found since the wind velocity gradients are not sufficiently strong to produce complete flanking for this source/hill/receptor geometry.

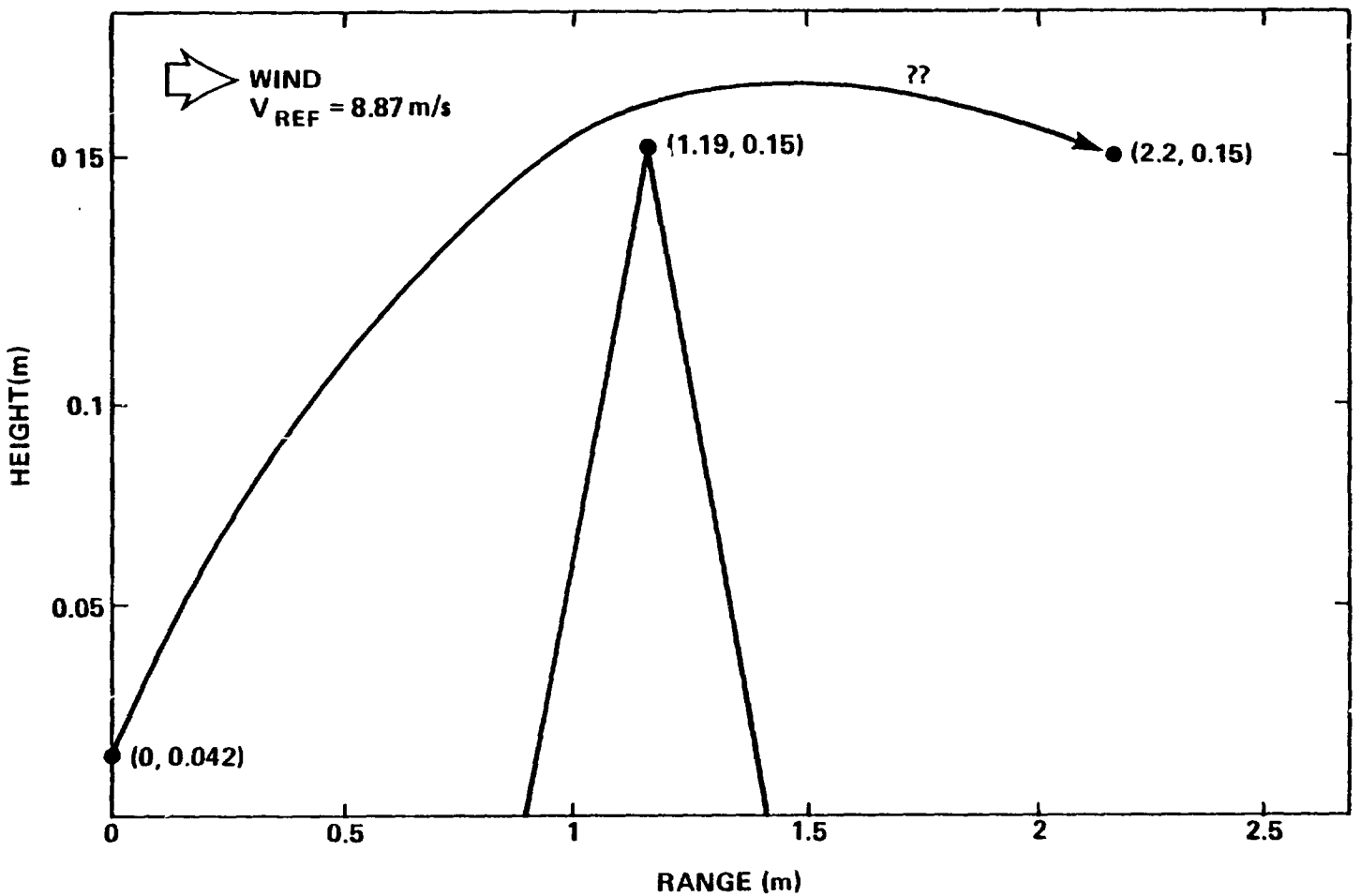

FIGURE 31. GEOMETRY FOR ELIMINATION OF HARD GROUND DIFFRACTION SHADOW DOWNWIND.

Therefore, we searched for two alternative rays: the first between the source and the hilltop; the second between the hilltop and the receptor. It proved impossible to find such a ray pair. Extreme refraction near the hilltop prevented any ray from reaching this topmost point. An increase in initial ray angle (at the source) from 9.761631 degrees to 9.761632 degrees -- an increase of only 0.000001 degrees -- produced a discontinuity in ray height, at the hilltop's range, from 0.01 m to 0.017 m. Figure 32 shows this discontinuity. In effect, the extreme wind-velocity gradients at the hilltop produced an effective singularity there.

As a compromise, the following two rays were sought: the first between the source and the hilltop-plus-0.017 m; the second between this same point and the receptor. These two paths appear in Fig. 33.

Although in the figure these paths appear smoothly connected at the hilltop, their slopes actually differ. The source ray approaches the hilltop at an angle of 4.4 degrees down from the horizontal, while the receptor ray emerges at an angle of 0.3 degrees upward from the horizontal. The angular difference of 4.1 degrees is the effective angle of diffraction over the hilltop.

For comparison, the angle of diffraction without wind is 6.7 degrees. As expected, the wind has reduced the angle of diffraction.

Figure 33 also shows the transformed source and receptor points -- transformed to preserve diffraction angles at the hilltop and also to preserve the source-hilltop and the hilltop-receptor distances. With these transformed points, App. C was used to calculate the IL due to diffraction. Three solutions were obtained:

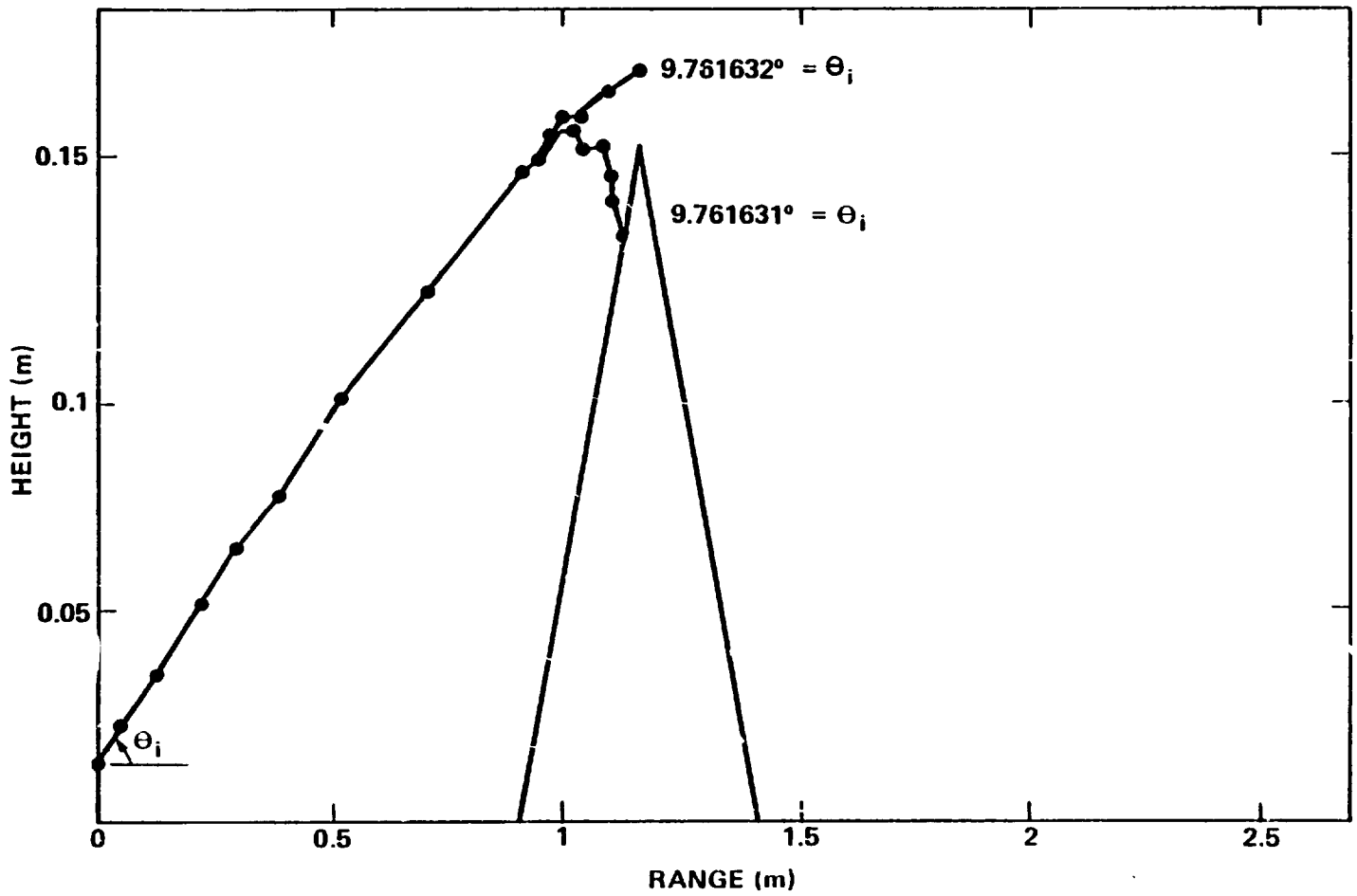

FIGURE 32. DISCONTINUITY IN COMPUTED RAYS FOR DOWNWIND PROPAGATION OVER A HILL.

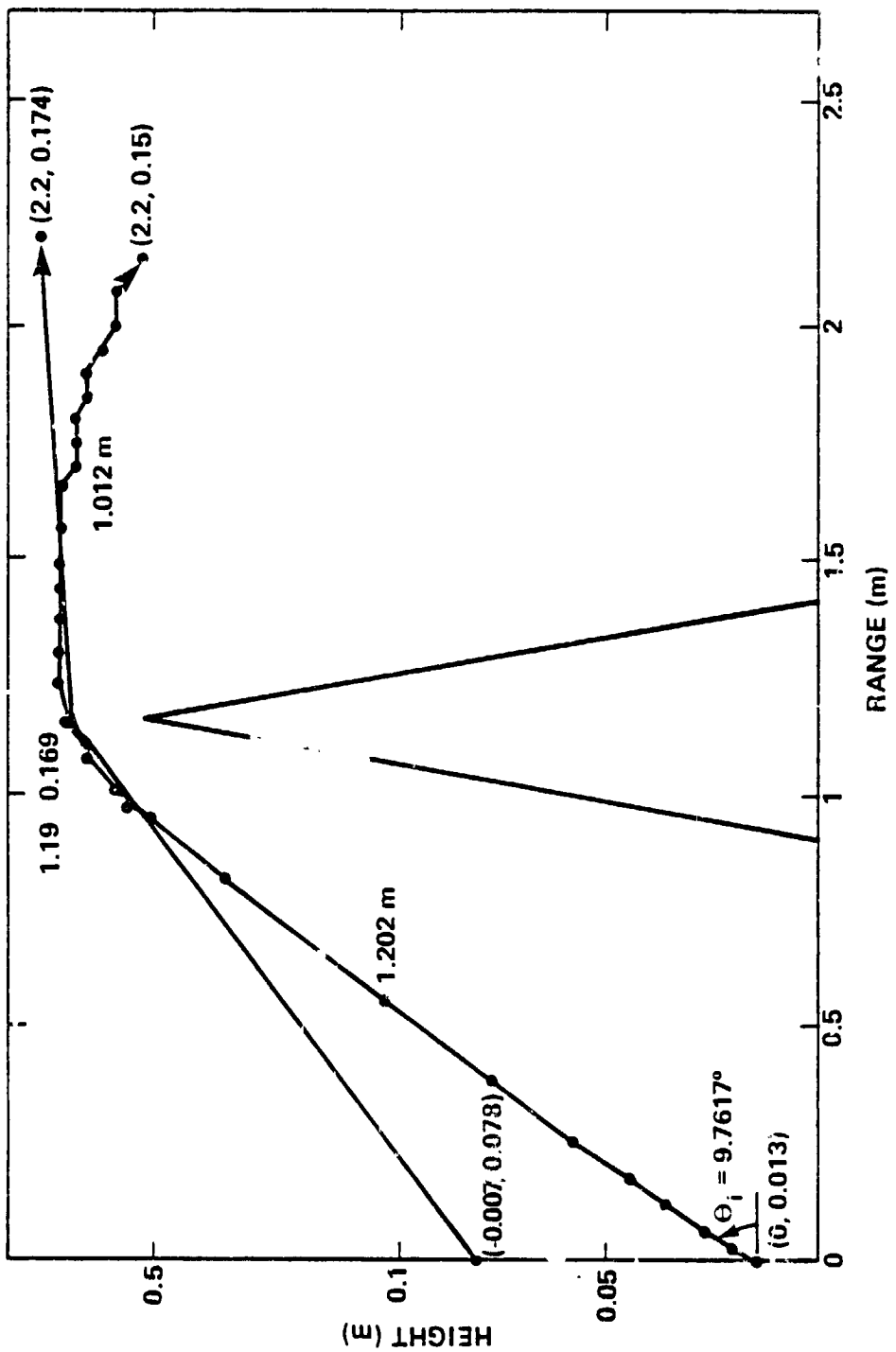

FIGURE 33. COMPUTED RAYS SELECTED FOR ANALYSIS OF DOWNWIND PROPAGATION OVER A HILL.

- Kurze
- Pierce: hard, thin-screen
- Pierce: hard-wedge.

As was done for the no-wind diffraction case above, the maximum of either the Kurze or Pierce solutions was used, because the Pierce solutions are not valid for low frequencies.

The Pierce thin-screen solution predicted 1-3 dB higher ILs than did Kurze, at the highest frequencies. Comparison of Pierce thin-screen with Pierce hard-wedge calculations indicated a reduction in IL due to the thickness of the wedge: 1 dB for these cases, independent of frequency.

For wedge calculations, a (p, q) pair of (33, 12) was used to approximate the wedge angle, yielding an angle of 4.3197 radians.

Resulting ILs appear in Table 2 and in Fig. 34a, where they are compared to experimental results.

At the lower frequencies, the analysis predicts 5-6 dB of barrier attenuation, which is mostly missing from the experimental results. At the upper frequencies, the match between analysis and experiment is good, except that the experimental results include interference not present in the analytical model. This interference is again probably due to rays reflecting from the horizontal ground surface not considered in the analytical model.

Mathematical models exist for computing barrier IL over an absorptive horizontal surface [16]. However, these models consider only thin-screen barriers, not wedges, and would not be applicable here. Our actual ground surface consisted of two parts: (1) the wedge's surface, tilted to the horizontal and (2) the horizontal ground, upon which the wedge sat. Required, therefore, is a theory that takes both of these absorptive

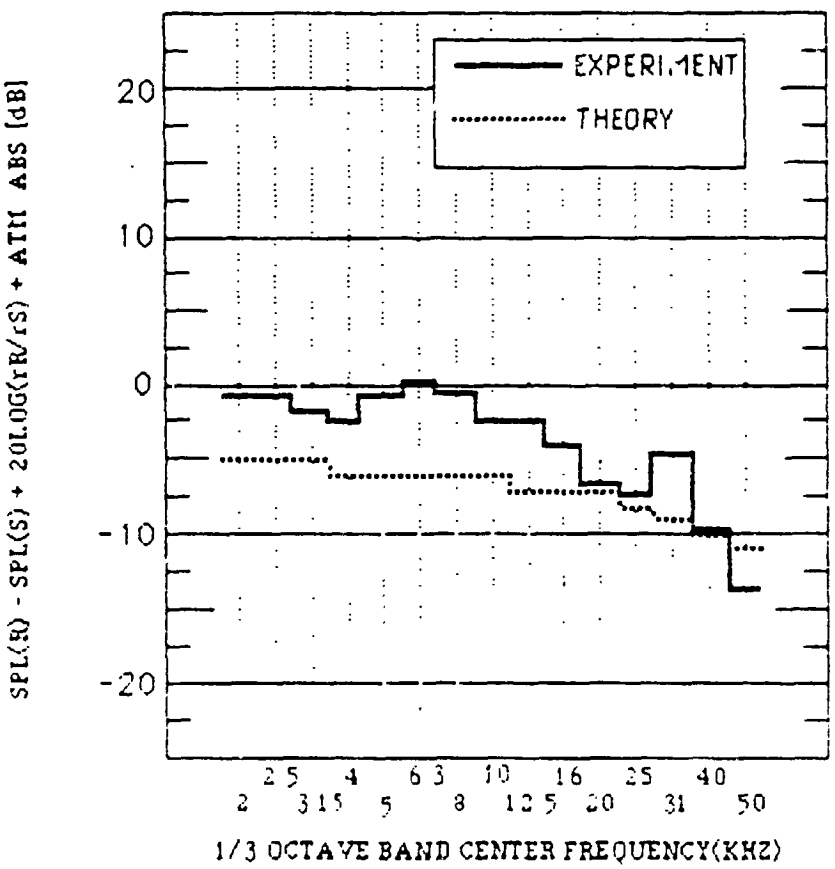

a. WIND SPEED 2.5 m/s.

FIGURE 34a. PROPAGATION DOWNWIND OVER A HILL (EFFECT 3). (SOURCE HEIGHT .013 m, RECEPTOR HEIGHT .15 m, DISTANCE 2.2 m, HILL HEIGHT .15 m.)

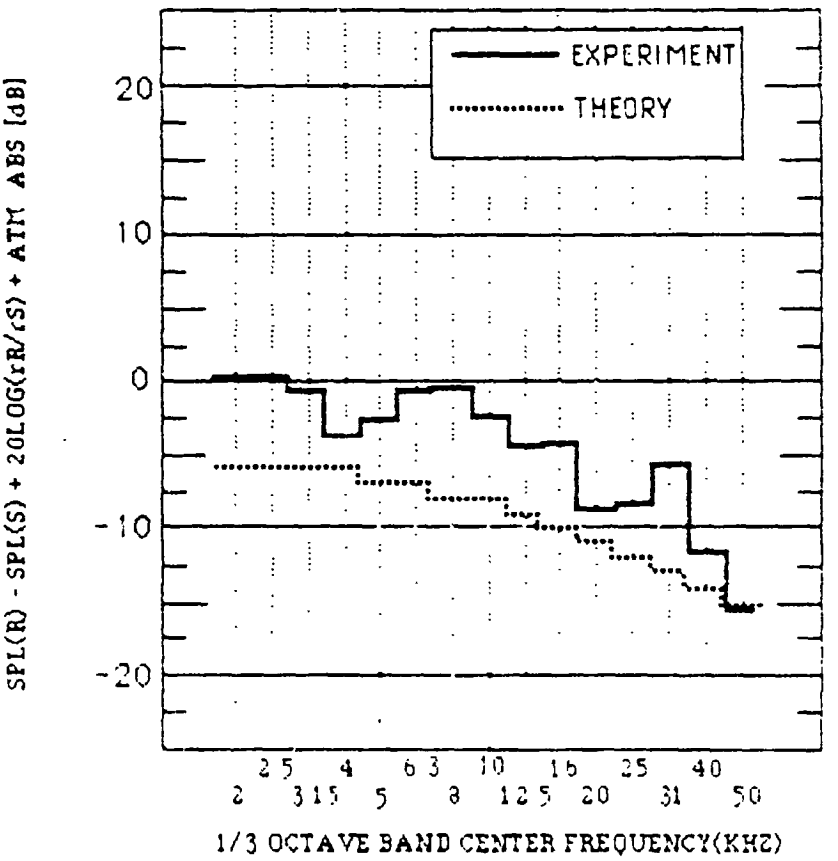

b. No Wind.

FIGURE 34b. PROPAGATION DOWNWIND OVER A HILL (EFFECT 3). (SOURCE HEIGHT .013 m, RECEPTOR HEIGHT .15 m, DISTANCE 2.2 m, HILL HEIGHT .15 m.)

surfaces into account. Such a theory does not presently exist.

The no-wind condition provides a baseline for these with-wind calculations. For the no-wind case, App. C was again used to compute the IL of the hill, this time with untransformed source and receptor positions. The analysis predicts a decrease in IL due to wind, ranging from 1 to 4 dB.

The analysis results for the no-wind case appear in Fig. 34b, where they are compared to experimental no-wind results.

At the lower frequencies, the analysis predicts a 6-7 dB IL, which is mostly missing from the experimental results. At the upper frequencies, again the analysis predicts greater IL than was experimentally found. In addition, the experimental results include apparent interference not included in the mathematical model.

Part of the difficulty may be that, near the top of the hill, nearly adjacent rays diverge dramatically. Changes in level due to this ray-tube divergence are ignored in this study.

Another reason for non-perfect match between experiment and analysis is that the wind data were interpolated horizontally, thereby providing a rough approximation of the actual wind behavior downwind of the hill.

Discussion of results

The loss of 5-dB barrier attenuation at the low frequencies both with and without wind is evident in Fig. 34. For the geometry used the line-of-sight between source and receptor is certainly blocked by the hill. Note that this loss did properly occur in Figs. 26 and 27.

The difference between this case and that of Figs. 26 and 27 is that in the present case the source is very near to the ground and, consequently, pressure doubling would be expected at least in the lower frequency bands. The mathematical model used here

does not include the ground plane and, consequently, this doubling is not present in the analysis. Note that the agreement between theory and experiment would be quite good if the theoretical curve was incremented by 6 dB. We suspect that the 5-6 dB attenuation, due to the barrier, is offset by pressure doubling at the lower frequencies. The interference in some bands again indicates that the ground plane must be included in the theoretical analysis.

The wind analysis shows an increase in level of 3-4 dB at upper frequencies compared to the no-wind case. The corresponding data comparison shows an increase of only 1-2 dB. The trends are the same, although the analysis overpredicts the wind-induced increase.

6.2.3 Elimination of diffraction shadow upwind (Effect 4)

A diffraction shadow behind intervening terrain may be flanked upwind, because of the strong anomalous wind gradients near the terrain peak. Such anomalous wind gradients can produce a strong downward refraction. If this downward refraction is strong enough to overbalance the upward refraction along the rest of the sound path, then this flanking will occur.

Figure 35 shows the geometry for this case. Chosen was a geometry with maximum wind gradients and minimum (5 dB) diffraction shadow, where the receptor is on the grazing line-of-sight across the hilltop. Note that the vertical scale is stretched 10-to-1, relative to the horizontal scale in the figure. The source-receptor distance is 2.2 m.

For this geometry, the 0.15-m hill wind data of App. F was used to search for the flanking ray -- that is, one that refracts over the hilltop, directly from the source to receptor. No such ray was found; the wind velocity gradients are not sufficiently strong to produce complete flanking for this source/hill/receptor geometry.

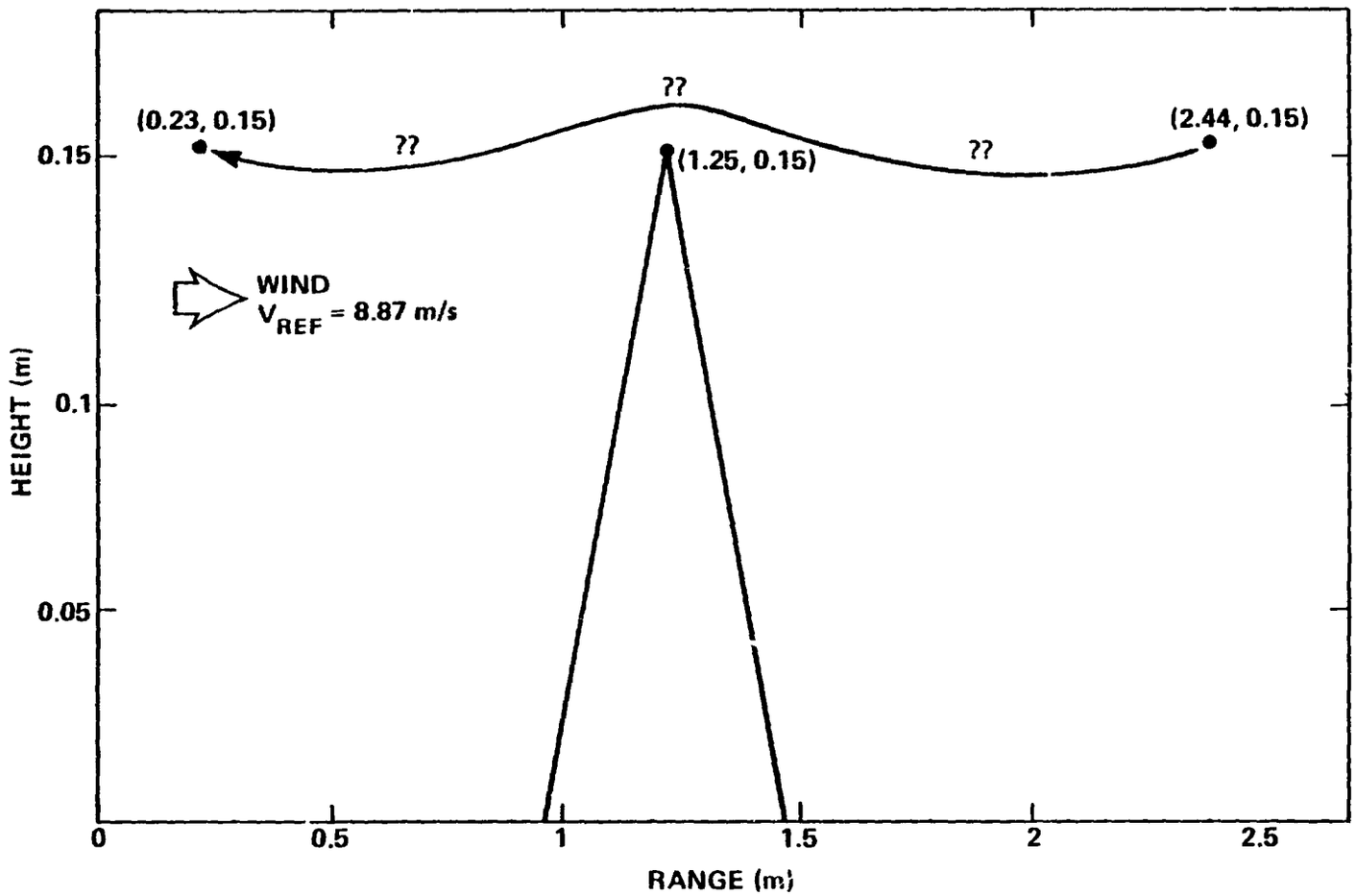

FIGURE 35. GEOMETRY FOR UPWIND PROPAGATION OVER A HILL.

Therefore, we searched for two alternative rays: the first between the source and the hilltop; the second between the hilltop and the receptor. It proved impossible to find such a ray pair because extreme refraction near the hilltop prevented any ray from reaching this topmost point. The closest ray that could be found came within 0.015 m of the hilltop. Therefore, as a compromise, the following two rays were sought: the first between the source and the hilltop-plus-0.015 m; the second between this same point and the receptor. These two paths appear in Fig. 36.

The slopes of the source ray and the receptor ray differ at the hilltop. The source ray approaches the hilltop at an angle of 2.00 degrees down from the horizontal, while the receptor ray emerges at an angle of 0.80 degrees, also downward. The angular difference of 2.80 degrees is the effective angle of diffraction over the hilltop. Note that this angle is zero for the no-wind situation. Therefore, the wind <u>increases</u> the diffraction shadow.

Figure 36 also shows the transformed source and receptor points -- transformed to preserve diffraction angles at the hilltop and also to preserve the source-hilltop and hilltop-receptor distances. With these transformed points, App. C was used to calculate the IL due to diffraction. Three solutions were obtained:

- Kurze
- Pierce: hard, thin-screen
- Pierce: hard-wedge.

As was done in previous example the maximum of either the Kurze or Pierce calculations was used.

The Pierce thin-screen solution predicted 0-2 dB higher IL than did the Kurze solution, at the highest frequencies. Comparison of Pierce thin-screen with Pierce hard-wedge solutions indicated a reduction in IL due to the thickness of the wedge: 1 dB for these cases, independent of frequency.

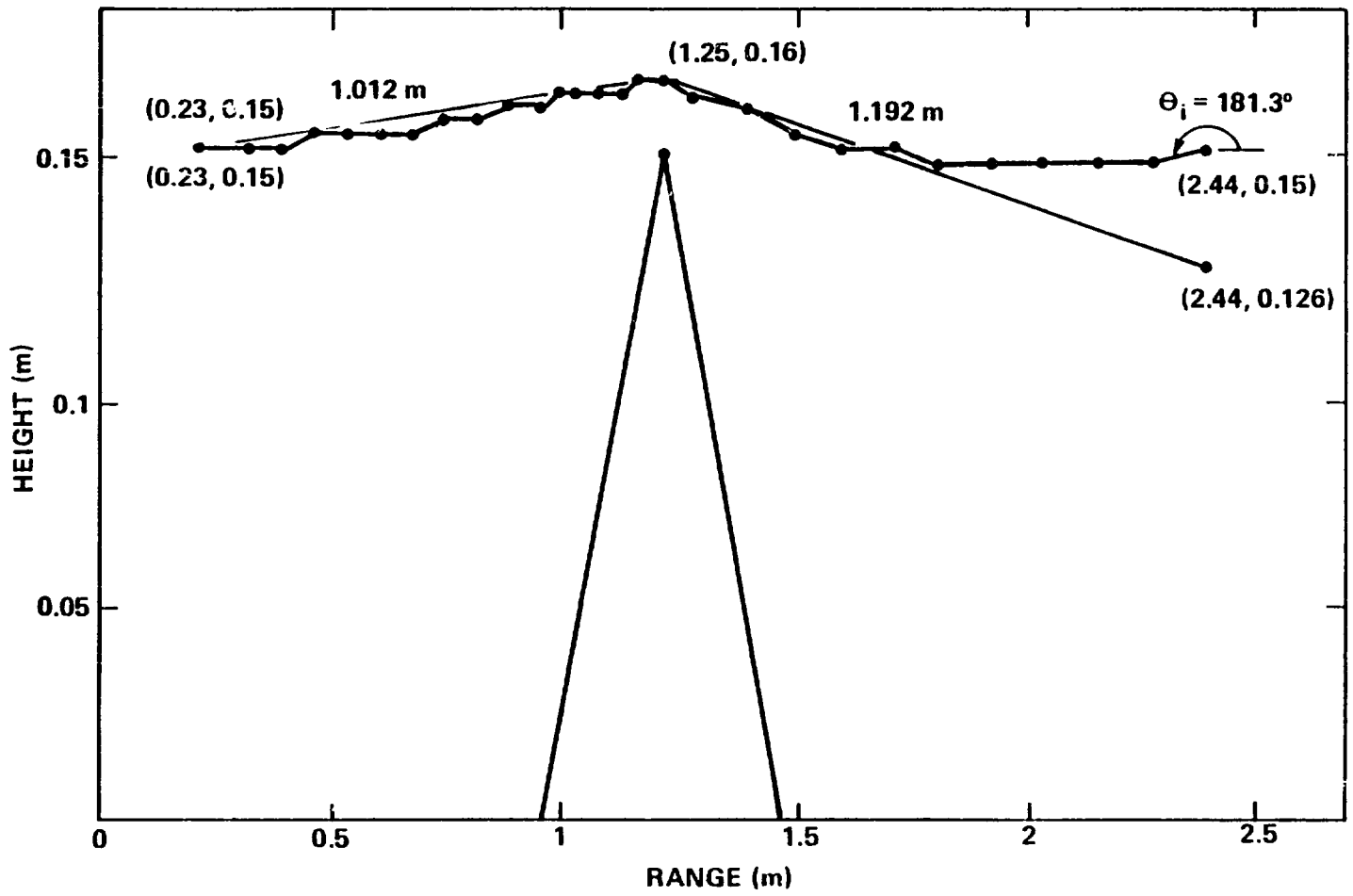

FIGURE 36. COMPUTED RAYS FOR UPWIND PROPAGATION OVER A HILL.

For wedge calculations a (p, q) pair of (33, 12) was used to approximate the wedge angle, yielding an angle of 4.3197 radians.

Resulting ILs appear in Table 2 and in Fig. 37a, where they are compared to experimental results.

Discussion of results

At the lower frequencies, the analysis predicts 5 dB of IL, which appears also in the experimental results. Then as frequency increases, the analysis predicts gently increasing IL; considerably more attenuation was measured experimentally. In addition, the experimental results include apparent interference not included in the mathematical model.

The no-wind condition provides a baseline for these with-wind calculations. For the no-wind case, the receptor lies on the grazing line-of-sight. Theory says that the resulting IL is 5 dB. This result appears in Fig. 37b, along with the no-wind experimental results. The analysis and experiment agree relatively well, except that the experimental results include the previously discussed interference not included in the mathematical model.

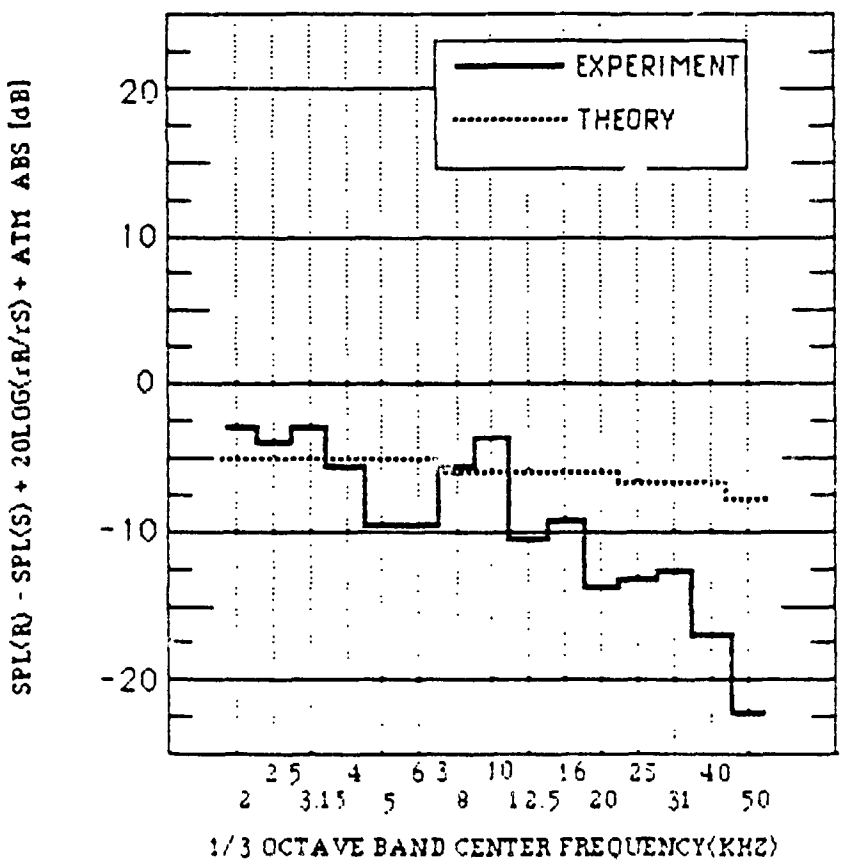

a. Wind Speed 8.8 m/s.

FIG. 37a. PROPAGATION UPWIND OVER A HILL (EFFECT 4). (SOURCE HEIGHT .15 m, RECEPTOR HEIGHT .15 m, DISTANCE 2.2 m, HILL HEIGHT .15 m.)

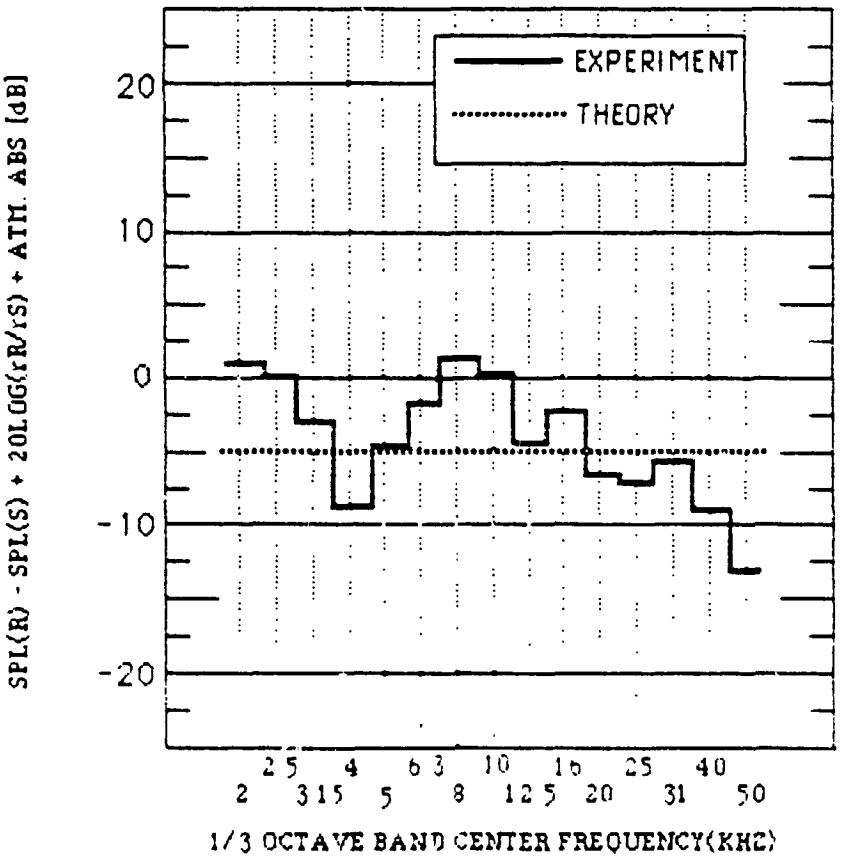

b. No Wind.

FIGURE 37b. PROPAGATION UPWIND OVER A HILL (EFFECT 4). (SOURCE HEIGHT .15 m, RECEPTOR HEIGHT .15 m, DISTANCE 2.2 m, HILL HEIGHT .15 m.)

7. SUMMARY AND CONCLUSIONS

The primary objective of the study was to evaluate the feasibility of using acoustical scale modeling techniques to evaluate long range, low angle sound propagation over hard and absorptive ground. The evaluation consisted primarily of the comparison of wind tunnel scale model test results with results obtained from analytical models of the propagation. In many cases, the comparison illustrated that scale modeling is a promising means of investigating sound propagation. Particularly noteworthy is the good comparison between theory and experiment for propagation over finite impedance ground (such as grassland). This pilot study points out clearly that further research is warranted both in the development of analytical models and in the experimental technique.

Critical lessons learned while conducting the program include the following:

- The use of high intensity spark sources require the damping of the ground plane to attenuate bending waves that can radiate sound to the receiver microphone.
- All reflecting surfaces on the spark source structure or near the spark source must be covered with absorptive material.
- Evaluation of the destructive interference between direct and reflected waves over hard ground requires that the difference in directional sensitivity of the receiver microphone in the direct and reflected wave directions be minimal.
- Evaluation of the destructive interference between direct and reflected waves over hard ground is limited by the noise floor of the acoustic measurement system.

- Accurate measurement of the wind velocity gradient in the vicinity of the ground plane is mandatory when ray tracing techniques are used to evaluate ground reflections.

This program has also pointed out the usefulness and need for additional work.

- Additional scale model experiments should be conducted to isolate the effects of wind over complex terrain under a variety of wind and ground impedance conditions.
- As a first step, the approximate analytical models for propagation over hills used in this program should be modified to include a ground plane.
- Additional analytical model development must be undertaken to quantify the propagation of sound over hills and more complex terrain.
- The analytical model of refraction should be extended to include the effects of ray-tube divergence.
- The effects of possible recirculating flow downstream of a hill should be measured and incorporated into the refraction analysis.
- Include in the analysis estimates of the influence of atmospheric turbulence on the measured noise spectra.

REFERENCES

1. Anderson, G.S., "Acoustical Scale Modeling of Roadway Traffic Noise: A Literature Review," Bolt Beranek and Newman Inc. Report 3630, Cambridge, MA, September 1978.

2. Bishop, D.E., "Overground Excess Sound Attenuation (ESA): Volume II: Analysis of Data for Flat Grass, Terrain Conditions," AFAMRL-TR-84-017-Vol II; February 1984.

3. DeJong, R.G., "A Model Study of the Effects of Wind on the Sound Attenuation of Barriers," Acoustics and Vibration Laboratory, Massachusetts Institute of Technology, Cambridge, 1974.

4. Snyder, W.H., "Guidelines for Fluid Modeling of Atmospheric Diffusion," EPA-600/8-81-009. U.S. Environmental Protection Agency, Environmental Sciences Research Laboratory, Research Triangle Park, NC, xiv and 185 pp., 1981.

5. Krauth, E., "Klangtreue Nachbildung der Raumakustik durch Modelle," doctural thesis, Technisch Hochschule, Munich, 1968.

6. Lyon, R.H., "Acoustical Modeling Handbook," Massachusetts Institute of Technology, Cambridge, MA, August 1975.

7. Rapin, J.M., "Etude des Modes de Protection Phoniques aux Abords des Voies Rapides Urbaines," Volume IA, CSTB, Grenoble, France, 1969.

8. Jones, H.W., D.C. Stredulinsky, P.J. Vermuelen, and J. Yu, "An Experimental and Theoretical Study of the Modelling of Urban Noise Problems," Acoustics Group, University of Calgary, Alberta, Canada, 1976.

9. Brooks, B.M., "A Model Study of Sound Propagation in a Random Array," B.Sc. Thesis, Dept. of Mech. Eng., Massachusetts Institute of Technology, Cambridge, MA, May 1974.

10. Delaney, M.E., A.J. Rennie and K.M. Collins, "Model Evaluation of the Noise Shielding of Aircraft Ground-Running Pens," NPL Report Ac67, 1974.

11. McShane, M.P., "Attenuation of Rail Noise at Bromley-Heath," Central Transportation Research Staff, Boston, MA, 1974 (in Ref. 1 above).

12. Ivey, E.S. and N.D. Lewis, "Model Studies of Housing and Walls as Roadside Noise Barriers," Dept. Mech. and Aerospace Eng., University of Massachusetts, Amherst, MA, 1974 (in Ref. 1 above).

13. Klinkowstein, R.E., "A Study of Acoustic Radiation from an Electric Spark Discharge in Air," M.Sc. Thesis, Dept. of Mech. Eng., Massachusetts Institute of Technology, Cambridge, MA, 1974.

14. Jones, H.W. and D.C. Stredulinsky, "Measurement of Surface Acoustic Impedances at Oblique Angles of Incidence and Ultrasonic Frequencies," J. Acoust. Soc. Am., Vol. 61, pp. 1089-1091, April 1977.

15. Embleton, T.F.W., J.E. Piercy, and G.A. Dingle, "Effective Flow Resistivity of Ground Surfaces Determined by Acoustical Measurements," J. Acoust. Soc. Am., Vol. 74, pp. 1239-1244, October 1983.

16. Jonasson, H.G., "Sound Reduction by Barriers on the Ground," J. Sound Vib., Vol. 22, No. 1. pp. 113-126, 1972.

APPENDIX A

Scale Model Sound Propagation Experiments
Ground Plane: Soft
Propagation Direction: Upwind

Tape	Run #	Spark Ht (in)	"Mountain" Height (in)	Receiver (Mic) Hgt	Reference Flow Velocity (mps)
26	168	0+	6	1/2, 3	0
	169				2.5
	170				5
	171				29
	172	0+	6	1 1/2, 6	0
	173				2.5
	174				5
27	175				29

Scale Model Sound Propagation Experiments
Ground Plane: Hard
Propagation Direction: Downwind

Tape	Run #	Source Ht (in)	"Mountain" Height (in)	Receiver (Mic) Hgt	Reference Flow Velocity (mps)	Comments
2	6	4138 CAL Tone				
	7	4135 CAL Tone				
	8	0+	-	0+	0	Ground plane problem
	9	0+	-	0+	0	Ground plane stuck down
	10	0+	-	0+	8.8	
	11	0+	-	0+	5	
	12	0+	-	0+	2.5	
	13	0+	-	0+	0	
	14	0+	-	0+	0	New smaller electrode holder
	15	0+	-	0+	8.8	
3	16a	0+	-	0+	5	
	17	0+	-	0+	2.5	
	18	0+	6	0+	0	
	19				8.8	
	20				5	
	21				2.5	
	22	0+	12	0+	0	
	23				8.8	
4	24				5	
	25				2.5	
	26	0+	12	1 1/2	0	
	27				8.8	
	28				5	
	29				2.5	
	30	0+	6	1 1/2	0	
	31				8.8	
5	32a				5	
	33				2.5	
	34	0+	-	1 1/2	0	
	35				8.8	
	36				5	
	37				2.5	

:cale Model Sound Propagation Experiments
:ound Plane: Hard
:opagation Direction: Downwind

Tape	Run #	Source Ht (in)	Mountain Height (in)	Receiver (Mic) Hgt	Reference Flow Velocity (mps)	Comments
	38	0+	-	3	0	
6	39				8.8	
	40				5	
	41				2.5	
6	42	0+	12	3	0	
	43				8.8	
	44				5	
	45				2.5	
	46	0+	12	6	0	
	47				8.8	
	48				5	
	49				2.5	No photo
	50a	0+	6	6	0	
8	51				8.8	
	52				5	
	53				2.5	
	54	0+	6	3	8.8	
	55				5	
	56				2.5	
	57				0	
	58	White noise test signal				

Scale Model Sound Propagation Experiments
Ground Plane: Hard
Propagation Direction: Upwind

Tape	Run #	Source Ht (in)	"Mountain" Height (in)	Receiver (Mic) Hgt	Reference Flow Velocity (mps)	Comments
9	59a	Ch. 5 CAL Tone				
	60	Ch. 7 CAL Tone				
	61	Ch. 6 CAL Tone				
	62	0+	-	0+, 3	0	
	63			0+, -	0	Interference check
	64			-, 3	0	Interference check
	65	0+	-	0+, 3	8.8	
	66				5	
	67				2.5	
	68	0+	6	0+, 3	0	
10	69a				8.8	
	70				5	
	71				2.5	
	72	0+	12	0+, 3	0	
	73				8.8	
	74				5	
	75				2.5	
11	76	0+	12	1 1/2, 6	0	
	77				8.8	
	78				5	
	79				2.5	
	80	0+	6	1 1/2, 6	0	
	81				8.8	
	82				5	
12	83				2.5	
	84	0+	-	1 1/2, 6	0	
	85				8.8	
	86				5	
	87				2.5	
	88	6	6	1 1/2, 6	0	
13	89a				8.8	
	90				5	
	91				2.5	

Scale Model Sound Propagation Experiments
Ground Plane: Hard
Propagation Direction: Upwind

Tape	Run #	Source Ht (in)	"Mountain" Height (in)	Receiver (Mic) Hgt	Reference Flow Velocity (mps)	Comments
14	96	6	12	1 1/2, 6	0	
	97				8.8	
	98				5	
	99				2.5	
	100	6	12	0+, 3	0	
	101				8.8	
15	102				5	
	103				2.5	
	104	6	-	0+, 3	0	
	105				8.8	
	106				5	
	107				2.5	
	108	6	6	0+, 3	0	
16	109				8.8	
	110				5	
	111				2.5	
	112	12	6	0+, 3	0	
	113				8.8	
	114				5	
	115				2.5	
17	116	12	-	0+, 3	0	
	117				8.8	
	118				5	
	119				2.5	
	120	12	12	0+, 3	0	
	121				8.8	
	122				5	
18	123				2.5	
	124	12	12	1 1/2, 6	0	
	125				8.8	
	126				5	
	127				2.5	

Scale Model Sound Propagation Experiments
Ground Plane: Hard
Propagation Direction: Upwind

Tape	Run #	Source Ht (in)	"Mountain" Height (in)	Receiver (Mic) Hgt	Reference Flow Velocity (mps)	Comments
	92	6	-	1 1/2, 6	0	
	93				8.8	
	94				5	
14	95a				2.5	
	128	12	-	1 1/2, 6	0	
	129				8.8	
19	130				5	
	131				2.5	
	132	12	6	1 1/2, 6	0	
	133				8.8	
	134				5	
	135				2.5	

Scale Model Sound Propagation Experiments
Ground Plane: Hard
Propagation Direction: Upwind (Repeat Runs)

Tape	Run #	Spark Ht (in)	"Mountain" Height (in)	Receiver (Mic) Hgt	Reference Flow Velocity (mps)
19	84 Repeat	0+	-	1 1/2, 6	0
20	87a Repeat	0+	-	1 1/2, 6	2.5
	76 Repeat	0+	12	1 1/2, 6	0
	77 Repeat				8.8
	78 Repeat				5
	79 Repeat				2.5
	66 Repeat	0+	-	0+, 3	5

Scale Model Sound Propagation Experiments
Ground Plane: Soft
Propagation Direction: Upwind

Tape	Run #	Spark Ht (in)	"Mountain" Height (in)	Receiver (Mic) Hgt	Reference Flow Velocity (mps)
21	136	0+	-	1/2, 3	0
	137				2.5
	138				5
	139				8.8
22	140	0+	-	1 1/2, 6	0
	141				8.8
	142				5
	143				2.5
	144	12 $(11\frac{13}{16})$	-	1 1/2, 6	0
	145				2.5
	146				5
23	147				8.8
	148	12	-	1/2, 3	0
	149				8.8
	150				5
	151				2.5
	152	6	-	1/2, 3	0
	153				8.8
24	154				5
	155				2.5
	156	6	-	1 1/2, 6	0
	157				8.8
	158				5
	159				2.5
	160	6	6	1 1/2, 6	0
25	161				2.5
	162				5
	163				29
	164	6	6	1/2, 3	0
	165				2.5
	166				5
	167				29

APPENDIX B: ANALYTICAL MODEL OF REFRACTION

Source: Pierce, Allan D., Acoustics, McGraw-Hill, 1981 (Chapter 8).

Sound refracts in the presence of a wind velocity field

$$\vec{v} = \vec{v}(\vec{x},t) \quad .$$

With knowledge of the emission direction from a point source, the sound-ray path is completely determined by numerical line integration, where the radius of curvature at any point is determined from the wind velocity gradient at that point. If

$$\vec{v} = \hat{i}v_x(z) \quad \text{only,}$$

then

$$\text{radius of curvature} = \frac{c}{\left(\frac{dv_x(z)}{dz}\right)}$$

where c = speed of sound in (still) air.

Any consistent set of units are valid.

This refraction model predicts the paths of rays, as they are curved by wind-velocity gradients. The refraction thus modifies the position of these rays relative to the terrain, and thereby may effect the level at the receiving microphone. In particular, if the refracted ray intercepts the terrain where the straight ray did not, then the received level would obviously be lower. Note that the wind velocity gradient is maximum in the vicinity of the surface. Clearly, very accurate measurements are required to accurately track rays near the surface. Since accurate measurements are difficult in this area, predictions that rely on rays that pass close to the surface must be viewed with skepticism.

Another refraction phenomenon can affect the received level: modified ray-tube divergence. A ray tube is a small bundle (small solid angle) of rays emanating from the source in a particular direction. In two dimensions, its boundaries appear as two nearly adjacent rays emanating from the source. As these nearly adjacent, straight rays progress outward from the source, they diverge from one another. This ray divergence occurs in a standard way for straight rays, for a given angular separation. Refraction will effect this rate of divergence, whenever it refracts one of the rays in a significantly different amount than the other. For example, if the upper of the two adjacent rays is refracted upward significantly more than is the lower, then the net divergence will be greater than it was without the refraction. Acoustically, this will reduce the level more rapidly as a function of distance than in the unrefracted case.

In this study, we neglected this refraction phenomenon. We suspect that this neglect will cause difficulty where the wind gradients change significantly over a quarter-wavelength or so.

APPENDIX C: ANALYTICAL MODEL OF DIFFRACTION

Sources:

1. Pierce, A.D. and W.J. Hadden, Jr., "Plane Wave Diffraction by a Wedge with Finite Impedance," J. Acoust. Soc. Am., Vol. 63, pp. 17-27, January 1978 (plane wave incidence, only).

2. Pierce, A.D. and W.J. Hadden, Jr., "Theory of Sound Diffraction Around Absorbing Barriers," presented at conference on Acoustic Protection of Residential Areas by Barriers, Centre National de la Recherche Scientifique, Laboratoire de Mecanique et d'Acoustique, Marseille, France, 18-20 February 1975 (generalization to point source).

3. Personal correspondence with Allan Pierce.

4. Kurze, U. and L.L. Beranek, "Sound Propagation Outdoors," in Noise and Vibration Control, ed. L.L. Beranek, McGraw-Hill, 1971.

An absorptive wedge is oriented with its (straight) diffracting edge along the z-axis, as shown in Fig. C.1. A point source is located at SCE. Desired is the IL due to the wedge at receptor REC.

Pierce

$$\left.\begin{matrix}\text{Insertion} \\ \text{Loss}\end{matrix}\right\} = (IL)_{\text{Hard-wedge}} - (\Delta IL)_{\text{absorptive}}$$

$$(IL)_{\text{Hard-wedge}} = 20 \log_{10} (L/\rho) + 10 \log_{10} (2\pi k r r_0/L)$$

$$- 20 \log_{10} [M_v^{-1} (\theta+\theta_0) + M_v^{-1} (\theta-\theta_0)]$$

$$L = [(z-z_0)^2 + (r+r_0)^2]^{1/2}$$

$$\rho = [r^2 r_0^2 - 2rr_0 \cos (\theta-\theta_0) + (z-z_0)^2]^{1/2}$$

$$k = 2\pi/\lambda$$

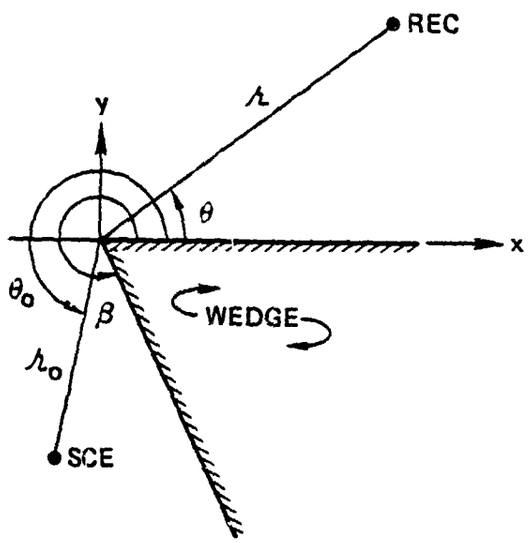

FIGURE C.1. DIFFRACTION GEOMETRY.

$$M_\nu(\theta) = \frac{\cos(\nu\pi) - \cos(\nu\theta)}{\nu \sin(\nu\pi)}$$

$$\nu = \pi/\beta$$

$$(\Delta IL)_{absorptive} = 10 \log_{10}\{|1+S_\beta(\theta-\theta_0)/\eta\sin\gamma|^2\}$$

$$S_\beta(\theta,\theta_0) = 2\,[M_\nu(\theta+\theta_0) + M_\nu(\theta-\theta_0)]^{-1} - Q_\beta(-\theta) - Q_\beta(-\theta_0)$$

$$Q(-\zeta) = \sum_{n=1}^{(p-1)/2} \left[\frac{-\nu \sin(\pi\nu)}{\sin[\nu(2\pi n-\zeta)\ \sin\{\nu[(2n-1)\pi-\zeta]\}}\right]$$

$$+ \sum_{m=0}^{q-1} \left[\frac{\sin(\zeta+2m\beta) + \sin[\zeta+\beta(2m+1)]}{\sin(\zeta+2m\beta)\ \sin[\zeta+\beta(2m+1)]}\right]$$

where λ = wavelength

η = acoustic impedance of the wedge, normalized to the impedance of air

r_0, θ_0, z_0 = polar coordinates of the source point

r, θ, z = polar coordinates of the receptor point

γ = angle between the z-axis and the SCE-APEX-REC line

β = external wedge angle

p, q = integers chosen so that $\beta = \pi p/2q$. 'p' must be odd and must have no common factors with 'q'. If no (p,q) pair can be found to satisfy this relationship with β exactly, then β may be bracketed above and below by selection of two (p,q) pairs, and the resulting ILs may be averaged.

All units of length must be identical. All angles must be in radians.

Kurze

$$\text{Insertion Loss} = 20 \log_{10} \left\{ \frac{(2\pi N)^{1/2}}{\tanh[(2\pi N)^{1/2}]} \right\} + 5 \quad \text{for } N > 0$$

$$= 20 \log_{10} \left\{ \frac{(-2\pi N)^{1/2}}{\tan[(-2\pi N)^{1/2}]} \right\} + 5 \quad \text{for } -0.1916 < N < 0$$

$$= 0 \quad \text{for } N < -0.1916$$

$N = \pm 2\ \delta/\lambda$ (positive if receptor is in geometrical shadow; otherwise negative)

$$\delta = L - L_s$$

$$L = [(z-z_0)^2 + (r+r_0)^2]^{1/2}$$

$$L_s = [(z-z_0)^2 + (r\cos\theta - r_0\cos\theta_0)^2 + (r\sin\theta - r_0\sin\theta_0)^2]^{1/2}$$

where λ = wavelength

$r_0, \theta_0 z_0$ = polar coordinates of the source point

r, θ, z = polar coordinates of the receptor point.

All units of length must be identical. The argument of the trigonometric tangent is in radians.

APPENDIX D: ANALYTICAL MODEL OF GROUND-REFLECTION

Sources:
1. Chessel, C.I., "Propagation of Noise Along a Finite Impedance Boundary," J. Acoust. Soc. Am., Vol. 62, pp. 825-834 (1977).
2. Embleton, T.F.W., J.E. Piercy, and G.A. Dingle, "Effective Flow Resistivity of Ground Surfaces Determined by Acoustical Measurements," J. Acoust. Soc. Am., Vol. 74, pp. 1239-1244, October 1983.

This model assumes that the source spectrum is flat (white) within any given 1/3-octave band. Such is not the case for the spark source spectrum.

Desired is the IL due to the ground, in 1/3-octave bands, relative to the level at the receptor in absence of the ground.

$$\left.\begin{matrix}\text{Third-}\\ \text{Octave}\\ \text{Insertion}\\ \text{Loss}\end{matrix}\right\} = 10 \log_{10}\left[1 + \left(\frac{r_1}{r_2}\right)^2 |O|^2 + \frac{2r_1}{r_2} |O| \sin\left(\frac{0.7275(r_2-r_1)}{\lambda}\right)\right.$$

$$\left. \times \frac{\cos(6.241(r_2 - r_1)/\lambda + \theta)}{0.7275(r_2 - r_1)/\lambda}\right]$$

$$O = R_p + F(w)\ (1-R_p)$$

$$R_p = \frac{\sin\phi - 1/n}{\sin\phi + 1/n}$$

$$\mathrm{Re}(n) = 1 + 9.08(f/\sigma)^{-0.75}$$

$$\mathrm{Im}(n) = 11.9(f/\sigma)^{-0.73}$$

$$F(w) = 1+i(\pi w)^{1/2} e^{-w} - 2e^{-w} \sum_{n=1}^{\infty} \frac{w^n}{(n-1)!(2n-1)} \qquad \text{for } |w| < 10$$

$$= - \sum_{n=1}^{\infty} \frac{(2n)!}{2^n n!(2w)^n} \qquad \text{for } |w| > 10 \text{ and Re } W > 0$$

$$w = \left(\frac{i\pi r_2}{\lambda} \right) \left[\frac{(\sin\phi + 1/\eta)^2}{1 + (\sin\phi)/\eta} \right]$$

$$\theta = \tan^{-1} \left[\mathrm{Im}(Q)/\mathrm{Re}(Q) \right]$$

where f = frequency, in Hertz

λ = wavelength

r_1 = distance between source and receptor, direct

r_2 = distance between source and receptor, reflected from ground

ϕ = grazing angle between reflected path and ground plane, in radians

η = acoustic impedance of ground, normalized to the impedance of air

σ = effective flow resistance of the ground (not the true flow resistance, as measured nonacoustically), in cgs rayls. For typical ground surfaces, values for σ are tabulated in the second reference above. For other ground surfaces, σ is best determined by fit to the measured $\mathrm{Re}(\eta)$ and $\mathrm{Im}(\eta)$.

All units of length must be identical. See Fig. C.1 for geometry.

In the presence of wind, it is necessary to separate this solution into three portions:

- Direct wave
- Reflected wave
- Ground/surface wave.

Normalized to the direct-wave pressure, these three portions become:

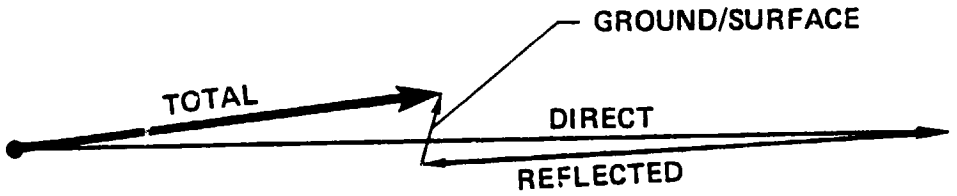

FIGURE D.1. GROUND-REFLECTION GEOMETRY.

- Direct-wave pressure: 1
- Reflected-wave pressure: $M_R \exp[i2\pi(\Phi_R + \Phi_{PL})]$
- Ground/surface-wave pressure: $M_{GS} \exp[i2\pi(\Phi_{GS})]$

where Φ_R = phase shift due to reflection

Φ_{PL} = phase shift due to path-length difference.

With this normalization, then:

$$M_R = |R_p|$$

$$\Phi_R = \tan^{-1} [Im(R_p)/Re(R_p)]$$

$$\Phi_{PL} = 2\pi(r_2-r_1)/\lambda$$

$$M_{GS} = |F(w)(1-R_p)|$$

$$\Phi_{GS} = \tan^{-1} [Im[F(w)(1-R_p)]/Re[F(w)(1-R_p)]].$$

Note that these apply at the center frequency of the 1/3-octave band of interest.

APPENDIX E: ANALYTICAL MODEL OF ATMOSPHERIC ABSORPTION

Source: "Method for the Calculation of the Absorption of Sound by the Atmosphere," American National Standard S1.26-1978, American Institute of Physics, 335 East 45th Street, New York, NY 10017.

$$\left.\begin{matrix}\text{Atmospheric} \\ \text{Absorption}\end{matrix}\right\} = 2\alpha s$$

$$\alpha = f^2 \left[1.84 \times 10^{-11} \left(\frac{P_s}{P_{so}}\right)^{-1} \left(\frac{T}{T_0}\right)^{1/2} + \left(\frac{T}{T_0}\right)^{-5/2} \left\{1.278 \times 10^{-2} \left[\exp_e(-2239.1/T)\right] / \left(f_{r,o} + (f^2/f_{r,o})\right) + 1.068 \times 10^{-1} \left[\exp_e(-3352/T)\right] / \left(f_{r,N} + (f^2/f_{r,N})\right)\right\}\right]$$

$$f_{r,O} = \left(\frac{P_s}{P_{so}}\right) \left\{24 + 4.41 \times 10^4 \, h \left[(0.05+h)/(0.391+h)\right]\right\}$$

$$f_{r,N} = \left(\frac{P_s}{P_{so}}\right) \left(\frac{T}{T_0}\right)^{-1/2} \left(9 + 350h \exp_e\left\{-6.142 \left[(T/T_0)^{-1/3} - 1\right]\right\}\right)$$

$$h = h_r \left(\frac{P_{sat}}{P_{so}}\right) \left(\frac{P_s}{P_{so}}\right)$$

$$\frac{P_{sat}}{P_{so}} = \exp_{10} \left[10.79586 \left[1-(T_{01}/T)\right] - 5.02808 \log_{10}(T/T_{01}) + 1.50474 \times 10^{-4} \left\{1 - \exp_{10}\left[-8.29692\left[(T/T_{01}) - 1\right]\right]\right\} + 0.42873 \times 10^{-3} \left\{-1 + \exp_{10}\left[4.76955\left[1-(T_{01}/T)\right]\right]\right\} - 2.2195983\right]$$

$$T_{01} = 293.15 \text{ K}$$

$$P_{so} = 1 \text{ atmosphere}$$

where s = distance between source and microphone, in feet

f = frequency, in Hertz

P_s = atmospheric pressure, in atmospheres

T = atmospheric temperature, in K

h_r = relative humidity, in percent.

APPENDIX F: DEVELOPMENT OF REPRESENTATIVE WIND PROFILES

The main text describes the wind measurements and contains plots of typical data. As input to the analysis, it was necessary to average these wind data and also to extend them upward and downward (below the ground). This appendix describes this wind-data averaging and extension, and documents the actual wind values used in the analysis.

F.1. Extension of Wind Data

The analysis software accepts wind data at discrete elevations and from these data computes wind gradients at these same elevations. For example, at height z_i, the software computes the gradient between z_{i-1} and z_i and then averages this with the gradient between z_i and z_{i+1}. The resulting gradient is assigned to height z_i.

This averaging method will not work for the topmost elevation, however, because z_{i+1} does not exist. For this elevation, therefore, z_i was initially ascribed the gradient between z_{i-1} and z_i, only. The analogous procedure was initially undertaken for the bottommost elevation, also.

However, this produced the following difficulty: often during ray tracing, the ray being traced either rises above the topmost wind elevation or descends below the bottommost (the ground). This causes the program to crash. Even more importantly, it eliminates the possibility of automatically hunting for the actual ray between two points, whenever this actual ray approaches the topmost elevation or the ground.

For this reason, the wind data were extended both upwards and downwards, below the ground. In this extension, the gradients were assumed equal to those in the last unextended interval. For example, for the bottom extension, the value of wind at z_{i-1}

was chosen so that the gradient between z_{i-1} and z_i was equal to the actual bottommost gradient: the one between z_i and z_{i+1}.

F.2. Averaging of Wind Data

Table F.1 contains the horizontal locations of all wind-speed measurements. Separate measurements were made for flat terrain and for the two different mountain heights. Where the table entry is empty, no measurements were made.

At these positions, Table F.2 contains the reference wind conditions measured. In all cases, the reference wind speed was measured at a height of 3.0 ft above a flat portion of the terrain. This reference wind speed is denoted by V_{REF} throughout this report. Where reference wind conditions are missing, they were not measured at that position.

Tables F.3 through F.5 contain the average of all wind data, for the three terrains of interest. These tables include the extended wind data, as well. In each table, each topmost and bottommost tabulation is "extended," rather than "measured." All data in the tables are normalized to V_{REF}.

TABLE F.1. WIND-SPEED MEASUREMENT LOCATIONS.

Terrain	Measurement Distance from Spark Source (ft)				
	St.0	St.2	St.4*	St.6	St.8
Flat	0				7.23
6-inch Hill	0	~1.8	3.91	~5.4	7.23
12-inch Hill	0		3.61	~5.4	7.23

*At top of hill.

In averaging wind data, normalization to V_{REF} was done first and then data were averaged irrespective of V_{REF}. Also, as many stacks of data were used in the averaging as possible. For example, for the flat terrain at Station 0 (Table F.3), data were averaged from all flat-terrain at all V_{REF} (four stacks of data; see Table F.2), plus Stations 0 and 2 for both hill terrains (three additional stacks of data).

Figure F.1 plots the wind profiles for easier visualization. Critical to near-ground refraction are the wind values near the ground. Note that these are not plotted with sufficient precision in this figure; the relevant tables should be used near the ground. Figure F.1 omits wind data for the 12-in hill, since no analysis was done for this terrain.

TABLE F.2. WIND-SPEED MEASUREMENT MATRIX.

Terrain	V_{REF} Wind Speeds at 3.0-ft Height (ft/sec)				
	St.0	St.2	St.4	St.6	St.8
Flat	16.4				16.4 29.1
6-inch Hill	16.4	16.4	16.4	8.2 16.4 29.1	16.4
12-inch Hill	16.4		16.4	8.2 16.4 29.1	16.4

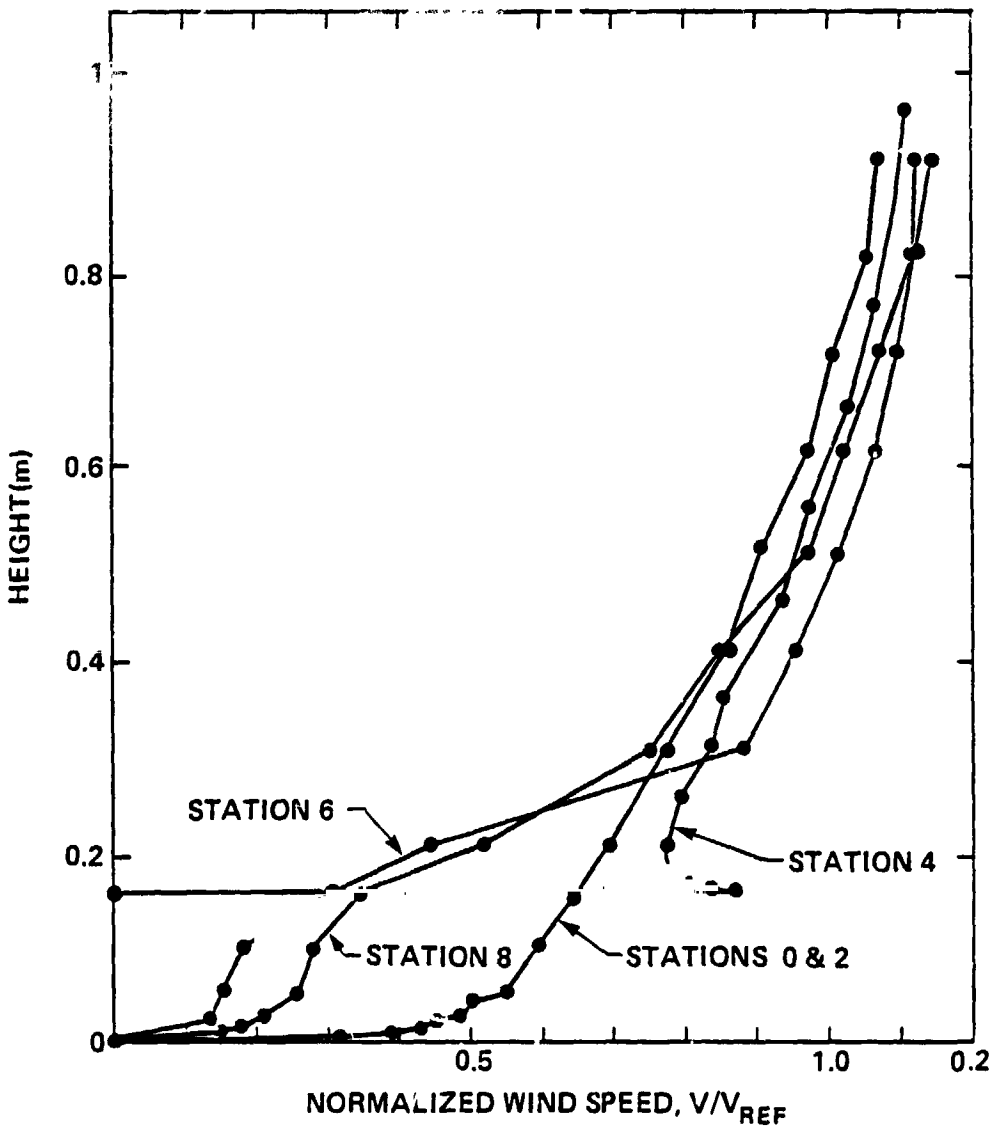

FIGURE F.1. MEAN VELOCITY PROFILES FOR SET-UP WITH TWO-DIMENSIONAL 15.24 cm HILL.

TABLE F.3. NORMALIZED WIND SPEEDS: FLAT TERRAIN.

Height (ft)	Normalized Wind Speed (ft/sec)				
	St.0	St.2	St.4	St.6	St.8
-1	-30.1				-30.1
0	0				0
0.0104	0.313				0.313
0.0208	0.394				0.394
0.0417	0.437				0.437
0.0625	0.456				0.456
0.0833	0.491				0.491
0.125	0.501				0.501
0.167	0.551				0.551
0.333	0.596				0.596
0.5	0.649				0.649
0.667	0.693				0.693
1	0.772				0.772
1.33	0.857				0.857
1.67	0.907				0.907
2	0.971				0.971
2.33	1.008				1.008
2.67	1.055				1.055
3	1.07				1.07
4	1.115				1.115

TABLE F.4. NORMALIZED WIND SPEEDS: SIX-INCH HILL.

Height (ft)	Normalized Wind Speed				
	St.0	St.2	St.4	St.6	St.8
-1	-30.1	-30.1	-129	-1.62	-4.49
0	0	0		0	0
0.0104	0.313	0.313			
0.0208	0.394	0.394			
0.0312					0.140
0.0417	0.437	0.437			0.167
0.0625	0.456	0.456			0.187
0.0833	0.491	0.491		0.135	0.212
0.125	0.501	0.501			
0.167	0.551	0.551		0.150	0.259
0.333	0.596	0.596		0.183	0.283
0.5	0.649	0.649	0	0.303	0.348
0.51			0.860		
0.521			0.829		
0.542			0.793		
0.562			0.787		
0.583			0.780		
0.625			0.774		
0.667	0.693	0.693	0.774	0.449	0.513
0.833			0.793		
1	0.772	0.772	0.835	0.885	0.757
1.17			0.854		
1.33	0.857	0.857		0.955	0.851
1.5			0.933		
1.67	0.907	0.907		1.018	0.973
1.83			0.976		
2	0.971	0.971		1.067	1.024
2.17			1.030		
2.33	1.008	1.008		1.095	1.073
2.5			1.067		
2.67	1.055	1.055		1.122	1.125
2.83			1.091		
3	1.070	1.070		1.143	1.127
3.17			1.110		
4	1.115	1.115	1.156	1.207	1.133

TABLE F.5. NORMALIZED WIND SPEEDS: 12-INCH HILL.

Height (ft)	Normalized Wind Speed				
	St.0	St.2	St.4	St.6	St.8
-1	-30.1	-30.1	-204.8	-3.8	-5.58
0	0	0		0	0
0.0104	0.313	0.313			
0.0208	0.394	0.394		0.079	0.116
0.0417	0.437	0.437		0.086	0.122
0.0625	0.456	0.456		0.082	0.116
0.0833	0.491	0.491		0.089	0.128
0.125	0.501	0.501			
0.167	0.551	0.551		0.103	0.146
0.333	0.596	0.596		0.107	0.146
0.5	0.649	0.649		0.134	0.177
0.667	0.693	0.693		0.165	0.213
1	0.772	0.772	0	0.344	0.470
1.01			1.024		
1.02			1.024		
1.04			1.024		
1.06			1.018		
1.08			1.018		
1.12			1.006		
1.17			1.000		
1.33	0.857	0.857	1.000	0.742	0.646
1.5			1.037		
1.67	0.907	0.907	1.061	1.124	1.012
2	0.971	0.971	1.104	14.179	1.213
2.33	1.008	1.008	1.183	1.234	1.256
2.67	1.055	1.055	1.201	1.275	1.305
3	1.070	1.070	1.238	1.296	1.366
4	1.115	1.115	1.35	1.36	1.55

As shown in the tables above, wind was measured along several stacks, spaced between source and receptor. For refraction calculations, the wind gradients must be known everywhere between source and receptor. For this purpose, we linearly interpolated vertically within each stack, to obtain values at heights not measured. In addition, we linearly interpolated horizontally between stacks, to obtain values at intermediate distances from the source.

For the cases with hill, before this horizontal interpolation we translated the stacks at Stations 2 and 6 to the foot of the hill.

This horizontal interpolation is awkward for the cases with hill, between the hilltop stack (Station 4) and the two adjacent stacks. For one, interpolation at constant height is not possible in these situations, because the Station-4 stack does not extend low enough in elevation. To avoid this difficulty - interpolation with the hilltop stack but below hilltop height - we interpolated between the proper height on Station 2 (or 6) and the zero-height gradient on the hilltop stack. Such an interpolation yields an even flow over the hilltop - in which the flow evenly compresses as it approaches the hilltop, with a corresponding increase in speed, then passes over the hilltop, and then evenly expands again on the downwind side. We suspect that the upwind approximation is sufficiently valid, but that the downwind approximation is not. Instead of even expansion and even decrease in wind speed downwind, turbulent eddies are created downwind of the hilltop. Within these large eddies, the wind actually reverses direction near the ground. These eddies and direction-reversals are not included in our analysis.

1. Report No.	2. Government Accession No.	3. Recipient's Catalog No.
NASA CR 172488		

4. Title and Subtitle	5. Report Date
Evaluation of the Feasibility of Scale Modeling to Quantify Wind and Terrain Effects on Low-Angle Sound Propagation	January 1985
	6. Performing Organization Code
7. Author(s)	8. Performing Organization Report No.
G.S. Anderson, R.E. Hayden, A.R. Thompson, R. Madden	BBN Report No. 5516
9. Performing Organization Name and Address	10. Work Unit No.
Bolt Beranek and Newman Inc. 10 Moulton Street Cambridge, MA 02238	11. Contract or Grant No NAS1-16521
12. Sponsoring Agency Name and Address	13. Type of Report and Period Covered
National Aeronautics and Space Administration Washington, DC 20546	Contractor Report
	14. Sponsoring Agency Code

15. Supplementary Notes

Langley Contracting Officer: Charles L. Crowder
Technical Monitor: John S. Preisser
Final Report

16. Abstract

The objective of this study was to evaluate the feasibility of acoustical scale modeling techniques for modeling wind effects on long-range, low-frequency outdoor sound propagation. Upwind and downwind propagation was studied in 1/100 scale for flat ground and simple hills with both rigid and finite ground impedance over a full scale frequency range from 20 to 500 Hz.

Results are presented as 1/3-octave frequency spectra of differences in propagation loss between the case studied and a free-field condition. Selected sets of these results were compared with predictions from approximate models developed specifically for this study. Comparisons were encouraging in many cases considering the approximations involved in both the physical modeling and analysis methods. Of particular importance was the favorable comparison between theory and experiment for propagation over soft ground.

17. Key Words (Suggested by Author(s))	18. Distribution Statement
Acoustic Scale Modeling Low-angle Sound Propagation	Unclassified - Unlimited

19. Security Classif. (of this report)	20. Security Classif. (of this page)	21. No. of Pages	22. Price
Unclassified	Unclassified	124	